

RESEARCH

PROFESSOR K. KOMVOPOULOS

Research in the *Surface Sciences and Engineering Laboratory (SSEL)* and the *Computational Surface Mechanics Laboratory (CSML)* under the directorship of Professor Komvopoulos is at the interfaces of mechanical and electrical engineering, materials science/engineering, surface physics/chemistry, and bioengineering. Most investigations are characterized by interdisciplinary nature and make use of a wide range of analytical and experimental techniques aimed to provide insight into complex surface and interface phenomena.

Surface Sciences and Engineering Laboratory (SSEL)

Research in SSEL relies on the integration of fundamentals from mechanics, materials science, surface physical chemistry, and bioengineering/biology, and spans a broad range of length scales, from macroscopic down to the atomic and molecular levels.

Current research conducted in SSEL comprises projects in the following areas:

- **WEARABLE AND EPIDERMAL ELECTRONICS**
- **MICRO-ELECTRO-MECHANICAL SYSTEMS (MEMS)**
- **BIOMEDICAL**
- **THIN FILMS**
- **ENGINE LUBRICATION**
- **ENERGY**

Major Equipment

- RF sputtering system (Perkin-Elmer Randex 2000)
- High-vacuum multi-probe MEMS station (MMR Technologies)
- Ion beam-assisted deposition system (Sierra Technology Group)
- Filtered cathodic vacuum arc deposition facility (custom-made)
- Inductively coupled plasma-assisted surface treatment system for biopolymer surface treatment (custom-made)
- AFM and STM instruments (Nanoscope II, Digital Instruments)
- Nanoindenter (AFM + force sensor (Triboscope, Hysitron))
- Reciprocating and unidirectional sliding pin-on-disk tribometer (custom-made)
- Four-ball tester with temperature control and contact voltage measurement capability (Falex)
- Equipment of lapping experiments with acoustic sensor (Buehler)
- Fretting wear tester with temperature control and dynamic loading capabilities (Buehler)

Summaries of Research Projects

1. WEARABLE AND EPIDERMAL ELECTRONICS

The goal of this research program is the design of polymeric structures with intrinsic large reversible flexibility and stretchability, the development of polymeric materials with properties matching those of the human epidermis, the incorporation of electronics (soft actuators) in flexible/stretchable materials for measuring vital human signals (e.g., pulse, temperature, thermoregulation, hidrosis by monitoring water-rich secretion of the eccrine glands) and sweat metabolites (e.g., glucose and lactate) and electrolytes (e.g., sodium and potassium ions). We are also interested in developing epidermal electronics for controllable transdermal drug delivery by microneedle arrays integrated with stretchable materials.

In a recently completed project (in collaboration with Tsinghua University), we developed two energy storage and supply modules with good electronic performance and the soft, compliant mechanics suitable for integration to biological interfaces. The first module (Fig. 1) consists of an array of microsupercapacitors (MSCs) joined together by deformable interconnects and embedded in elastomeric materials structured into a honeycomb shape. This layout accommodates significant tensile and compressive strains by in-plane bending of interconnects, while the MSCs are shielded from excessive strain. Because of this design, the resulting module demonstrates excellent rate capability, power performance, and electrochemical stability up to 150% of stretching (Fig. 1b), even under excessive bending (Fig. 1c) and twisting (Fig. 1d). We have also demonstrated that the module can light up a commercial LED, even in a heavily deformed configuration (Fig. 1e).

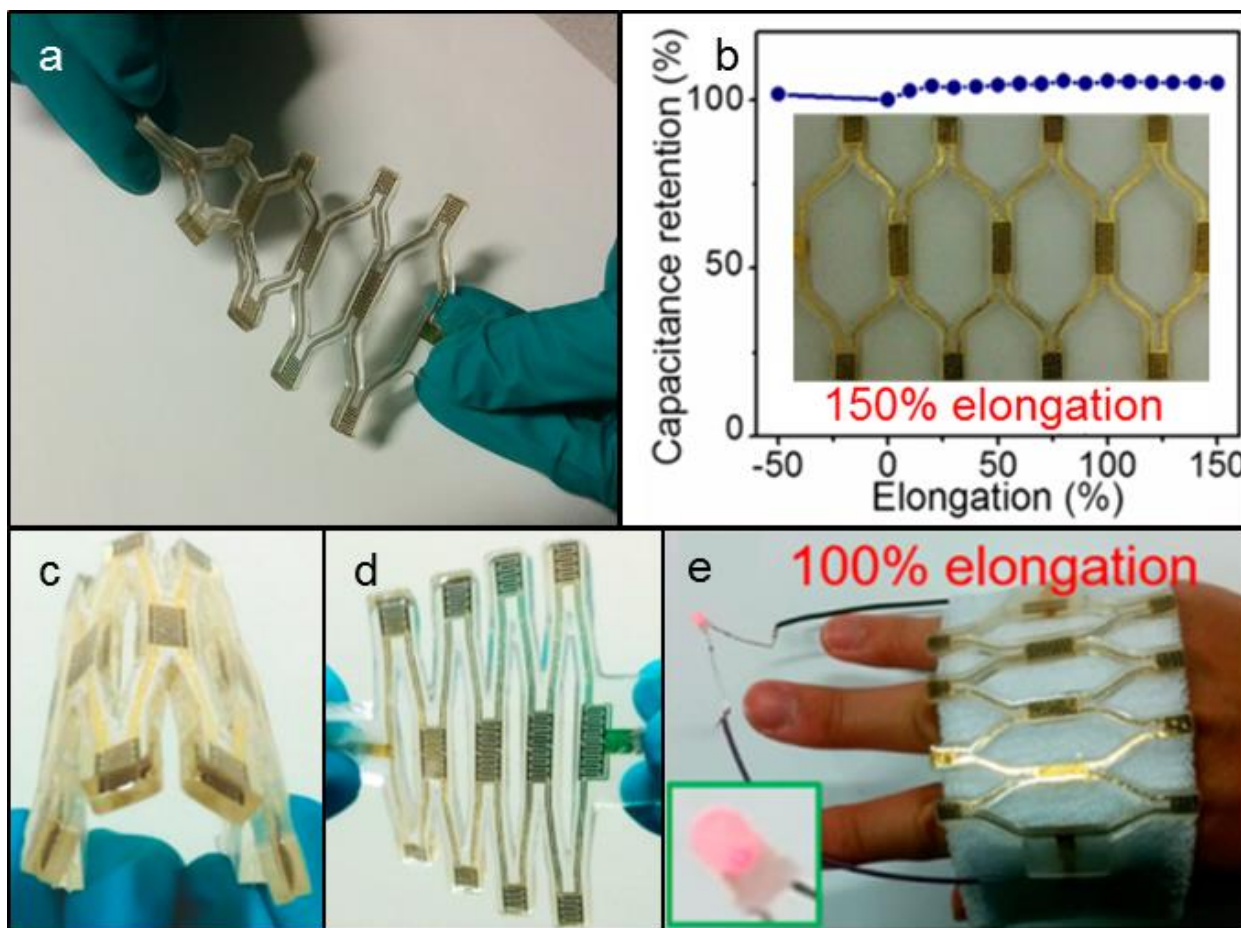


Figure 1

The second module is a miniaturized (8.4 mm × 5.7 mm) flexible MSC that is smaller than the area of a finger nail (Fig. 2a). The miniaturized MSC consists of interdigital electrodes residing on an ultrathin polyimide substrate, a network of single-walled carbon nanotubes (SWCNT), and an elastomeric superstrate. The optimization of the structural design and the integration of high-performance electronic materials have provided the module with high energy density (comparable to thin-film lithium ion batteries), ultrahigh power density ($>1000 \text{ W}\cdot\text{cm}^{-3}$), and extremely small time constant ($\sim 1 \text{ ms}$). In addition, these desirable electronic performances are almost uncompromised when the module is wrapped around rods of different radii (Fig. 2b), rolled into a scroll (Fig. 2c), or folded into half (Fig. 2d).

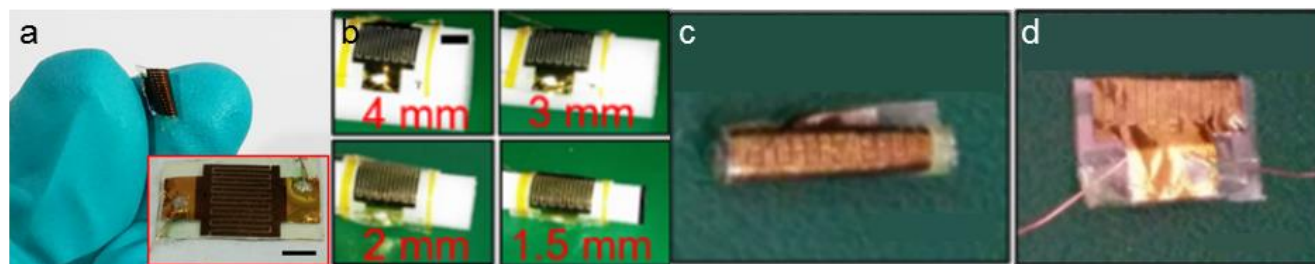


Figure 2

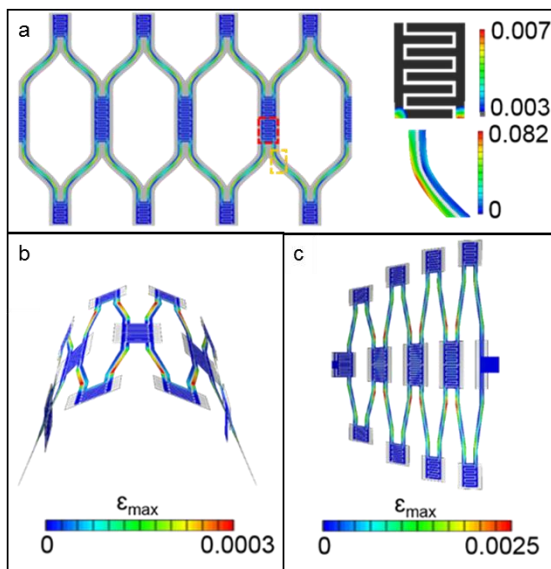


Figure 3

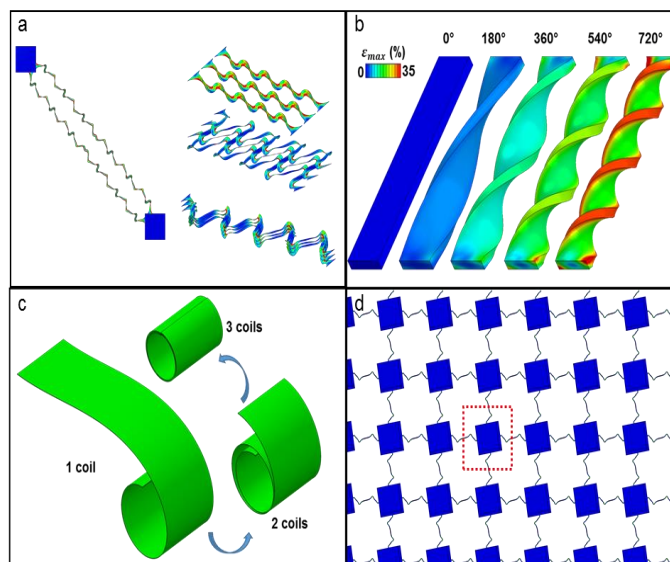


Figure 4

In previous and current projects of our group, 3D finite element analysis (FEA) was used to guide the design of flexible/stretchable electronics and soft actuators before device microfabrication. This numerical approach, which has been validated by experiments (Fig. 3), can accurately capture deformation details, yield stress and strain distributions in regions of interest, and predict the failure site and mechanism. FEA greatly benefits the design process by efficiently finding an optimum design through iteration, without the need of unnecessary experiments. After device fabrication, systematic mechanical testing is performed to experimentally obtain the mechanical properties of the devices and to validate the FEA models.

We are currently working on the development of more flexible and stretchable electronic devices and soft actuators. Some of the main subtasks include the mechanics of interconnect patterns (Fig. 4a), elastomeric materials (Figs. 4b and 4c), large periodic arrays (Fig. 4d), and the exploration of new microfabrication techniques.

Selected Publications

Pu, J., Wang, X., Kuang, X., Xu, S., Li, S., and Komvopoulos, K., "Stretchable Microsupercapacitor Arrays with a Composite Honeycomb Structure," *Proceedings of the 29th IEEE International Conference on Micro Electro Mechanical Systems (MEMS 2016)*, 24-28 Jan. 2016, pp. 1232–1235.

Pu, J., Wang, X., Xu, R., and Komvopoulos, K., "Highly Stretchable Microsupercapacitor Arrays with Honeycomb Structures for Integrated Wearable Electronic Systems," *ACS Nano* **10**(10) 9306 (2016).

2. MICRO-ELECTRO-MECHANICAL SYSTEMS (MEMS)

Miniaturized dynamic devices for sensing, actuation, and control, known as micro-electro-mechanical systems (MEMS), have led to new technologies, which are projected to impact science and engineering in many different ways. In view of the multidisciplinary nature of MEMS, it is essential to integrate basic knowledge derived from mechanical, electrical, and chemical engineering disciplines with versatile MEMS devices and novel testing protocols. To enable the transition of MEMS from the

research environment to the market place, it is essential to obtain fundamental understanding of the device response under both static and dynamic loadings and various environments.

The functionality of numerous MEMS devices is affected by surface adhesion forces arising between proximity interfaces. Earlier work in our lab revealed the importance of interface topography (texture) and surface energy on adhesion forces. Our more recent work is focused on the development of microdevices and testing protocols that closely resemble actual operation conditions and methods of measuring adhesion and friction forces at MEMS interfaces. Novel microdevices for measuring adhesion and friction forces at both planar and sidewall micromachine surfaces were designed, fabricated, and tested. Particular attention was drawn to sidewall surfaces because they possess significantly different topographies than planar surfaces (due to the profoundly different fabrication processes) and, more importantly, because quantification of surface forces at sidewall surfaces is very limited compared with planar surfaces.

To investigate adhesion of sidewall surfaces, a special multi-purpose microdevice was fabricated by surface micromachining and tested under conditions mimicking those of typical contact-mode MEMS devices. We have developed an experimental scheme that enables direct measurement of the critical normal force at the instant of surface separation and the friction force at the onset of sliding. Additional capabilities in our design include the evaluation of the dynamic friction behavior, measurement of the electrical characteristics across the contact interface, and characterization of the tribological response under impact contact loading. This microdevice can be operated over a wide range of normal forces and different environmental conditions. Because the design is independent of the process environment, a novel feature of the particular microdevice is the study of the effects of different surface treatments (e.g., monolayers) and variations in fabrication process steps on the tribological properties of MEMS contact interfaces.

Selected Publications

Komvopoulos, K., "Surface Engineering and Microtribology for Microelectromechanical Systems," *Wear* **200**(1-2) 305 (1996).

Komvopoulos, K., "Challenging Issues in Microelectromechanical Systems," *Micro-Electro-Mechanical Systems (MEMS) Proceedings, DSC-66* 261 (1998).

Komvopoulos, K., "Surface Texturing and Chemical Treatment Methods for Reducing High Adhesion Forces at Micromachine Interfaces," in *Materials and Device Characterization in Micromachining*, Eds., Friedrich C. R. and Vladimirovsky Y., *Proceedings of SPIE* **3512** 106 (1998).

Komvopoulos, K., "Nanoengineering and Tribophysics for Microelectromechanical Systems," in *Nanotribology: Critical Assessment and Research Needs*, Eds. S. M. Hsu and Z. C. Ying, Kluwer, Boston, MA, 2002, pp. 139–164.

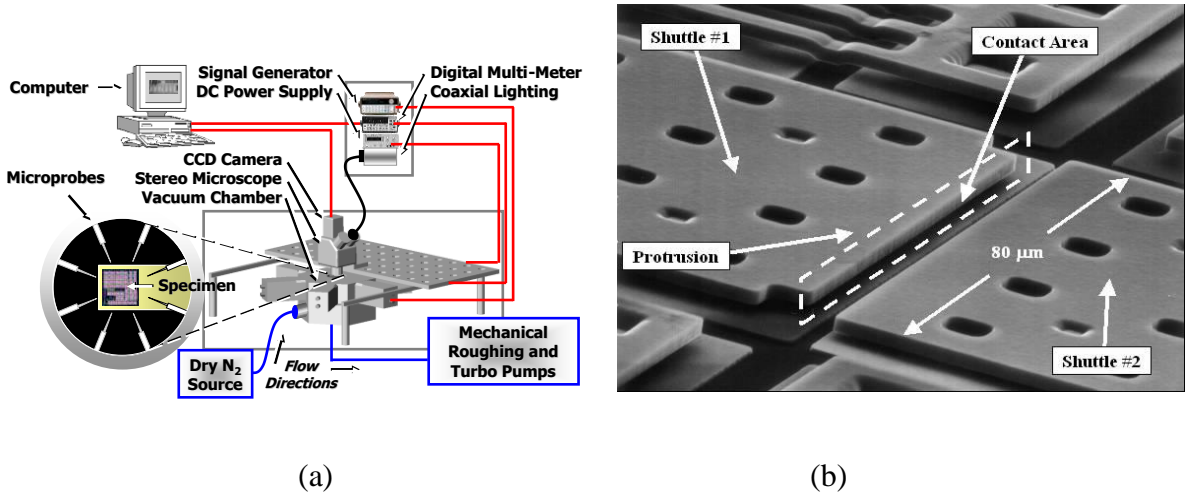
Komvopoulos, K., "Adhesion and Friction Forces in Microelectromechanical Systems: Mechanisms, Measurement, Surface Modification Techniques, and Adhesion Theory," *Journal of Adhesion Science and Technology* **17**(4) 477 (2003).

Summaries highlighting main findings of the MEMS projects mentioned above are given below.

2.1. Sidewall Adhesion of MEMS Devices

Static friction phenomena at sidewall surfaces were examined with the microdevice MEMS station and microdevices shown below. The dependence of sidewall static friction on contact pressure, ambient

conditions, relative humidity, and temperature was examined in parametric studies. It was found that the static friction coefficient exhibits a nonlinear variation with external contact pressure. A difference between *in-contact* and *pull-out* adhesion forces was observed due to the elastic recovery of deformed asperities at the contact interface. An important contribution to the MEMS field is the introduction of the *true* static coefficient of friction, which accounts for the effects of van der Waals and capillary forces on the normal force applied at sidewall contact interfaces.



(a) Schematic of high-vacuum multi-probe MEMS station and (b) MEMS device for sidewall adhesion and friction testing with a sidewall protrusion for controlling the apparent contact area.

Electrical and thermal effects on the adhesion force at sidewall contact interfaces of MEMS devices were also investigated. A significant increase of the adhesion force was found for relatively low current flow across the interface. In this case, current flow through asperity contacts led to the accumulation of trapped charges in the insulating oxide layer, resulting in electrostatic attraction, which remained even after surface separation and with ground surfaces. Alternatively, high current flow across asperity contacts due to dielectric breakdown of the native oxide layer commenced at a critical voltage, resulting in interfacial bonding that caused permanent adhesion of the sidewall surfaces.

Selected Publications

Lumbantobing, A., Kogut, L., and Komvopoulos, K., “Electrical Contact Resistance as a Diagnostic Tool for MEMS Contact Interfaces,” *Journal of Microelectromechanical Systems* **13**(6) 977 (2004).

Kogut, L., Lumbantobing, A., and Komvopoulos, K., “In Situ Monitoring of Native Oxide Film Behavior at MEMS Contact Interfaces Through Basic Electrical Measurements,” *Technical Digest, Solid-State Sensor, Actuator and Microsystems Workshop*, Hilton Head Island, SC, 2004, pp. 310–315.

Lumbantobing, A., and Komvopoulos, K., “Static Friction in Polysilicon Surface Micromachines,” *Journal of Microelectromechanical Systems* **14**(4) 651 (2005).

Kogut, L., and Komvopoulos, K., “Significance of Surface Topography on Performance and Lifetime of MEMS Switches and Relays,” *Materials Research Society Symposium Proceedings* **872** J2.4.1 (2005).

Timpe, S. J., and Komvopoulos, K., “An Experimental Study of Sidewall Adhesion in Microelectromechanical Systems,” *Journal of Microelectromechanical Systems* **14**(6) 1356 (2005).

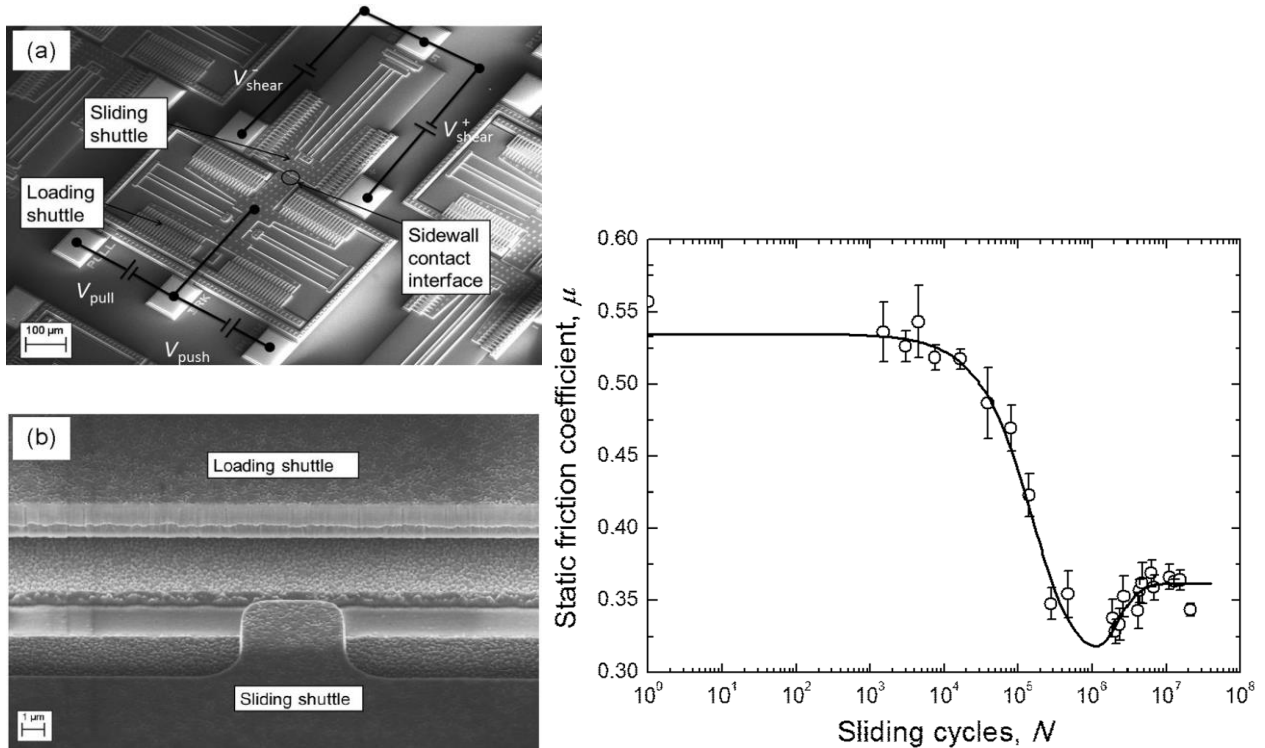
Timpe, S. J., and Komvopoulos, K., “The Effect of Adhesion on the Static Friction Properties of Sidewall Contact Interfaces of Microelectromechanical Devices,” *Journal of Microelectromechanical Systems* **15**(6) 1612 (2006).

Timpe, S. J., and Komvopoulos, K., "Effects of Electrical and Thermal Phenomena on the Evolution of Adhesion at Contact Interfaces of Electrostatically Activated Surface Microstructures," *Applied Physics Letters* **90**(9) 093510 (2007).

Timpe, S. J., and Komvopoulos, K., "Microdevice for Measuring Friction and Adhesion Properties of Sidewall Contact Interfaces of Microelectromechanical Systems," *Review of Scientific Instruments* **78**(6) 065106 (2007).

2.2. Adhesion-Induced Stiction and Friction in Contact-Mode MEMS Devices

The previous microdevice was also used to study the effect of repetitive impact loading on the evolution of the adhesion force at sidewall contact interfaces. A low and stable adhesion force was encountered during the initial stage of impact testing (run-in phase). A surface degradation phase commenced subsequently, in which the adhesion force increased logarithmically with increasing impact cycles. This experimental trend was used to predict micromachine failure due to excessive interfacial adhesion. An unexpected finding was that changes in the surface topography did not occur even after ~55 million impact cycles, despite the significant increase of the adhesion force. An important contribution to the MEMS field is the identification of the dominant surface degradation mechanisms of sidewall polycrystalline surfaces subjected to dynamic contact.



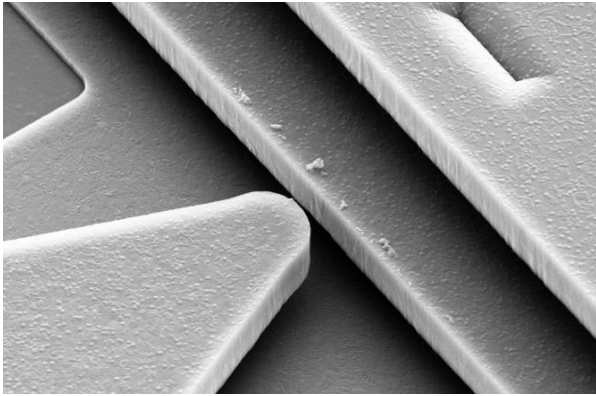
Left: SEM images of (a) surface micromachine, including the electrical wiring diagram for electrostatic comb-drive actuation, and (b) contact region showing a protrusion extending from the side of the sliding shuttle, which is used to control the apparent contact area with the opposed sidewall surface of the loading shuttle.

Right: Static friction coefficient vs sliding cycles.

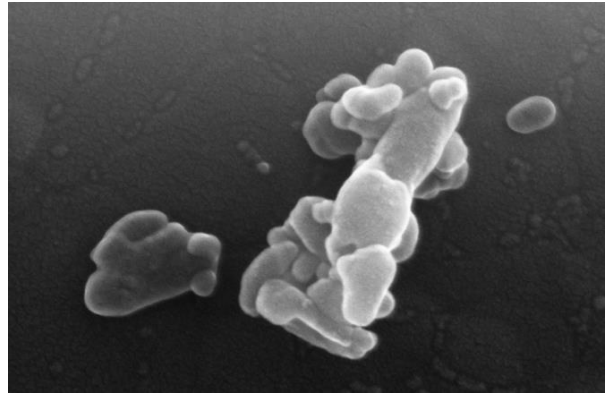
New insight into dynamic friction phenomena, such as stick-slip, was the goal of another study of oscillating MEMS devices. Variations in static and dynamic friction force were tracked *in situ* throughout testing under controlled loading and environmental conditions. Stick-slip surface interactions

occurred after many sliding cycles. An unexpected binary friction behavior commenced as sliding transitioned between two-body and three-body contact conditions due to the formation of fine wear particles. A counterintuitive finding was that oscillating MEMS devices failed in static friction mode rather than dynamic friction mode. This research illustrates the important role of microscale stick-slip phenomena in high-speed oscillatory microdevices.

In more recent work, we explored the evolution of wear at sidewall surfaces of polysilicon MEMS devices operated in high vacuum under controlled contact load and sliding speed conditions. Measurements of the static adhesion force as a function of sliding cycles and SEM observations of microdevices subjected to nominally identical testing conditions revealed two distinctly different tribological patterns, namely low-adhesion/high-wear behavior and high-adhesion/low-wear behavior. The static adhesion force and wear behavior were found to correlate with the micromachine's operational lifetime. TEM results yielded insight into the origin, microstructure, and composition of wear debris and agglomerates adhered onto the sliding surfaces.



(a)



(b)

SEM micrographs of a micromachine that demonstrated low-adhesion/high-wear behavior showing (a) wear debris pushed out of the sliding track on top of the main shuttle and (b) agglomerates of fine wear debris.

An important finding is that, even if there is some tolerance for wear debris in a MEMS device, e.g., when/if electrical conductance is not required, maintaining a low adhesion force may be critical to the effective operation of the device. Such a design requires a robust, self-replenishing coating, which will prevent significant changes in the surface composition despite the generation of wear debris. Alternatively, a design with increased tolerance for a high adhesion force (because of the high stiffness of the mechanical suspension, such as in the case of inertial sensors, for example) may exhibit a small tolerance for wear debris due to the electrical activation of the device.

Selected Publications

Timpe, S. J., Komvopoulos, K., and Dugger, M. T., "Microscale Friction Phenomena in Oscillatory Sliding Contacts," *Journal of Applied Physics* **102**(12) 123503 (2007).

Timpe, S. J., Hook, D. A., Dugger, M. T., and Komvopoulos, K., "Levitation Compensation Method for Dynamic Electrostatic Comb-Drive Actuators," *Sensors and Actuators A: Physical* **143**(2) 383 (2008).

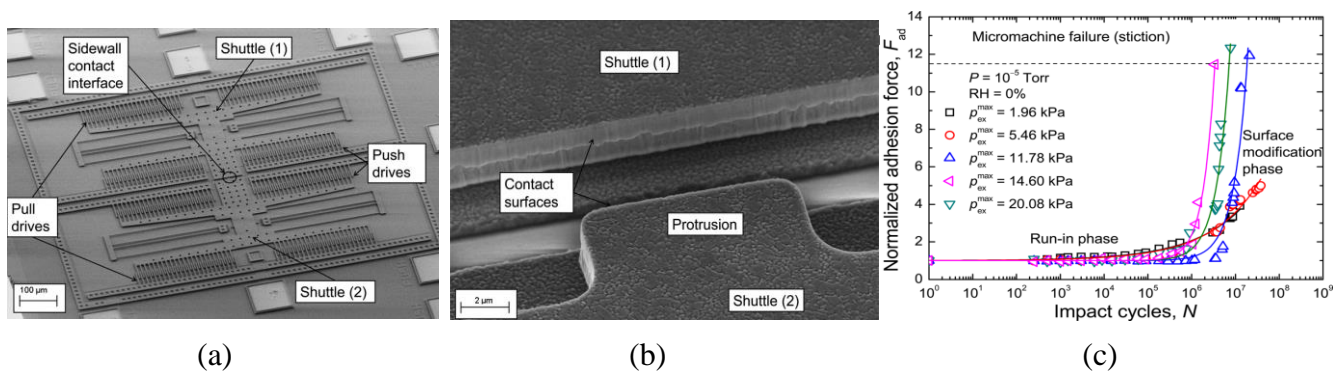
Timpe, S. J., Alsem, D. H., Hook, D. A., Dugger, M. T., and Komvopoulos, K., "Wear of Polysilicon Surface Micromachines Operated in High Vacuum," *Journal of Microelectromechanical Systems* **18**(2) 229 (2009).

Alsem, D. H., Xiang, H., Ritchie, R. O., and Komvopoulos, K., "Sidewall Adhesion and Sliding Contact Behavior of Polycrystalline Silicon Microdevices Operated in High Vacuum," *Journal of Microelectromechanical Systems*, **21**(2) 359 (2012).

Xiang, H., and Komvopoulos, K., "High-Vacuum Adhesion and Friction Properties of Sliding Contact-Mode Micromachines," *Applied Physics Letters* **103**(3) 033507 (2013).

2.3. Dynamic Contact (Impact) of MEMS Devices

Special contact-mode surface micromachines were used to study the effect of repetitive impact loading on the evolution of the adhesion force at sidewall contact interfaces. Based on the experimental trend, a method of predicting micromachine failure due to excessive interfacial adhesion was developed and confirmed experimentally. High-magnification SEM did not show any modification of the surface topography even after 5.5×10^7 impact cycles, despite the significant increase of the adhesion force, attributed to the increase of the real contact area and the higher surface energy due to the removal of the organic residue produced by supercritical drying. Adhesion force measurements and microscopy images of the impacted surfaces were used to examine the dominant surface degradation mechanisms. The principal goal of this work was to correlate the adhesion force with the impact cycles of MEMS devices operated in different environments.



(a) SEM image of a surface micromachine designed for repetitive dynamic contact (impact) of the sidewall surfaces under controlled loading and environmental conditions.

(b) High-magnification SEM image showing a protrusion extending from the sidewall of shuttle (2), which is used to control the apparent contact area with the sidewall surface of shuttle (1).

(c) In-vacuum variation of normalized adhesion force with impact cycles for externally applied maximum contact pressure in the range of 1.96-20.08 kPa.

Selected Publications

Philippine, M. A., Timpe, S. J., and Komvopoulos, K., "Evolution of Interfacial Adhesion Force in Dynamic Micromachines Due to Repetitive Impact Loading," *Applied Physics Letters* **91**(6) 063102 (2007).

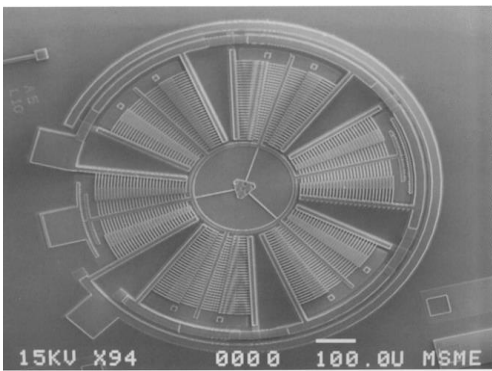
Xiang, H., and Komvopoulos, K., "Evolution of Sidewall Adhesion in Surface Micromachines Due to Repetitive Impact Loading," *Journal of Applied Physics* **111**(5) 054507 (2012).

Xiang, H., and Komvopoulos, K., "The Effect of Impact Velocity on Interfacial Adhesion of Contact-Mode Surface Micromachines," *Applied Physics Letters* **101**(5) 053506 (2012).

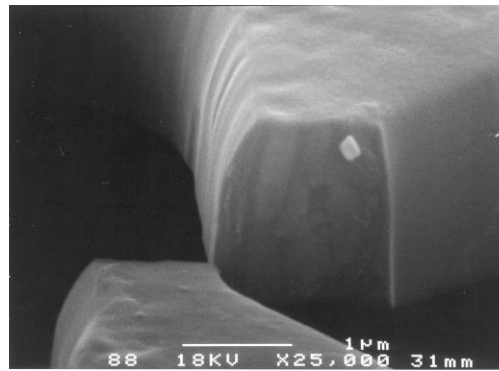
Xiang, H., and Komvopoulos, K., "Effect of Fluorocarbon Self-Assembled Monolayer Films on Sidewall Adhesion and Friction of Surface Micromachines with Impacting and Sliding Contact Interfaces," *Journal of Applied Physics* **113**(22) 224505 (2013).

2.4. Fatigue of Polycrystalline MEMS Devices

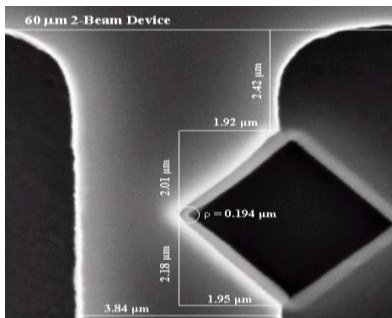
Rapid developments in micromachine devices have increased the need for understanding dynamic material behavior at scales relevant to MEMS. The significance of such information is of paramount importance to the development of reliable MEMS devices capable of performing sensing, actuation, and computing functions in a robust manner. Basic understanding of fatigue at MEMS scales and, more importantly, the effect of process parameters, device dimensions, loading, and environmental conditions is sparse. This research aims to bridge this gap in knowledge through the development of novel microstructures suitable for fatigue testing under conditions typical of most MEMS devices. The main objectives are: (a) develop new microstructure designs appropriate for performing multiaxial fatigue testing at MEMS scales, (b) identify new experimental procedures for fatigue testing under controlled environmental conditions typical of MEMS, and (c) derive fatigue lifetime curves for polysilicon MEMS devices operating in different environments and stress/strain levels.



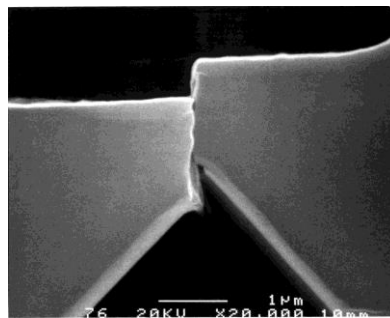
(a)



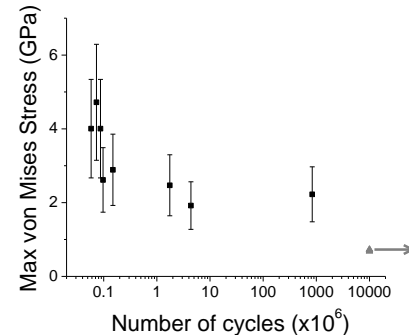
(b)



(c)



(d)



(e)

(a) Three-beam MEMS device for fatigue testing, (b) 3D view of the fractured beam of a fatigued MEMS device, (c) notched beam of a MEMS device, (d) side-view of the fractured beam of a fatigued MEMS device, and (e) stress-life data of MEMS devices fatigued in a vacuum of 10^{-2} Torr.

Selected Publications

Komvopoulos, K., "Electromechanical Devices for Microscale Fatigue Testing," in *Long Term Durability of Structural Materials: Durability 2000*, Eds., Monteiro, P. J. M., Chong, K. P., Larsen-Basse, J., and Komvopoulos, K., Elsevier, Oxford, UK, 2001, pp. 221–230.

Komvopoulos, K., "Microelectromechanical Structures for Multiaxial Fatigue Testing," *Advances in Fracture Research, Proceedings of 10th International Conference on Fracture*, Elsevier, Paper **ICF100217OR**, Honolulu, HI, 3-7 Dec., 2001.

Sun, X., Horowitz, R., and Komvopoulos, K., "Analysis of a Natural Frequency Tracking System for MEMS Fatigue Testing," *Proceedings of 2001 ASME International Mechanical Engineering Congress and Exposition/MEMS*, Paper **23849**, New York, NY, 2001.

White, C. D., Xu, R., Sun, X., and Komvopoulos, K., "Dynamic MEMS Devices for Multi-Axial Fatigue and Elastic Modulus Measurement," *Reliability, Testing, and Characterization of MEMS/MOEMS II*, Eds., R. Ramesham and D. M. Tauner, *Proceedings of SPIE* **4980** 63 (2003).

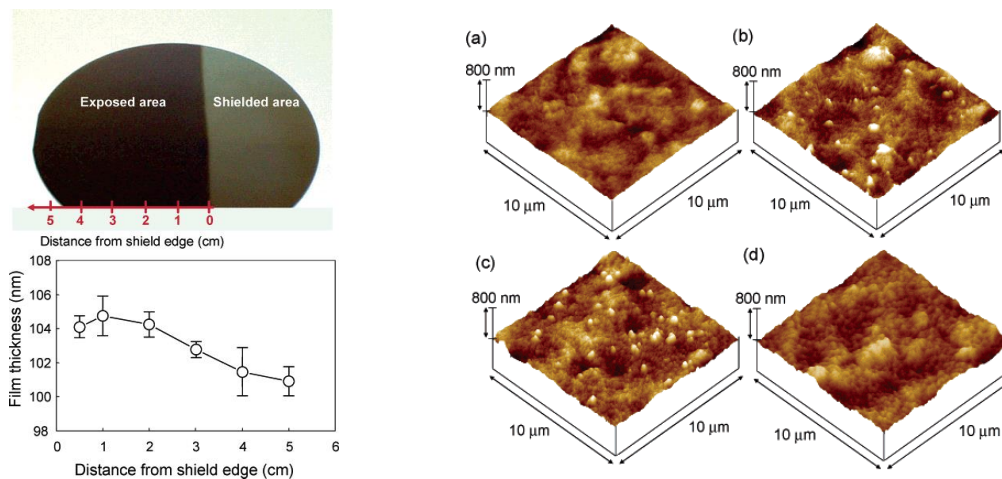
White, C., Xu, R., Sun, X., and Komvopoulos, K., "Characterization of Microscale Material Behavior with MEMS Resonators," *Proceedings of Nanotechnology 2003 Conference* **1** 494 (2003).

Xu, R., and Komvopoulos, K., "A Reduced-Order Dynamic Model of Nonlinear Oscillating Devices," *ASME Journal of Dynamic Systems, Measurement, and Control* **129**(4) 514 (2007).

3. BIOMEDICAL

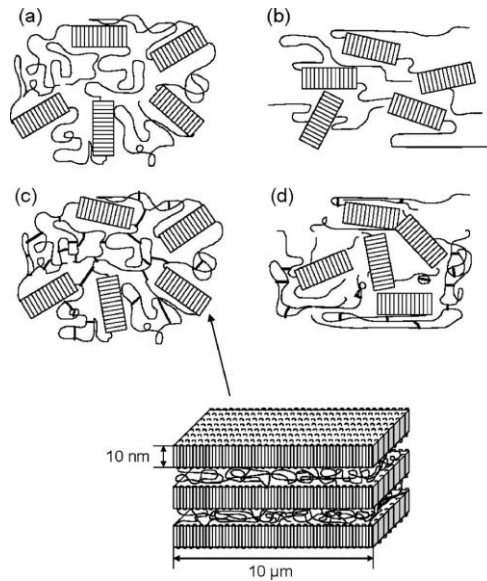
3.1. Plasma-Assisted Surface Modification of Biopolymers

Plasma-assisted surface modification (PASM) of biopolymers is a surface-specific treatment, which, in contrast to conventional bulk treatments, does not alter the bulk properties. Our studies show that unique tailored-made modifications of biopolymer surfaces can be achieved by various PASM treatments. The focus of these studies is the elucidation of the mechanisms controlling surface modification at molecular scales in the context of plasma-polymer surface interactions. Specifically, we have found a strong ion energy fluence effect on surface morphology and surface chemical functionalities of plasma-treated polymer surfaces.



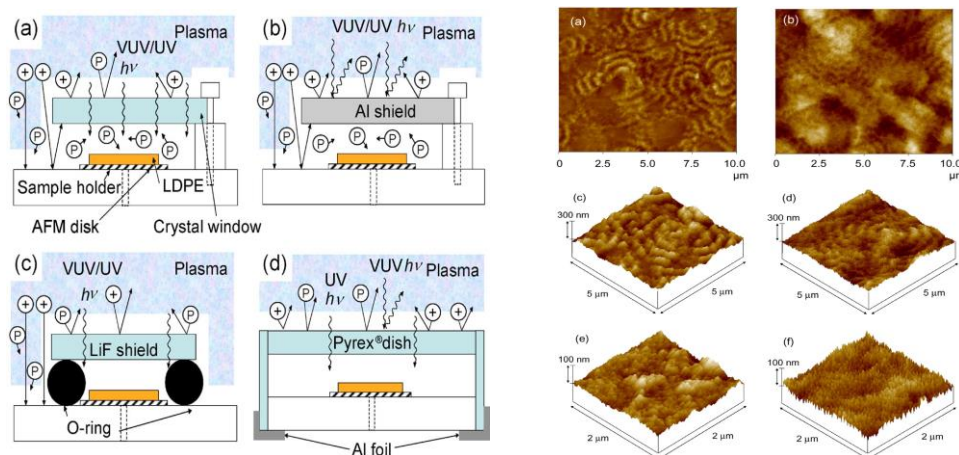
Left: Fluorocarbon film thickness vs distance from the shield edge (unshielded plasma conditions). The locations of the exposed area where the film thickness was measured are shown in the photograph above the film thickness plot.

Right: Microscale surface topographies of (a) Ar-treated LDPE and fluorocarbon films grown under (b) shielded plasma conditions ($W/FM = 66.2$ MJ/kg) and (c,d) unshielded plasma conditions ($W/FM = 22.1$ and 66.2 MJ/kg). (W = plasma power; F = flow rate; M = molecular weight of film precursor (C_4F_8)).



Surface molecular models of (a) untreated LDPE before scratching, (b) untreated LDPE after scratching, (c) cross-linked LDPE before and after scratching with a blunt tip, and (d) cross-linked LDPE after scratching with a sharp tip. The inset at the bottom shows a close view of crystalline lamellae. Chain cross-linking in (c) and (d) is shown by thick solid lines bridging the molecular chains in the amorphous phase.

We have also investigated polymer surface modification by different plasma species (e.g., ions, uncharged particles, and photons) by surface force microscopy. Using crystals of different cut-off wavelengths and a metal shield to deconvolute the effects of individual plasma species, surface crosslinking was shown to be mainly due to the simultaneous effects of uncharged particles and vacuum ultraviolet photons, while the effect of ion bombardment was secondary. A significant increase in the surface shear resistance of plasma-modified polymer surfaces was observed following plasma-induced chain crosslinking, which increased with the ion energy fluence and radiation intensity. An important contribution is the development of a molecular-based model of PASM-treated polymers.



Left: Sample shielding from various plasma species: (a) crystal top shield, (b) Al top shield, (c) LiF top shield and O ring side shield, and (d) Pyrex top and side shield.

Right: AFM images of microscale and nanoscale surface topographies of chemically etched (left column) and plasma-treated (right column) LDPE.

The principal objective of this research is to provide fundamental insight into surface and bulk modification and associated friction and wear processes of biopolymers currently used in various biomedical applications. To achieve this goal, we make use of knowledge derived from surface mechanics, physics, and chemistry studies performed with state-of-the-art experimental techniques to better understand biomaterial phenomena at the nano/micro-scale. The broader impact of this interdisciplinary work is the elucidation of biopolymer surface behaviors, which affect the design of durable biomedical implants and the efficacy of components used in minimally invasive operations.

Selected Publications

Tajima, S., and Komvopoulos, K., "Surface Modification of Low-Density Polyethylene by Inductively Coupled Argon Plasma," *Journal of Physical Chemistry B* **109**(37), 17623 (2005).

Tajima, S., and Komvopoulos, K., "Effect of Ion Energy Fluence on the Topography and Wettability of Low-Density Polyethylene Exposed to Inductively Coupled Argon Plasma," *Journal of Physics D: Applied Physics* **39**(6), 1084 (2006).

Tajima, S., and Komvopoulos, K., "Effect of Reactive Species on Surface Crosslinking of Plasma-Treated Polymers Investigated by Surface Force Microscopy," *Applied Physics Letters* **89**(12), 124102 (2006).

Tajima, S., and Komvopoulos, K., "Dependence of Nanomechanical Modification of Polymers on Plasma-Induced Cross-Linking," *Journal of Applied Physics* **101**(1), 014307 (2007).

Tajima, S., and Komvopoulos, K., "Physicochemical Properties and Morphology of Fluorocarbon Films Synthesized on Crosslinked Polyethylene by Capacitively Coupled Octafluorocyclobutane Plasma," *Journal of Physical Chemistry C* **111**(11) 4358 (2007).

Komvopoulos, K., and Tajima, S., "Method for Depositing Fluorocarbon Films on Polymer Surfaces," *U.S. Patent No. 7,879,418* (2011).

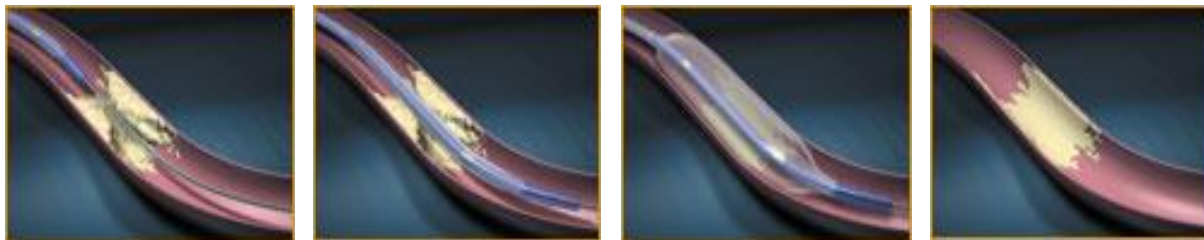
Cheng, Q., and Komvopoulos, K., "Nanoscale Mechanical and Tribological Properties of Fluorocarbon Films Grafted onto Plasma-Treated Low-Density Polyethylene Surfaces," *Journal of Physics D: Applied Physics* **45**(9) 095401(2012).

Komvopoulos, K., and Tajima, S., "Modification of Polymer Surface with Shielded Plasma," *U.S. Patent No. 8,168,074* (2012).

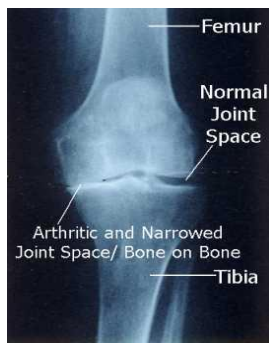
Komvopoulos, K., and Tajima, S., "Method to Control Cell Adhesion and Growth on Biopolymer Surfaces," *U.S. Patent No. 8,927,283* (2015).

3.2. Structural-Chemical Modification of Biopolymer Surfaces

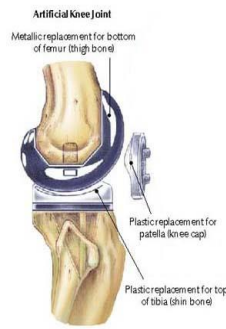
Medical-grade polyethylene is the main material used to make catheters for treating diseased vessels and fabricate parts of artificial joints. Earlier studies in our lab have shown that the topography and chemical behavior of polyethylene used in minimally-invasive procedures (catheterization) and prosthesis (artificial joints) and can be controllably modified by inductively-coupled Ar plasma treatment.



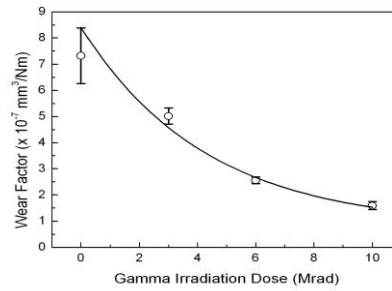
Schematics of the main steps of balloon angioplasty.



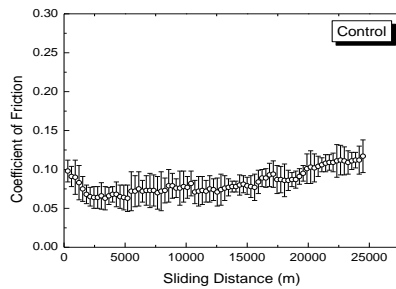
(a)



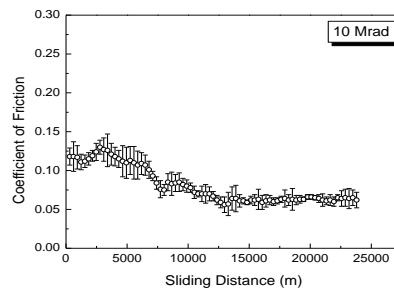
(b)



(c)

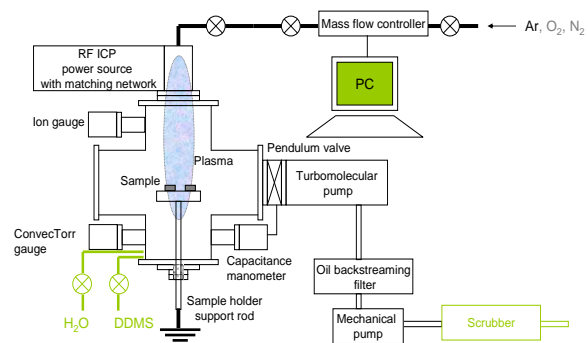


(d)



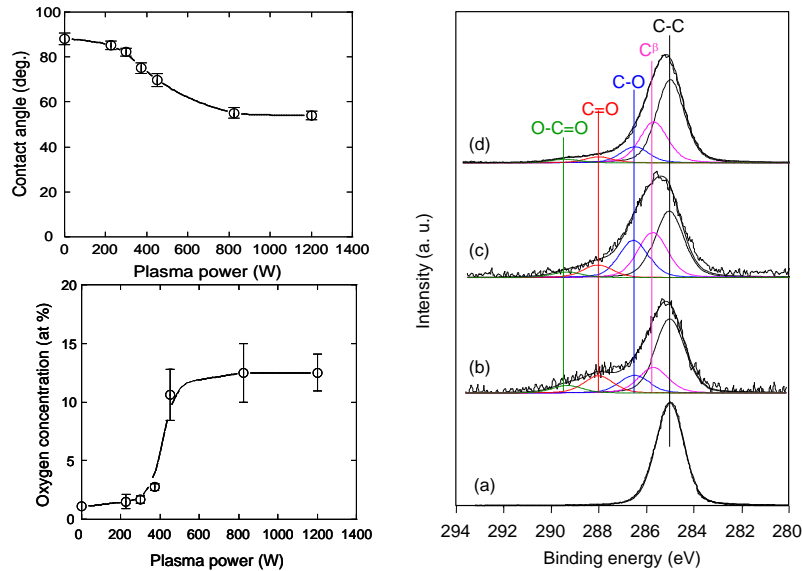
(e)

(a) X-ray photograph of arthritic joint, (b) schematic of total knee joint replacement, (c) wear resistance of UHMWPE vs irradiation dose, and coefficient of friction vs sliding distance for (d) uncrosslinked and (e) crosslinked (by γ -irradiation at 10 Mrad) UHMWPE.



PASM system (left) and schematic configuration of main system components (right).

Our most recent work has been focused on grafting low-friction, biocompatible, molecularly thin layers onto plasma-crosslinked polymer surfaces. We have successfully tuned the degree of crosslinking and chemical structure of grafted fluorocarbon films by shielded-PASM treatment. The PASM method has also been used to synthesize polyethylene-glycol-like films exhibiting remarkable non-fouling behavior against various proteins and cells. We have given particular emphasis on the basic scientific/biomedical aspects of plasma-solid surface interaction at submicrometer scales and the implications of the findings of these studies to *in-vivo* implant performance.



Effect of Ar⁺ plasma power on contact angle and oxygen concentration of plasma-treated LDPE catheters (left) and effect of Ar⁺ ion energy (decreasing from the bottom toward the top of the XPS spectrum) on surface functionalities controlling surface chemical behavior of LDPE catheters (right).

Selected Publications

Komvopoulos, K., "Plasma-Enhanced Modification of Surface Chemistry and Friction Characteristics of Polyethylene Catheters for Cardiovascular Balloon Angioplasty," *Proceedings 11th International Conference on Mechanics in Medicine and Biology*, Maui, Hawaii, 2-5 April, 2000, pp. 133–136.

Komvopoulos, K., "Plasma-Enhanced Surface Modification of Low Linear-Density Polyethylene Catheters," *Journal of Mechanics in Medicine and Biology* **1**(1), 17 (2001).

Komvopoulos, K., Klapperich, C., Pruitt, L., and Kaplan, S. L., "Plasma-Assisted Surface Modification of Polymers for Medical Device Applications," *U.S. Patent No. 6,379,741* (2002).

Zhou, J., Chakravartula, A., Pruitt, L., and Komvopoulos, K., "Tribological and Nanomechanical Properties of Unmodified and Crosslinked Ultra-High Molecular Weight Polyethylene for Total Joint Replacements," *Journal of Tribology* **126**(2), 386 (2004).

Komvopoulos, K., Pruitt, L., Klapperich, C., and Kaplan, S. L., "Plasma-Assisted Surface Modification of Polymers for Medical Device Applications," *U.S. Patent No. 6,685,743* (2004).

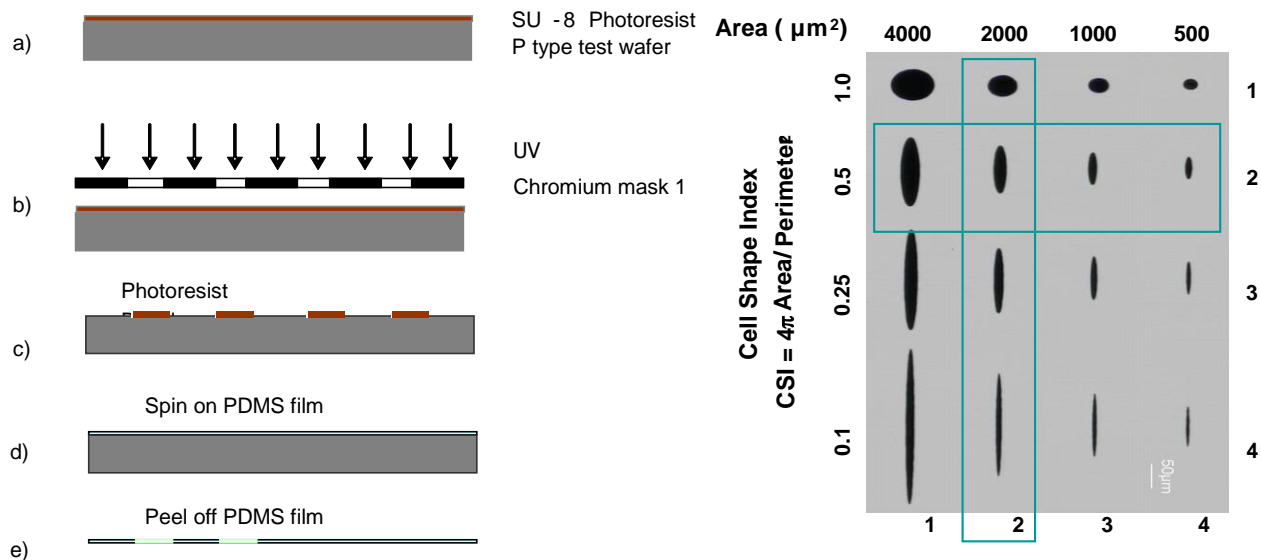
Zhou, J., and Komvopoulos, K., "Wear Mechanisms of Untreated and Gamma Irradiated Ultra-High Molecular Weight Polyethylene for Total Joint Replacements," *Journal of Tribology* **127**(2), 273 (2005).

Cheng, Q., and Komvopoulos, K., "Nanoscale Mechanical and Tribological Properties of Fluorocarbon Films Grafted onto Plasma-Treated Low-Density Polyethylene Surfaces," *Journal of Physics D: Applied Physics* **45**(9) 095401 (2012).

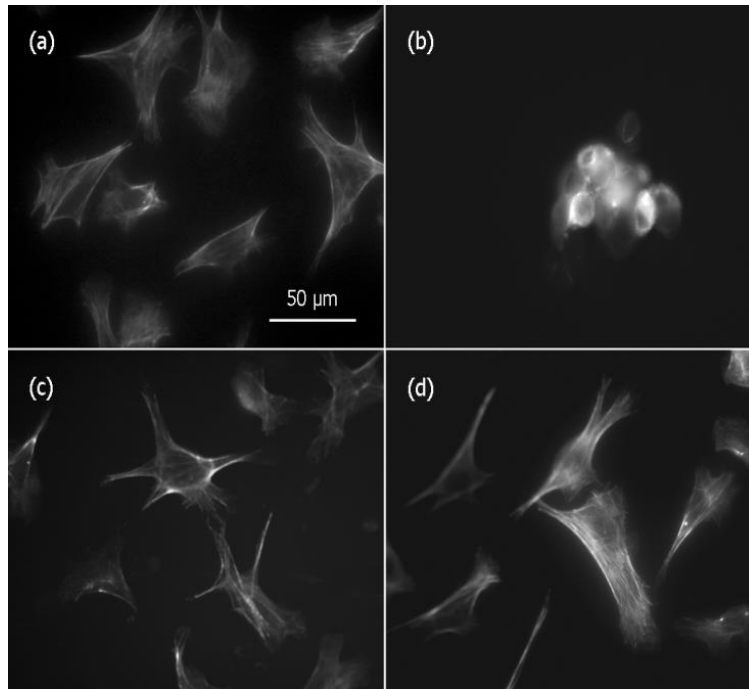
3.3. Plasma-Assisted Surface Modification for Single-Cell Culture

Single-cell patterning is of great importance in cell biology, biosensor technology, and tissue engineering because it can be used to control the cell shape and spreading area, which are known to affect various cell functions, such as migration, division, and differentiation. Our recent work on microscale patterning has led to the fabrication of patterned substrates suitable for studying single cell behavior, which is of critical importance to tissue repair and regeneration. Our research aims to further explore how PASM can be better utilized for single-cell micropatterning.

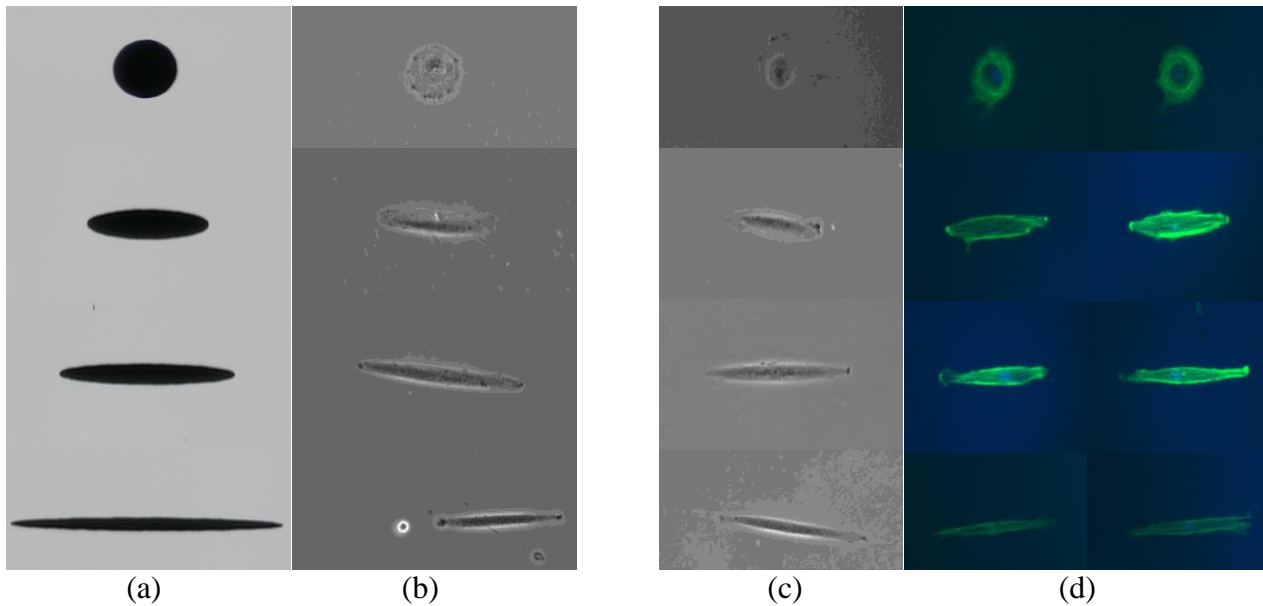
The main theme of this research is the development of novel PASM treatments for single-cell adhesion and culture. By integrating the PASM technique with soft lithography, we can create chemical micropatterns of varying shapes and sizes on different bio-substrates used for single-cell culture. The novelty of our research relies on the development of a simple, cell-sensitive process of surface chemical patterning that combines plasma-assisted polymerization and deposition with plasma etching performed through the windows of a shadow mask fabricated by photolithography. Thus, surface areas for single cell attachment can be obtained by partial plasma etching of the nonfouling layer through the windows of the shadow mask. Special attention is drawn to the identification of correlations between PASM parameters and surface physicochemical properties, which would provide insight into changes in surface biochemical characteristics and, in turn, cell attachment and proliferation. The basic knowledge derived from this research has direct implications in the development of assays for single-cell culture and tissue engineering, and provides insight into the effect of surface nanotopography and chemical cues on cell attachment, growth, and proliferation.



Fabrication process of a PDMS shadow mask (left) and surface micropatterns (right) with cell shape index (CSI) and cell area in the range of 0.1–1.0 and 500–4000 μm^2 , respectively.



Bovine aorta endothelial cells after (a) Ar plasma treatment and (b-d) Ar plasma treatment followed by 30-min diglyme plasma treatment at a power of (b) 1 W, (c) 5 W, and (d) 10 W. The diglyme film in (b) possesses the best nonfouling characteristics, showing significantly reduced cell attachment and spreading.



Representative results from surface chemical micropatterning for single-cell proliferation studies: (a) mask micropatterns of different shapes, (b) and (c) effect of cell shape index and area on SMC proliferation, and (d) actin and nuclear staining of smooth muscle cells of different shapes.

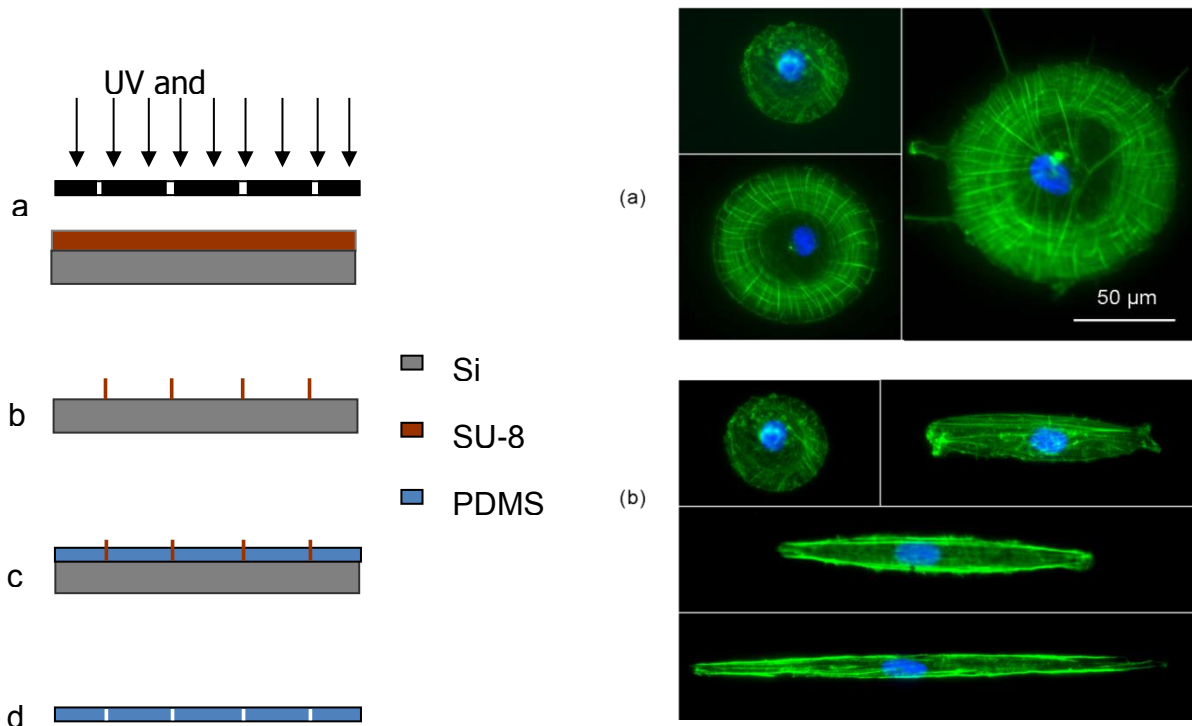


Illustration of the fabrication process of a patterned PDMS substrate with islands of exposed PDMS surrounded by non-fouling PEG-like film (left) and morphologies of human mesenchymal stem cells (right) incubated in serum medium for 24 h and seeded on patterned PDMS substrates with (a) circular and (b) elliptical surface patterns. Note the effect of the surface pattern on the orientation of actin filaments (green) and cell nucleus (blue).

Selected Publications

Tajima, S., Chu, J. S. F., Li, S., and Komvopoulos, K., “Differential Regulation of Endothelial Cell Adhesion, Spreading, and Cytoskeleton on Low-Density Polyethylene by Nanotopography and Surface Chemistry Modification Induced by Argon Plasma Treatment,” *Journal of Biomedical Materials Research, Part A* **84A**(3) 828 (2008).

Cheng, Q., and Komvopoulos, K., “Synthesis of Polyethylene Glycol-Like Films from Capacitively Coupled Plasma of Diethylene Glycol Dimethyl Ether Monomer,” *Journal of Physical Chemistry C* **113**(1) 213 (2009).

Thakar, R. G., Cheng, Q., Patel S., Chu, J., Nasir, M., Liepmann, D., Komvopoulos, K., and Li, S., “Cell Shape-Regulation of Smooth Muscle Cell Proliferation,” *Biophysical Journal* **96**(8) 3423 (2009).

Cheng, Q., Li, S., and Komvopoulos, K., “Plasma-Assisted Surface Chemical Patterning for Single-Cell Culture,” *Biomaterials* **30**(25) 4203 (2009).

Cheng, Q., and Komvopoulos, K., “Integration of Plasma-Assisted Surface Chemical Modification, Soft Lithography, and Protein Surface Activation for Single-Cell Patterning,” *Applied Physics Letters* **97**(4) 043705 (2010).

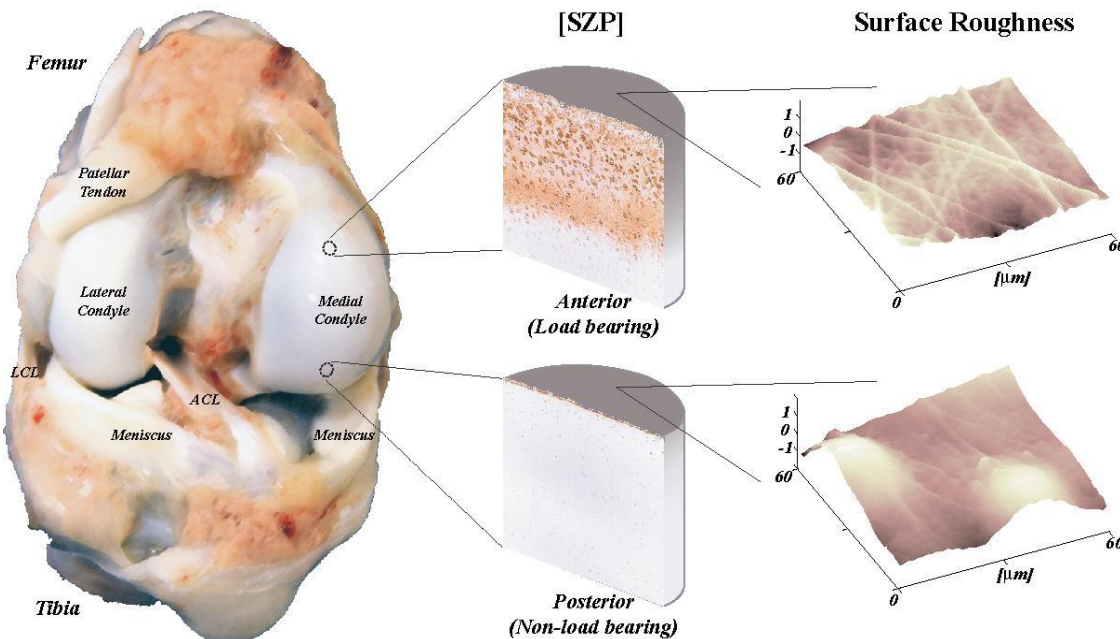
Cheng, Q., Komvopoulos, K., and Li, S., “Surface Chemical Patterning for Long-Term Single-Cell Culture,” *Journal of Biomedical Materials Research, Part A* **96A**(3) 507 (2011).

Tartibi, M., Liu, Y. X., Liu, G.-Y., and Komvopoulos, K., “Single-Cell Mechanics – An Experimental–Computational Method for Quantifying the Membrane–Cytoskeleton Elasticity of Cells,” *Acta Biomaterialia* **27** 224 (2015).

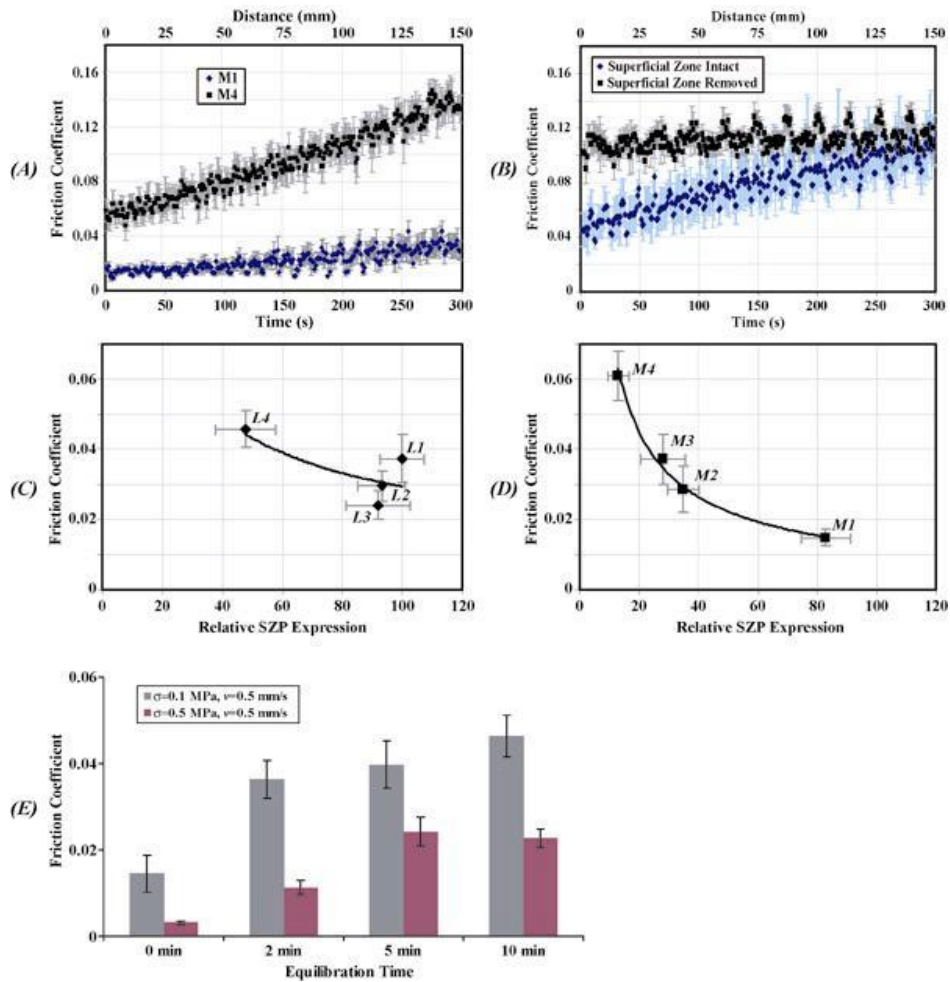
3.4. Mechanotransduction Effects on Protein Secretion from the Superficial Zone of Cartilage and Synovial Joint Degeneration

Cells attached to a substrate convert mechanical stimuli to changes in biochemical activity, a process known as mechanotransduction. Surface irregularities (asperities), adhesion forces, and mechanical stresses exhibit first-order effects on the internal organization of the cytoskeleton and the adhesion of cells to nearby cells and extracellular matrix. The goal of this research is to explore changes in the friction characteristics of bovine articular cartilage due to mechanotransduction and correlate these changes to variations in the near-surface expression of proteins secreted from chondrocytes in the superficial layer of cartilage.

Recent work has demonstrated the existence of an interfacial mechanism of biological regulation and mechanical function in which mechanical forces regulate joint lubrication through biochemical pathways involving the release of various proteins from cartilage DNA. In particular, our work is the first to reveal the role of a key glycoprotein (PRG4) as a friction reducing modifier in joints. The expression level of this protein, secreted from the superficial zone of the cartilage, has been found to correlate with the magnitude of the contact pressure at the joint interface, implying mechanically stimulated protein secretion. Secreted PRG4 molecules form a sacrificial boundary layer, which effectively lubricates the cartilage surface when the synovial fluid is squeezed out from the joint interface. A remarkable finding is that low-friction patterns correspond to regions of high glycoprotein expression and accumulation.



The synovial joint is a living bearing system, which can be studied at different hierarchical levels, from the whole joint scale (bone shape; contact pressure) through the cellular scale (lubricant protein distributions; cellular biosynthesis) to the atomic scale (surface roughness; protein binding). The articular cartilage is a highly organized structure consisting of cells, water, collagens, proteoglycans, and other matrix biomolecules.



Dependence of cartilage friction coefficient on femoral condyle location and SZP expression: (A) The friction coefficient increases linearly with time in all explants tested suggesting the removal of SZP from the articular surface. (B) The removal of SZP increases the friction coefficient. The friction coefficient decreases with the increase of the SZP expression in both lateral (C) and medial (D) condyles. (E) The proof of the sufficiency of a 2 min equilibration time before testing.

More recent work has been centered on the regulation of the PRG4 expression levels by both anabolic and catabolic transformation growth factors, the effect of anatomical differences in PRG4 expression levels under shear loading, and the tribological characteristics of different biomaterials articulated against natural cartilage for hemi-anatomical joint procedures. An ultimate goal is to implement the knowledge derived from the previous studies in engineering scaffolds that can regulate friction by replicating the lubricating function of articular cartilage and explore minimally invasive procedures that will supply cartilage surfaces with appropriate expression levels of specific growth factors and morphogens to improve joint lubricity and suppress cartilage damage by mechanical wear. The results of this research also demonstrate the importance of employing multiple functional assessments (including biochemical and tribological assays) to ascertain the long-term lubricating ability of constructs.

Some of our future objectives are to use the knowledge derived from the previously mentioned studies to engineer scaffolds that would regulate friction by replicating the lubricating function of articular cartilage and exploring minimally invasive procedures for supplying cartilage surfaces with the appropriate expression levels of specific growth factors and morphogens in order to improve joint lubricity and suppress cartilage damage due to mechanical wear. The results of this research program illustrate the importance of employing multiple functional assessments (including biochemical and tribological assays) to ascertain the long-term lubricating ability of constructs.

Selected Publications

Neu, C. P., Khalafi, A., Komvopoulos, K., Schmid, T., and Reddi, A. H., "Mechanotransduction of Bovine Articular Cartilage Superficial Zone Protein by Transforming Growth Factor β Signaling," *Arthritis and Rheumatism* **56**(11) 3706 (2007).

Komvopoulos, K., "Surface Modification and Mechanical Stimulation Effects on Cell Proliferation and Protein Expression on Functionalized Biopolymer Surfaces and Articular Cartilage," *Proceedings of 2nd International Conference on Mechanics of Biomaterials and Tissues* Paper **MB43** (2007).

Neu, C. P., Komvopoulos, K., and Reddi, A. H., "The Interface of Functional Biotribology and Regenerative Medicine in Synovial Joints," *Tissue Engineering B* **14**(3) 235 (2008).

DuRaine, G., Neu, C. P., Chan, S. M. T., Komvopoulos, K., June, R. K., and Reddi, A. H., "Regulation of the Friction Coefficient of Articular Cartilage by TGF- β 1 and IL-1 β ," *Journal of Orthopaedic Research* **27**(2) 249 (2009).

Chan, S. M. T., Neu, C. P., Komvopoulos, K., Reddi, A. H., and Di Cesare, P. E., "Friction and Wear of Hemiarthroplasty Biomaterials in Reciprocating Sliding Contact with Articular Cartilage," *ASME Journal of Tribology* **133**(4) 041201 (2011).

3.5. Scaffolds for Tissue Engineering

Polymer electrospinning is used to fabricate fibrous nonwoven scaffolds. A principal objective is to fabricate scaffolds with controlled structures and fiber organization resembling the structure and function of extracellular matrix and create surface features conducive to cell attachment. To accomplish this goal, silicon wet etching and polydimethylsiloxane (PDMS) molding techniques were combined to construct micropatterned templates, which were used to fabricate fibrous poly(L-lactide) (PLLA) scaffolds by electrospinning. To control the fiber conformity, scaffolds with significantly different fibrous structures were fabricated by varying the geometry of micropattern features on PDMS templates and feed rate of the electrospun polymer solution. Our results show that the developed method can easily be used to fabricate fibrous structures with different characteristics, including fiber alignment, locally high or low porosity (density), and surface microwells of varying shapes and dimensions for various biological applications. The fabricated micropatterned fibrous scaffolds were found to significantly affect the cell morphology and to enhance cell migration *in vitro* and cell infiltration *in vivo*, which are critical factors of cell fate in tissue engineering.

The findings of the previous studies and the work dealing with plasma-assisted surface modification were combined in a series of studies to synthesize scaffolds with surface chemical characteristics promoting cell attachment, growth, and infiltration (in-growth). Cell culture studies performed with electrospun PLLA fibrous scaffolds, which were previously chemically modified with inert (Ar) or reactive (Ar-NH₃/H₂) plasmas, showed that both plasma treatments can effectively improve the spreading and growth of endothelial and smooth muscle cells. The Ar-NH₃/H₂ plasma treatment resulted in more cell spreading, whereas Ar plasma treatment increased more cell proliferation. In addition to

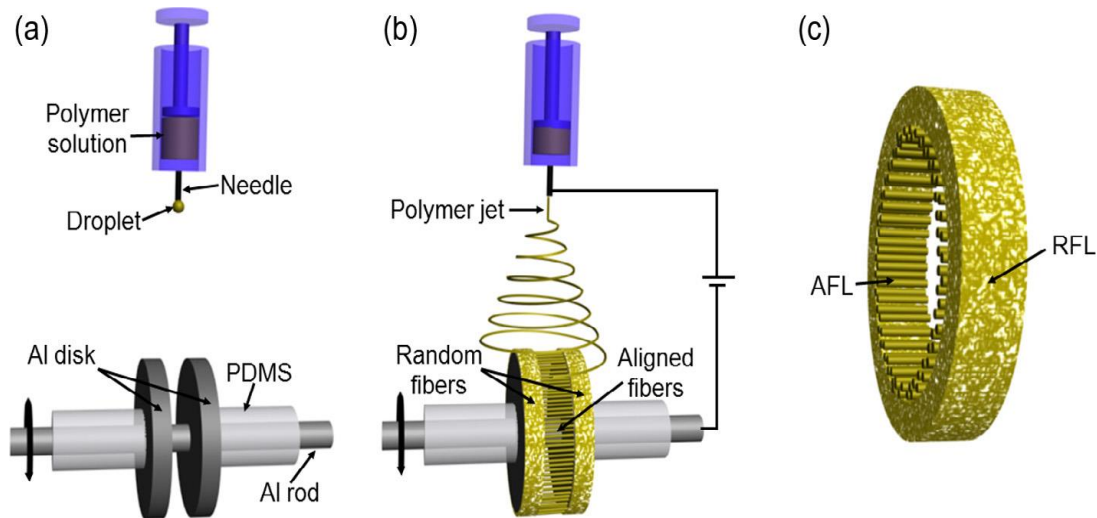
increasing cell adhesion and growth, both plasma treatments induced cell infiltration into the fibrous scaffold structure and resulted in higher cell proliferation rates.

In another study, heparin conjugation of electrospun PLLA fibrous scaffolds was achieved through surface functionalization with amine ($-\text{NH}_2$) groups by sequential scaffold treatment with Ar-NH_3 and H_2 plasmas. Scaffold treatment with these plasmas increased infiltration of bovine aorta endothelial cells *in vitro*, while heparin conjugation further enhanced cell infiltration *in vitro*, independent of the amount of covalently immobilized heparin on plasma-treated scaffolds with a high density of $-\text{NH}_2$ surface functionalities. The improved heparin conjugation achieved with our method is of high importance because it increases the amount and stability of heparin on electrospun scaffolds, thereby improving the anti-thrombogenicity and long-term performance of electrospun vascular grafts. Another important application of this discovery is that heparin-coated electrospun scaffolds can be used for the effective loading and delivery of growth factors, which has broad applications in tissue engineering.

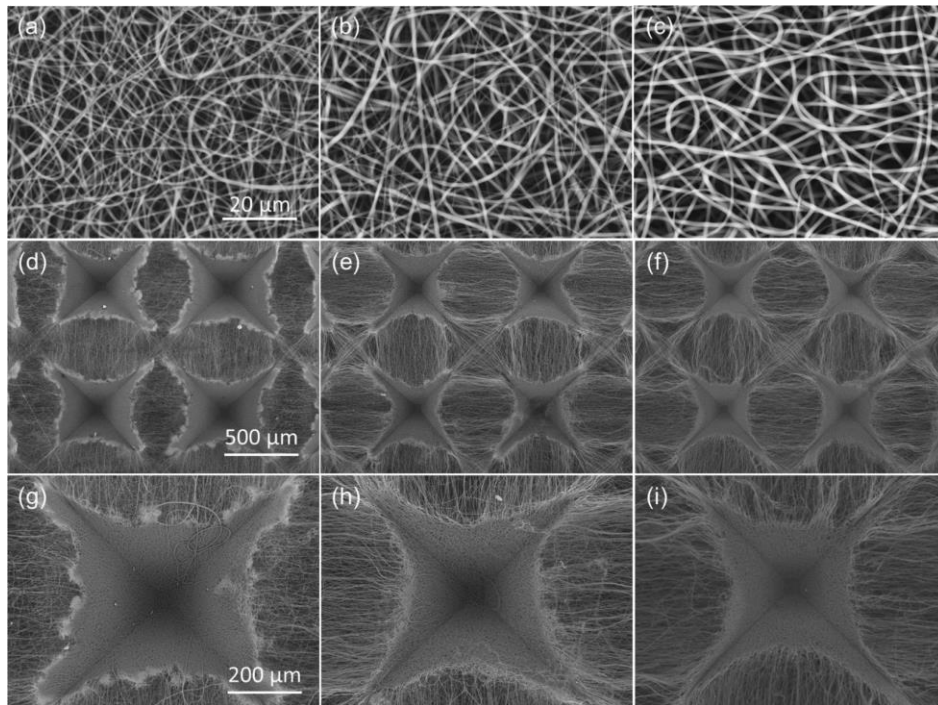
The previous studies provided impetus for the more recent work in this research field. Our interest is to create scaffolds for tissue engineering exhibiting adequate strength and increased biocompatibility. To achieve this goal, we fabricated bilayer fibrous scaffolds consisting of a thin surface layer with aligned fibers (to provide spatial cues resembling native tissue, which can guide cell attachment and growth) and a thicker underlayer with loosely packed and randomly distributed fibers (to promote cell infiltration and tissue growth). Despite the higher porosity of the bilayer scaffolds compared with conventional (single-layer) scaffolds with randomly oriented fibers, the bilayer scaffolds demonstrated significantly better mechanical properties, because the distinctly different deformation behaviors of the two structural layers allowed for gradual delamination and multi-point necking followed by localized fracture of the highly stretched fibers, hence increasing the overall mechanical strength of the scaffold.

We have also evaluated the biocompatibility and biological performance of the former bilayer fibrous scaffolds by *in vivo* experiments involving the subcutaneous scaffold implantation of the scaffolds in Sprague-Dawley rats, followed by histology and immunohistochemistry studies. Our results show that major limitations encountered with conventionally electrospun (controls) scaffolds due to intrinsically small pores, low porosity and, consequently, poor cell infiltration can be overcome with the present bilayer scaffolds. The significantly higher porosity and larger pore size of the layer with random fibers are conducive to cell motility through the scaffold thickness, whereas the relatively dense structure of the layer with aligned fibers provides the scaffolds with the necessary mechanical strength.

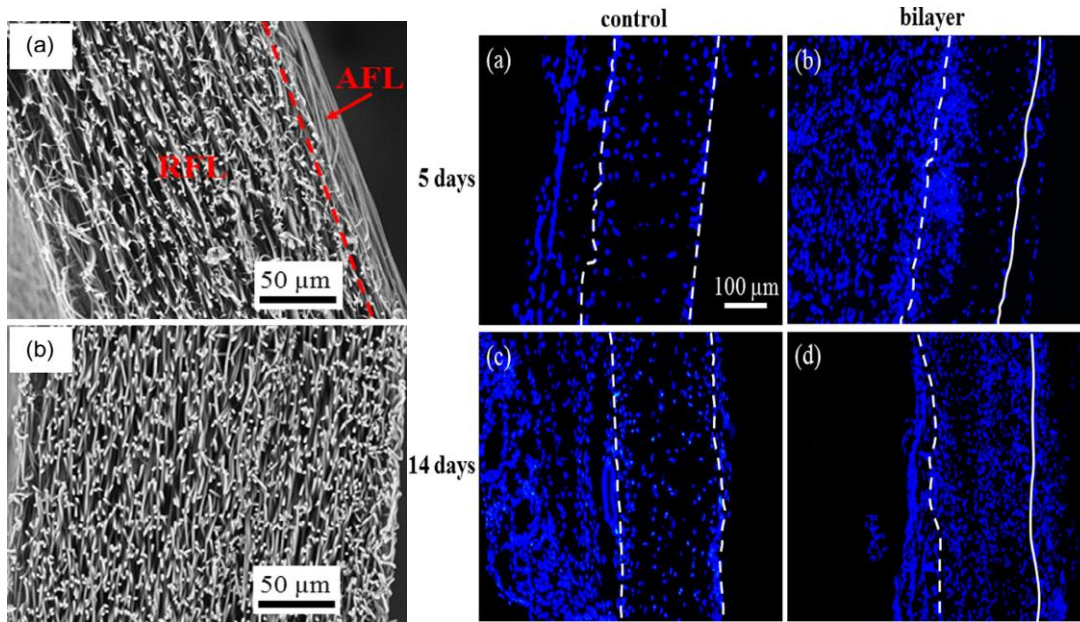
Another impressive characteristic of the bilayer scaffolds is that they show more than two times higher cell infiltration compared with controls (single-layer scaffolds with random fibers) during implantation *in vivo*. The unique structure of the bilayer scaffolds promotes collagen fiber deposition, cell proliferation, and ingrowth of smooth muscle cells and endothelial cells *in vivo*, revealing a high potential of bilayer fibrous scaffolds for tissue engineering and regeneration applications.



(a) Schematic of the present electrospinning process. An aluminum mandrel consisting of a rod and two parallel disks were used to collect the polymer fibers ejected from a needle. (b) Initial fiber deposition results in fiber alignment between the two parallel disks. (c) A bilayer scaffold consisting of an aligned-fiber layer (AFL) and a random-fiber layer (RFL) is produced between the aluminum disks. The formation of the RFL commences as soon as the AFL reaches a critical thickness, which significantly changes the electric field distribution due to the high dielectric constant of the deposited polymer fibers.

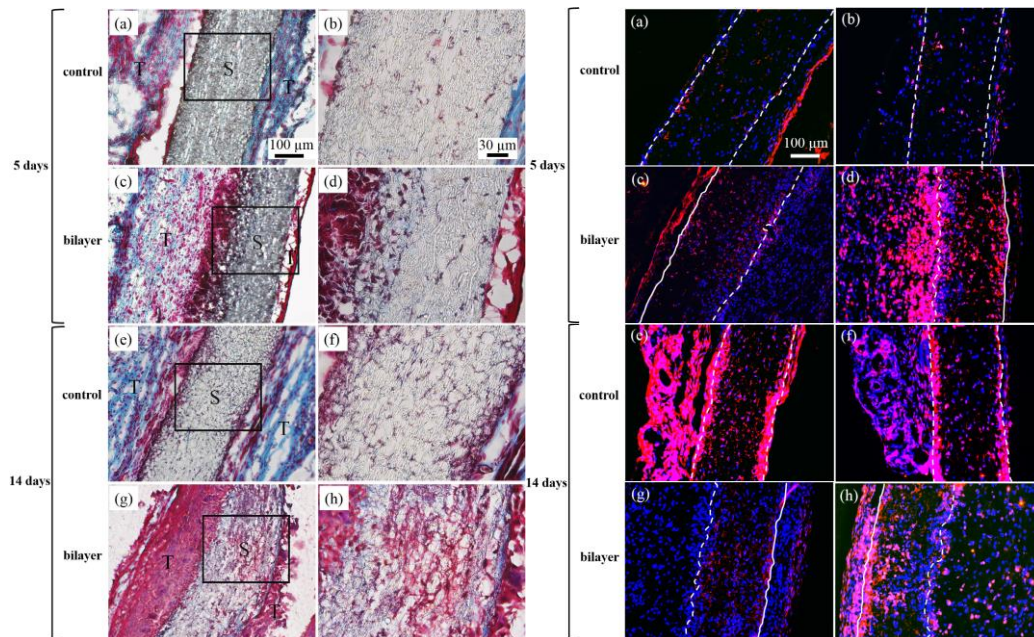


Effect of feed rate of PLLA solution on the micropattern of electrospun PLLA scaffolds: (a)-(c) PLLA fibers deposited on a flat PDMS template, (d)-(f) SEM images of PLLA fibrous scaffolds fabricated on templates with single-slope pyramidal posts (pattern I), and (g)-(i) high-magnification SEM images of the scaffolds shown in (d)-(f) illustrating the formation of individual microwells. Fiber electrospinning was carried out at a feed rate of (a), (d), and (g) 0.2 mL/h, (b), (e), and (h) 0.5 mL/h, and (c), (f), and (i) 2 mL/h.



Left: Cross-sectional SEM images of electrospun (a) bilayer and (b) control scaffolds of thickness equal to ~220 and ~250 μm, respectively. The dashed line shown in (a) indicates the AFL/RFL interface in the bilayer scaffold.

Right: Representative cross-sectional images of (a,c) control and (b,d) bilayer scaffolds subcutaneously implanted in Sprague–Dawley rats for 5 and 14 days confirming cell infiltration *in vivo*. Cell nuclei (blue) were stained with DAPI. Dashed and solid lines represent the boundaries between surrounding tissue and scaffold surfaces with random and aligned fibers, respectively. Aligned fibers are on the right scaffold surface in (b) and (d).



Left: Trichome-stained control and bilayer scaffolds subcutaneously implanted in Sprague–Dawley rats for (a)-(d) 5 days and (e)-(h) 14 days (collagen (blue); muscle (red); cell nuclei (dark purple)).

The cross-sectional images shown in (b), (d), (f), and (h) are enlarged views of regions enclosed by rectangular frames in (a), (c), (e), and (g), respectively. S and T indicate scaffold and surrounding native tissue, respectively. Aligned fibers are on the right scaffold surface in (c), (d), (g), and (h). All images of each column have the same magnification.

Right: Cross-sectional SEM images of electrospun (a) bilayer and (b) control scaffolds of thickness equal to ~220 and ~250 nm, respectively. The dashed line shown in (a) indicates the AFL/RFL interface in the bilayer scaffold. Representative cross-sectional images of control and bilayer scaffolds subcutaneously implanted in Sprague–Dawley rats for (a)-(d) 5 days and (e)-(h) 14 days. Left column: DAPI (nuclei, blue), CD68 (pan macrophages, red). Right column: DAPI (nuclei, blue), Ki67 (cell proliferation, red). Dashed and solid lines indicate the boundaries between surrounding tissue and scaffold surfaces with random and aligned fibers, respectively. Aligned fibers are on the left surface in (c) and (h) and right surface in (d) and (g).

Selected Publications

Cheng, Q., Lee, B. L.-P., Komvopoulos, K., and Li, S., “Engineering the Microstructure of Electrospun Fibrous Scaffolds by Microtopography,” *Biomacromolecules* **14**(5) 1349 (2013).

Cheng, Q., Lee, B. L.-P., Komvopoulos, K., Yan, Z., and Li, S., “Plasma Surface Chemical Treatment of Electrospun Poly(L-Lactide) Microfibrous Scaffolds for Enhanced Cell Adhesion, Growth, and Infiltration,” *Tissue Engineering, Part A* **19**(9-10) 1188 (2013).

Cheng, Q., Komvopoulos, K., and Li, S., “Plasma-Assisted Heparin Conjugation on Electrospun Poly(L-Lactide) Fibrous Scaffolds,” *Journal of Biomedical Materials Research, Part A* **102**(5) 1408 (2014).

Pu, J., and Komvopoulos, K., “Mechanical Properties of Electrospun Bilayer Fibrous Membranes as Potential Scaffolds for Tissue Engineering,” *Acta Biomaterialia* **10**(6) 2718 (2014).

Pu, J., Yuan, F., Li, S., and Komvopoulos, K., “Electrospun Bi-Layer Fibrous Scaffolds for Enhanced Cell Infiltration and Vascularization in Vivo,” *Acta Biomaterialia* **13** 131 (2015).

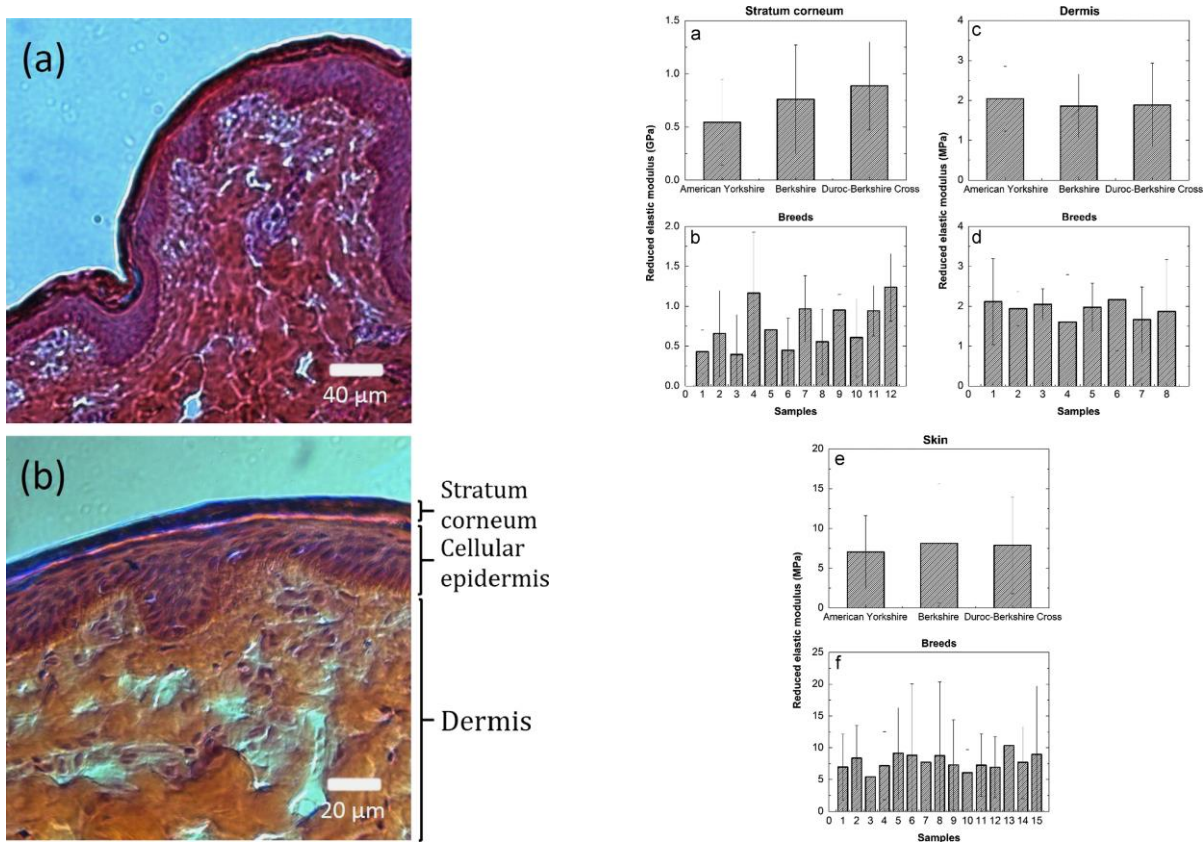
3.6. Skin Mechanics

Aside from teeth, cornea, hair, and nails, human organ surfaces consist of epithelial tissue. The outer epithelial layer (epidermis), commonly referred to as the skin, is the largest organ of the human body providing vital protection to tissue and cells against external intruders, such as bacteria, virus, and fungi, and prevents the loss of water. Unfortunately, very little is known about the mechanical behavior of individual skin layers. Obtaining such knowledge requires the use of microprobe-based methods, such as nano/micro-indentation, which can objectively probe the mechanical response of each skin layer. Thus, the aim of these studies was to examine the mechanical behavior of individual skin layers using nano/micro-indentation techniques and identify the contribution of each skin layer to the overall mechanical behavior of skin.

To accomplish this objective, indentation experiments were performed with porcine skin samples obtained from three different breeds to account for the possible effect of breed type on the measurements. Our results show that irreversible skin deformation commences beyond a critical indentation depth, on the order of the stratum corneum thickness, due to the inadequate support of the highly compliant and soft viable epidermis and dermis. Because the rate of cell and tissue regeneration in injured viable epidermis is much faster than the replenishment rate of stratum corneum by viable epidermis, understanding the role of the mechanical properties of individual layers on irreversible skin deformation is of paramount importance to skin repair. Our results provide insight into the mechanical behavior of skin due to indentation loading, which is of particular importance to minimally invasive

procedures relying on the effective penetration of stratum corneum, such as transdermal drug delivery, local tissue and gene delivery, and blood or interstitial fluid sampling using microneedle-based procedures.

In another investigation, we examined time-dependent deformation of porcine skin *in vitro* using specialized microprobe instruments. The deformation behavior of the stratum corneum, dermis, and whole skin were examined in the context of results of creep strain, elastic stiffness, and viscoelastic constants obtained in terms of hold time, loading/unloading rate, and maximum indentation depth (load). It was found that skin time-dependent deformation is significantly influenced by dermis viscoelasticity up to a critical indentation depth (load) beyond which, it is controlled by the outermost hard epidermis, particularly stratum corneum.



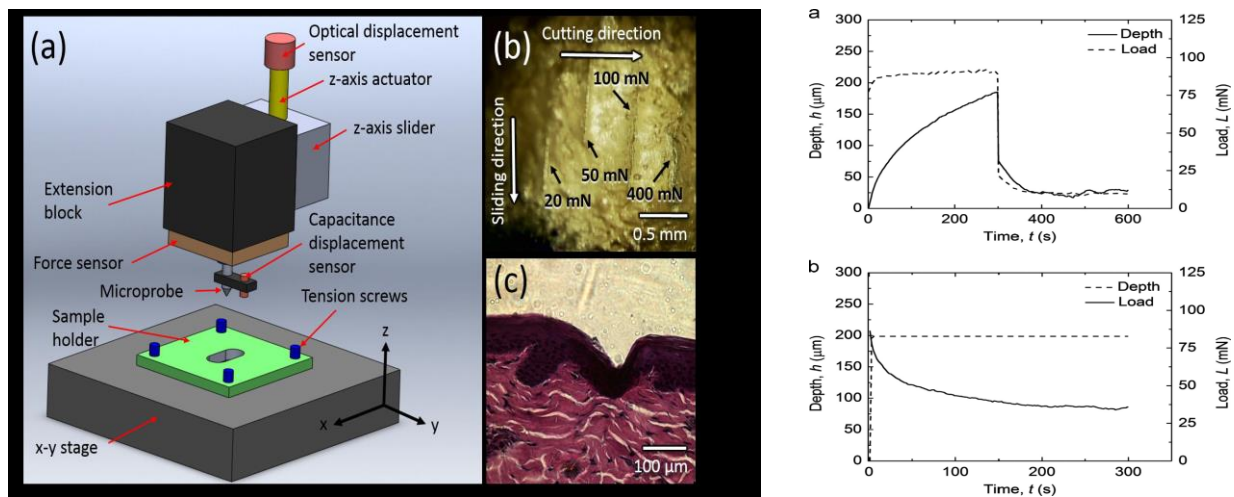
Left: Cross-sectional optical microscopy images of porcine skin (American Yorkshire) at different magnifications. Image (b) shows (from top to bottom): stratum corneum (~10 μm thick), viable epidermis (20–100 μm thick), and dermis (a few mm thick).

Right: Effect of breed type and sample or test order on reduced elastic modulus of (a,b) stratum corneum, (c,d) dermis, and (e,f) skin of three different porcine breeds: American Yorkshire, Berkshire, and Duroc-Berkshire Cross.

Despite the well-recognized importance of the mechanical and tribological properties of skin, the majority of investigations concerned with the mechanical behavior of skin have been performed at macroscopic levels. However, because of the multi-layer skin structure, it is necessary to perform studies at microscopic scales in order to reveal the effect of individual layers on the overall skin response to mechanical stimulus. To bridge this gap of knowledge, we used a custom-made mechanical

tester, optical microscopy, and cross-sectional histology to examine the deformation and tribological behavior of porcine skin subjected to various normal and shear loadings.

Representative friction and wear results of skin tested under unidirectional and reciprocating (cyclic) shearing (scratching) modes were obtained in terms of shearing speed, normal load, and number of scratch cycles to illustrate the effects of stratum corneum, cellular epidermis, and dermis on the friction and wear characteristics of skin. Depending on the normal load and scratch time (cycles), different friction mechanisms (i.e., adhesion, plowing, and squeeze-film lubrication) and different wear mechanisms (i.e., surface plasticity (plowing), bulk shearing, cohesive failure, tearing, and delamination) were found to control shear-induced skin damage. Our work reveals the importance of microscale friction and wear processes on the overall mechanical response of skin subjected to normal and shear surface traction.



Left: (a) Schematic of the microprobe-based mechanical tester used in our studies, (b) optical microscope image showing wear scars on porcine skin produced by a normal load of 20–400 mN, the sliding (scratching) direction, and the cutting direction used to obtain cross-sectional samples for histology analysis, and (c) stained cross-sectional sample showing the formation of a permanent groove on the skin surface without the removal of stratum corneum (normal load $L = 50$ mN).

Right: Representative results of penetration depth h vs time t response of dermis due to (a) step-wise and (b) constant normal load L .

Selected Publications

Jee, T., and Komvopoulos, K., “*In Vitro* Measurement of the Mechanical Properties of Skin by Nano/Microindentation Methods,” *Journal of Biomechanics* **47**(5) 1186 (2014).

Jee, T., and Komvopoulos, K., “Skin Viscoelasticity Studied *in Vitro* by Microprobe-Based Techniques,” *Journal of Biomechanics* **47**(2) 553 (2014).

Jee, T., and Komvopoulos, K., “*In Vitro* Investigation of Skin Damage Due to Microscale Shearing,” *Journal of Biomedical Materials Research, Part A* **102**(11) 4078 (2014).

3.7. Microneedle Arrays for Transdermal Drug Delivery

A transdermal patch is a medicated adhesive patch, which is placed on the skin to deliver a specific dose of medication through the skin and into the bloodstream. An advantage of a transdermal drug delivery

route over other types such as oral or topical is that it enables a controlled release of medicament into the patient's body. A disadvantage to development, however, stems from the fact that the skin is a very effective barrier. To overcome this problem and also increase the number of compounds that can be delivered via the skin, novel transdermal technologies, such as microneedle arrays consisting of tiny needles with diameters smaller than the strand of hair must be developed. The application of the microneedles is painless because they are too small to touch the nerves located deeper into the skin. The main goal of this new initiative is the development of novel microneedle arrays for effective drug delivery through innovations in design and microfabrication and basic understanding of mechanical interactions arising at microneedle/skin sliding interfaces during the operation procedure. Our work relies on knowledge and expertise in microfabrication, microprobe-based nanomechanical testing, surface topography and chemistry modification, tribology, and analytical/numerical modeling of microneedle-skin contact interactions.

This work has direct implications to the design of ambulatory flexible medical devices designed to be attached to the human skin either for short or extended periods without inhibiting normal daily activity. The societal impact of our research is the development of an enabling fabrication technology of microneedle arrays for painless and controllable drug delivery without prevention of the patient's normal activity. Because of the minimal training required to apply these microneedle arrays, flexible ambulatory devices with microneedle arrays may prove useful for immunization programs in developing countries or mass vaccination and antidote administration in bioterrorism incidents.

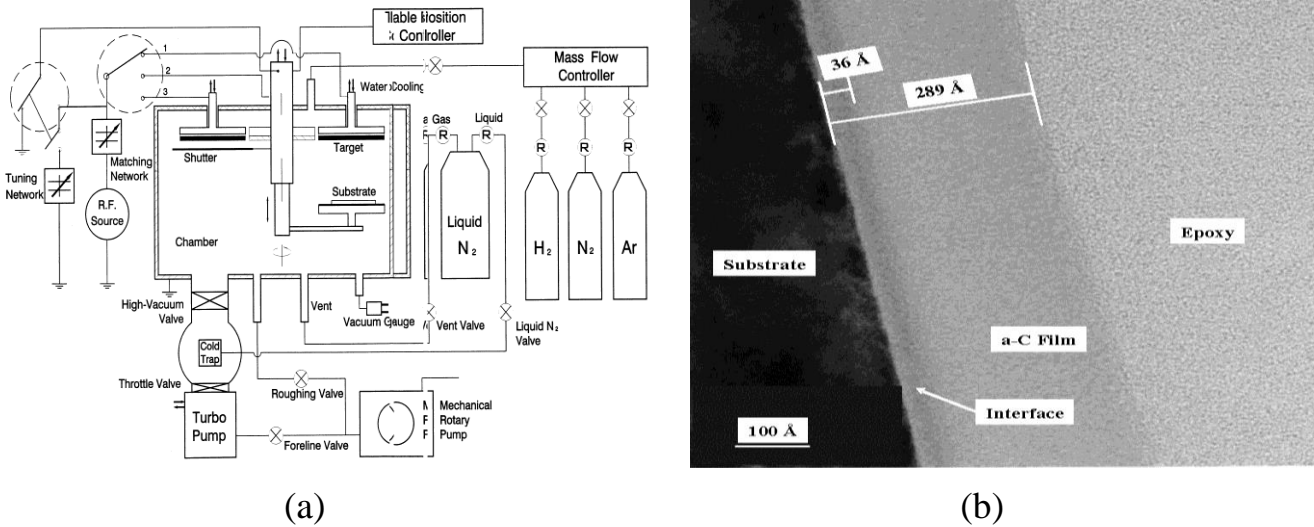
4. Thin Films

4.1. Synthesis and Microstructure Characterization of Ultrathin Carbon Films

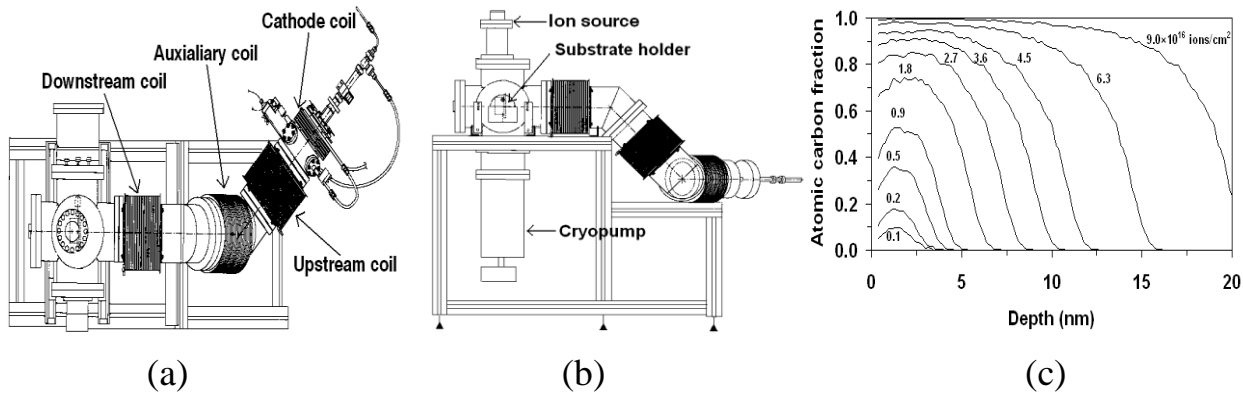
The focus of our recent work in this area is the synthesis, characterization, and structural stability of ultrathin amorphous carbon (a-C) films for use as protective overcoats of the head and disk media of next-generation hard-disk drives. Motivation for this research has been spearheaded by the constantly increasing demands for even higher storage densities, which have led to strict requirements for the thickness, roughness, composition, microstructure, and nanomechanical/tribological properties of the protective a-C overcoats of hard disks and magnetic recording heads. However, continuous overcoats of such small thickness cannot be synthesized by traditional deposition methods, such as sputtering, which has been the workhorse of magnetic recording industry for more than three decades. Thus, new film deposition technologies must be developed to achieve such high information storage densities.

Furthermore, achieving storage densities of 10 Tbit/in² and beyond is restricted by fundamental problems associated with magnetic particle instabilities, high noise-to-signal ratio, and low read/write data rates induced by so-called superparamagnetic limit. Heat-assisted magnetic recording (HAMR) promises to circumvent these difficulties. This new technology uses the optical power of a laser beam, effectively coupled with the magnetic medium of the rotating hard disk, to rapidly heat a track of magnetic medium above its Curie temperature. The instantaneous decrease of the coercivity caused by the intense heat flux allows information to be stored in single bits by the magnetic field of the read/write transducer in the trailing edge of the recording head. However, knowledge of the thermal stability of ultrathin a-C films under localized rapid laser heating conditions is sparse. Therefore, the ultimate objective of our work in this area is to synthesize a-C protective overcoats as thin as 1-3 nm, which also exhibit adequate structural stability under the HAMR operation conditions.

Filtered cathodic vacuum arc (FCVA) is a low-temperature, thin-film deposition technique, which has been under investigation in SSEL since the middle 90's. The demonstrated capacity of FCVA led to the extensive use of this technique in ongoing studies, in conjunction with the traditional method of thin film deposition, i.e., sputtering, a low-pressure plasma discharge process also used in our work to produce a-C films for fundamental studies of carbon atom hybridization.



(a) Schematic of sputtering system and TEM images of (b) cross-section of a thin a-C film deposited on a Si(100) substrate under sputtering conditions of 750 W power, -200 V substrate bias, 20 sccm Ar gas flow rate, and 3 mTorr working pressure.



(a,b) Schematics of FCVA system and (c) carbon depth profiles determined from dynamic simulations for 120 eV kinetic energy of C^+ ions impinging perpendicular to the surface of a Si substrate.

In ongoing work, the FCVA is pushed to its limit to synthesize thermally stable ultrathin (~ 1 - 2 -nm-thick) a-C films for next-generation hard-disk drives. These studies are summarized in the following two sub-sections.

Selected Publications

Zhang, H.-S., and Komvopoulos, K., "Direct-Current Cathodic Vacuum Arc System with Magnetic-Field Mechanism for Plasma Stabilization," *Review of Scientific Instruments* **79**(7) 073905 (2008).

Zhang, H.-S., and Komvopoulos, K., "Synthesis of Ultrathin Carbon Films by Direct Current Filtered Cathodic Vacuum Arc," *Journal of Applied Physics* **105**(8) 083305 (2009).

Zhang, H.-S., and Komvopoulos, K., "Surface Modification of Magnetic Recording Media by Filtered Cathodic Vacuum Arc," *Journal of Applied Physics* **106**(9) 093504 (2009).

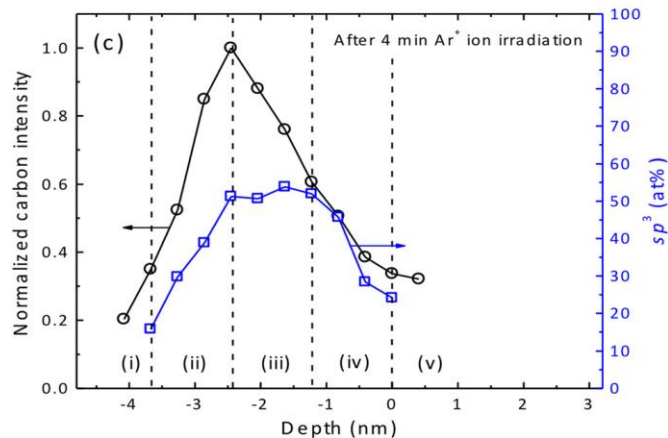
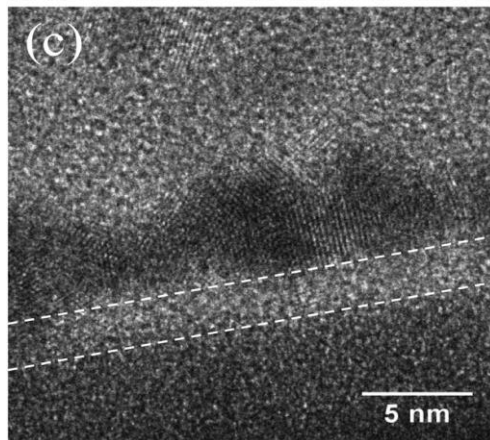
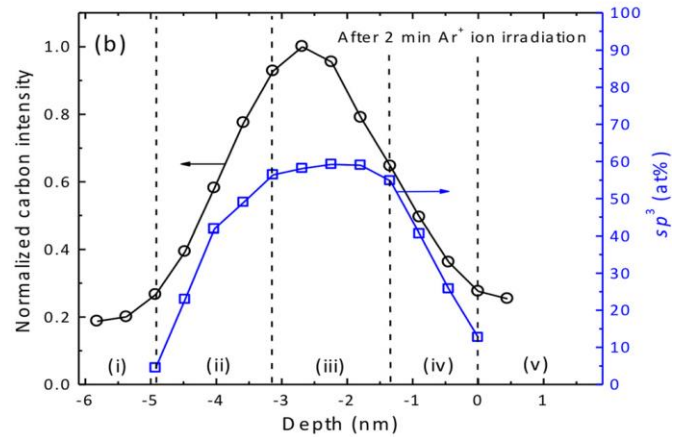
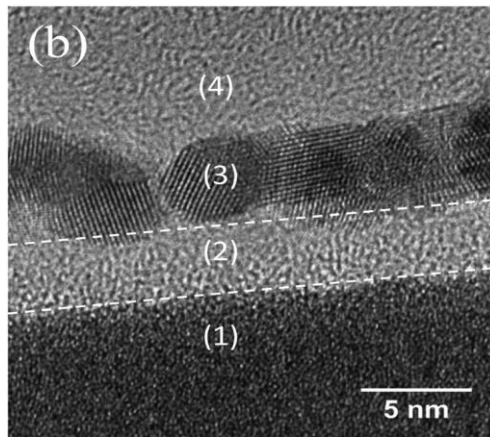
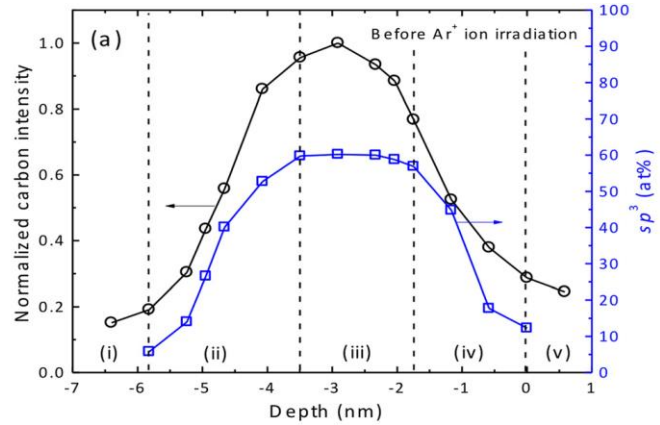
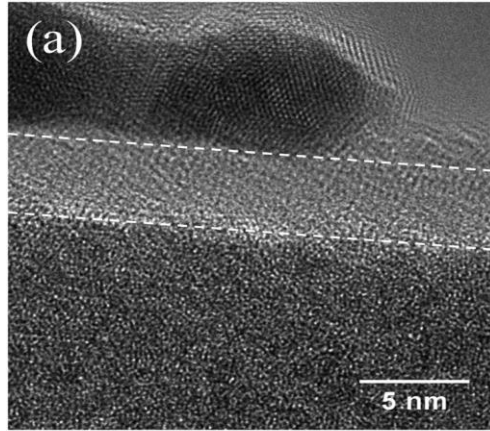
4.1.1. Structure and Tribological Properties of FCVA Ultrathin Carbon Films

The incidence angle of energetic carbon ions significantly affects the deposition rate, topography (roughness), and structure of FCVA-deposited a-C films. Monte Carlo simulations, cross-sectional transmission electron microscopy, atomic force microscopy, and X-ray photoelectron spectroscopy were used to evaluate the effect of the ion incidence angle on the quality of ultrathin a-C films and to determine the optimum incidence angle for FCVA film deposition. It was observed that the a-C film thickness decreases with the increase of the incidence angle, whereas the deposition rate does not depend on ion fluence and varies with the incidence angle according to a relationship derived from classical sputtering theory.

The growth and structure of ultrathin a-C films was further investigated in molecular dynamics (MD) studies, using the second-generation reactive-empirical-bond-order potential to model atomic interaction. The main objective was to elucidate the dependence of short- and intermediate-range order in a-C films on atom deposition energy. MD simulation results of film growth, structure, density, and internal stress have been obtained for a range of carbon atom deposition energy. Short- and intermediate-range carbon atom ordering was interpreted in the context of atomic hybridization and ring connectivity MD results. It was found that relatively high deposition energy (e.g., 80 eV) yields a multilayer film structure consisting of intermixing layer, bulk film, and surface layer, and that the highest film density, content of diamond-like carbon atom hybridization (sp^3), and intermediate-range carbon atom ordering correspond to a deposition energy of ~ 80 eV, which is in good agreement with experimental findings.

Detailed studies of the through-thickness structure of FCVA-deposited ultrathin a-C films were also performed. Depth profiles of carbon atom concentration and sp^3 carbon hybridization confirmed earlier observations of a multilayer film structure consisting of intermixing layer, buffer layer, bulk film, and surface layer.

The minimum thickness of a-C films deposited under the FCVA conditions of -100 V substrate bias was found to be in the range of 3–3.5 nm. The effect of duty cycle of substrate biasing on the structure (hybridization), thickness, residual stress, and roughness of these FCVA a-C films was further examined. A strong effect of duty cycle on carbon atom hybridization and growth, residual stress, and roughness of the films was observed. The results indicate that a-C films of thickness only a few nanometers can be synthesized under FCVA conditions of 65% duty cycle, whereas even thinner films can be synthesized by appropriate adjustment of the ion incidence angle and post-deposition Ar^+ ion sputter etching, which are currently under investigation. The findings of the above studies have direct implications in ultrahigh-density magnetic recording and provide impetus for ongoing studies on a-C films of thickness less than 2 nm.



Left: Cross-sectional HRTEM images of FCVA-deposited a-C film obtained (a) before and after Ar⁺ ion irradiation for (b) 2 min and (c) 4 min. Contrast and structure differences reveal the following regions: (1) NiTa sublayer, (2) a-C film, (3) Au capping layer, and (4) epoxy mounting material (labelled in (b)).

Right: Depth profiles of normalized carbon intensity and sp^3 content calculated from the C K-edge spectra of FCVA-deposited a-C film. The figure shows variations in film structure (a) before and after Ar⁺ ion irradiation for (b) 2 min and (c) 4 min. The boundaries between different regions are distinguished by dashed lines.

In another study we compared the tribological characteristics of FCVA a-C films with sputtered a-C films, which are the protective overcoats of conventional hard-disk drives. Our results show a strong

dependence of the friction properties on the film roughness, thickness, and structure, and that this dependence is affected by the intricacies of each deposition method. The dependence of the coefficient of friction on normal load and the dominance of adhesion and plowing friction mechanisms have been correlated with the through-thickness variation of the carbon atom hybridization of a-C films.

Selected Publications

Wang, N., and Komvopoulos, K., “Incidence Angle Effect of Energetic Carbon Ions on Deposition Rate, Topography, and Structure of Ultrathin Amorphous Carbon Films Deposited by Filtered Cathodic Vacuum Arc,” *IEEE Transactions on Magnetics* **48**(7) 2220 (2012).

Wang, N., and Komvopoulos, K., “The Multilayered Structure of Ultrathin Amorphous Carbon Films Synthesized by Filtered Cathodic Vacuum Arc Deposition,” *Journal of Materials Research* **28**(16) 2124 (2013).

Wang, N., and Komvopoulos, K., “The Effect of Deposition Energy of Energetic Atoms on the Growth and Structure of Ultrathin Amorphous Carbon Films Studied by Molecular Dynamics Simulations,” *Journal of Physics D: Applied Physics* **47**(24) 245303 (2014).

Matlak, J., and Komvopoulos, K., “Friction Properties of Amorphous Carbon Ultrathin Films Deposited by Filtered Cathodic Vacuum Arc and Radio-Frequency Sputtering,” *Thin Solid Films* **579** 167 (2015).

Xie, J., and Komvopoulos, K., “The Role of Duty Cycle of Substrate Pulse Biasing in Filtered Cathodic Vacuum Arc Deposition of Amorphous Carbon Films,” *IEEE Transactions on Magnetics* **51**(12) 3302009 (2015).

Xie, J., and Komvopoulos, K., “The Effect of Argon Ion Irradiation on the Thickness and Structure of Ultrathin Amorphous Carbon Films,” *Journal of Applied Physics* **119**(9) 095304 (2016).

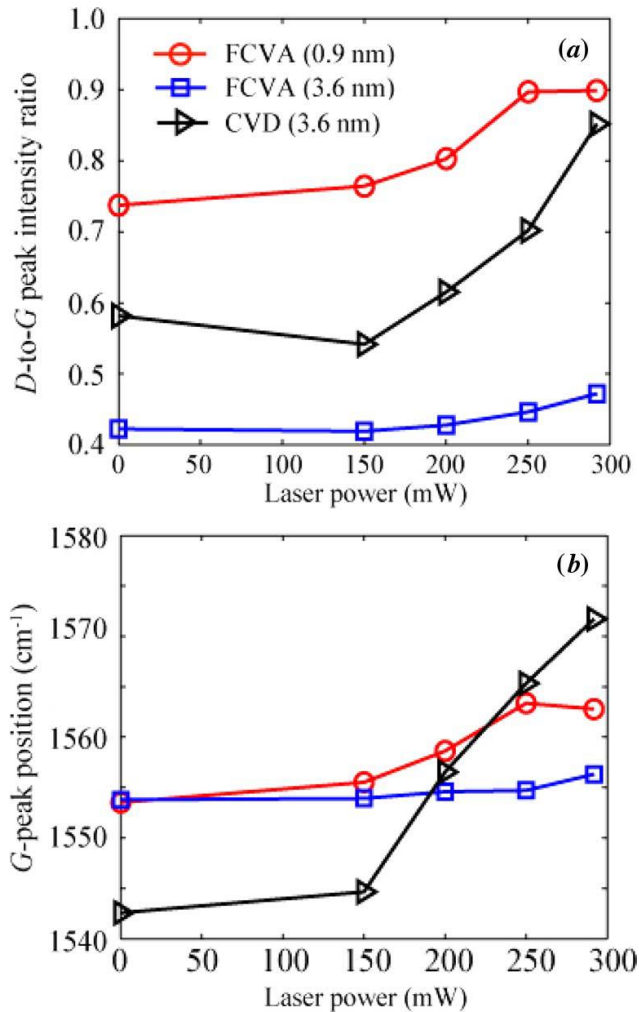
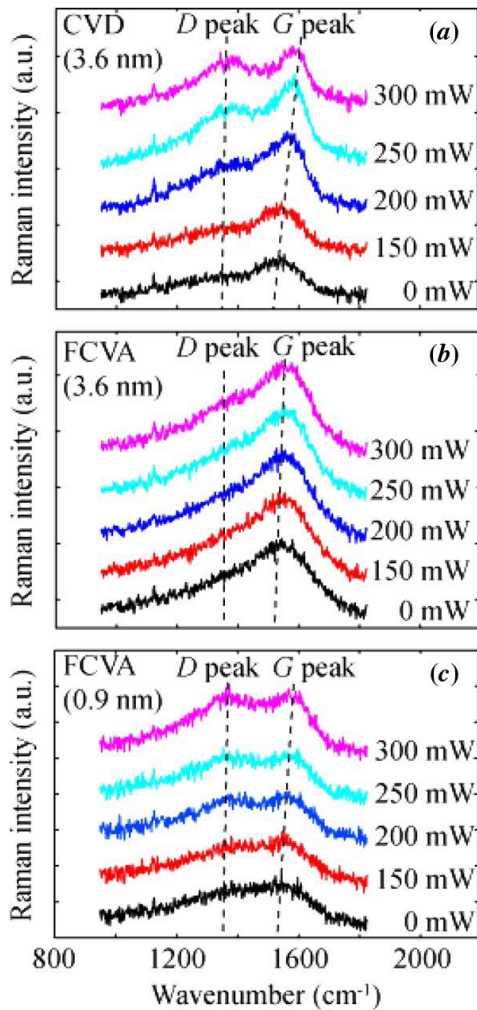
Xie, J., and Komvopoulos, K., “Bilayer Amorphous Carbon Films Synthesized by Filtered Cathodic Vacuum Arc Deposition,” *Journal of Materials Research* **20**(20) 3161 (2016).

4.1.2. Thermal Stability of FCVA Ultrathin Films

To examine the effect of laser heating in HAMR on the overcoat thermal stability, ultrathin a-C films of similar thickness (~3.6 nm) synthesized by FCVA and chemical vapor deposition (CVD) were subjected to cyclic heating at different laser powers. FCVA films demonstrated greater thermal stability than CVD films, which are currently used in HAMR drives. To investigate the possibility of further reducing the magnetic spacing, thinner (~0.9 nm) FCVA a-C films were subjected to the same laser heating conditions. Although the thermal stability of FCVA films demonstrated a thickness dependence, thinner (~0.9 nm) FCVA films demonstrated higher thermal stability than much thicker (~3.6 nm) CVD films, illustrating the high potential of FCVA as the leading coating method for HAMR.

Rapid thermal annealing experiments with ultrathin hydrogenated a-C films deposited by plasma-enhanced CVD showed film thermal stability up to a maximum temperature in the range of 400–450 °C. Heating above this temperature range led to hydrogen depletion and sp^2 clustering. The critical temperature determined in this study represents an upper bound of the temperature rise induced by laser heating in HAMR and, in turn, the Curie temperature of magnetic materials used in HAMR hard disks. In addition, the oxidation rates of FCVA a-C films were found to be lower than those of CVD a-C films by a factor of five, while activation energies of the films were similar, revealing a significant bonding character effect.

All of the studies mentioned in sections 4.1.1 and 4.1.2 provide overwhelming evidence that a-C films synthesized by FCVA are prime candidates as protective overcoats of next-generation hard-disk drives.



Left: Visible Raman spectra of a-C films obtained before and after heating at different laser powers: (a) 3.6-nm-thick CVD film, (b) 3.6-nm-thick FCVA film, and (c) 0.9-nm-thick FCVA film. (The spectra have been shifted upward for clarity.)

Right: (a) D-to-G peak intensity ratio and (b) G-peak position of CVD and FCVA a-C films vs laser power. The results reveal a higher thermal stability for FCVA films.

Selected Publications

Wang, N., and Komvopoulos, K., "Thermal Stability of Ultrathin Amorphous Carbon Films for Energy-Assisted Magnetic Recording," *IEEE Transactions on Magnetics* **47**(9) 2277 (2011).

Wang, N., Komvopoulos, K., Rose, F., and Marchon, B., "Structural Stability of Hydrogenated Amorphous Carbon Overcoats Used in Heat-Assisted Magnetic Recording Investigated by Rapid Thermal Annealing," *Journal of Applied Physics* **113**(8) 083517 (2013).

Pathem, B. K., Guo, X.-C., Rose, F., Wang, N., Komvopoulos, K., Schreck, E., and Marchon, B., "Carbon Overcoat Oxidation in Heat-Assisted Magnetic Recording," *IEEE Transactions on Magnetics* **49**(7) 3721 (2013).

Xie, J., and Komvopoulos, K., "Thermal Stability of Ultrathin Amorphous Carbon Films Synthesized by Plasma-Enhanced Chemical Vapor Deposition and Filtered Cathodic Vacuum Arc," *Philosophical Magazine* (2017) in press.

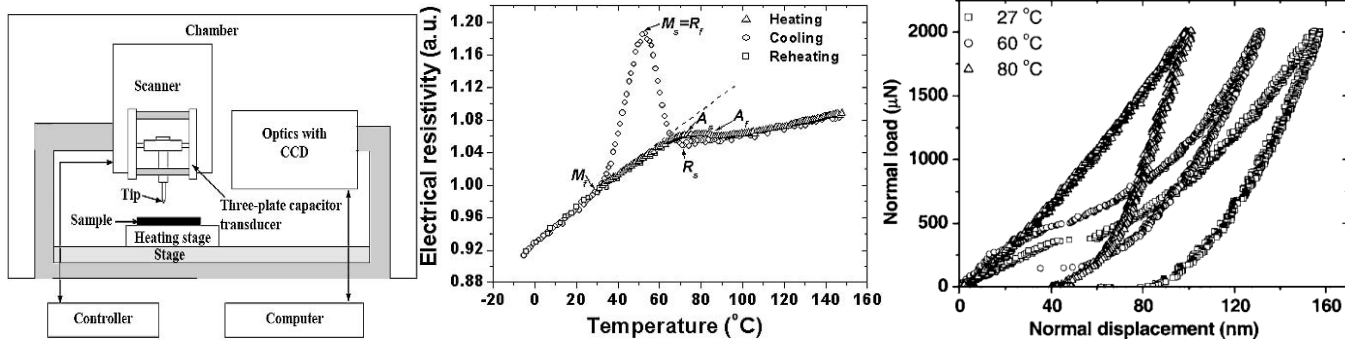
4.2. Phase Transformation Mechanisms and Mechanical Behavior of Shape-Memory Alloys in Film and Bulk Form

Since the initiation of this research program in 2002, significant progress has been made in the analysis of austenite-martensite transformation mechanisms responsible for the pseudoelastic behavior of shape-memory alloys (SMAs), both in film and bulk form. The initial research on TiNi thin films was extended to a more complex SMA material, namely CuAlNi. TiNi and CuAlNi have been selected in our studies due to their high potential as structural materials in various biomedical applications (e.g., stents) and dynamic microdevices (MEMS), resulting from their unique mechanical properties, which are controlled by diffusionless temperature/stress-induced phase transformations. For example, the recovery of very large strains (on the order of 10-20%) by heating or stress relaxation is an intriguing behavior that has not been examined at the nanoscale.

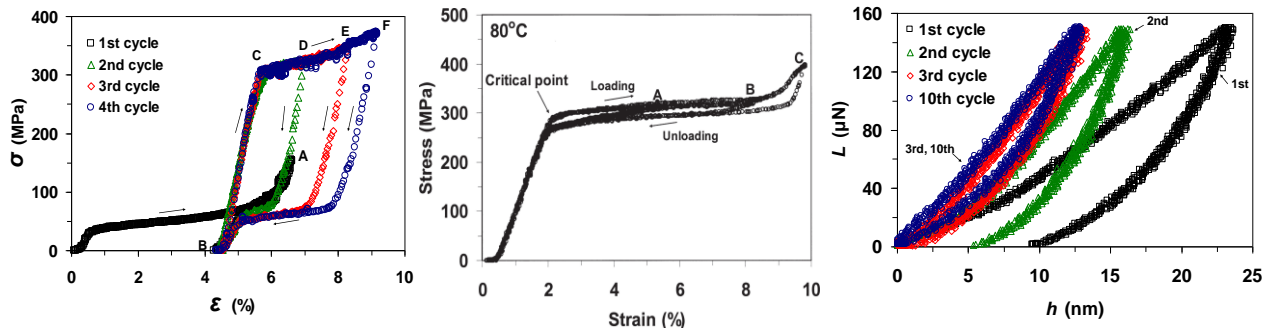
Pseudoelasticity of SMAs has been commonly associated with reversible austenite-martensite phase transformation characterized by shear-induced atomic rearrangement. In contrast to this traditional belief, our *in-situ* heating nanoindentation and TEM studies demonstrate that martensitic TiNi films may also exhibit pseudoelasticity over a specific temperature range by reversible twin boundary movement. The *in-situ* heating nanoindentation responses elucidate the underlying mechanisms of this reversible twin boundary movement and the energy dissipated by pseudoelastic and elastic-plastic deformation in TiNi films. Our experimental evidence is in agreement with a unified description of pseudoelasticity in which the origin of the restoring force responsible for the pseudoelastic behavior of SMAs is the formation of metastable pseudotwins.

The most recent work on the deformation behavior of single-crystal CuAlNi SMA shows some unexpected phenomena. For example, we have discovered that this material can be “trained” to exhibit pseudoelastic behavior by first subjecting it to a cyclic loading up to a certain maximum stress. Stress-strain responses obtained from tensile and nanoindentation tests indicate that this training period corresponds to the stabilization of the γ'_1 phase (the strongest of the four possible martensite phases). Subsequent cyclic loading results in fully reversible martensite-to-martensite phase transformation. Another important contribution of this work is the insight into the nanoscale pseudoelastic behavior of CuAlNi and associated phase transformation mechanisms under cyclic tensile loading. From an application perspective, the intriguing martensite phase transformation and stress-strain response of this SMA can be used to enhance the dynamic agility of MEMS devices. For instance, a captivating concept is nanoscale tuning of the damping ratio by alternating between pseudoelastic responses resulting from austenite-martensite and martensite-martensite phase transformation mechanisms via local temperature control.

We have also observed that tensile testing of single-crystal CuAlNi at elevated and close to phase transformation temperatures produces remarkable stress-strain responses associated with phase transformation phenomena. Formation and coalescence of twin variants affects phase transformation, especially under conditions of partial loading or unloading and varying temperature. The pseudoelastic behavior due to the fully reversible austenite-martensite transformations at elevated temperatures, the formation of the high strength γ'_1 phase at low temperatures, and the high damping ratio obtained by cooling below the martensite finish temperature or by stretching the material at a temperature close to the austenite finish temperature are the most important findings of this work. The unique pseudoelastic behavior and damping ratio of single-crystal CuAlNi SMA illuminate its high potential as structural material in dynamic microdevices exhibiting desirable damping characteristics and sensors enabling *in situ* stress-temperature correlations.



Schematic of nanoindentation system (left), electrical resistivity vs temperature of TiNi films (middle), and nanoindentation responses of TiNi films at different temperatures (right).



- Left:** Stress-strain response of single-crystal CuAlNi alloy at -30°C due to cyclic tensile loading. The first cycle consists of loading up to point A and then unloading to point B. All three consecutive loading cycles begin and end at point B, attaining their corresponding maximum stresses at points D, E, and F. These cycles demonstrate the occurrence of a stable pseudoelastic behavior after the first cycle. Arrows indicate the loading and unloading paths in each stress-strain cycle.
- Middle:** Isothermal stress-strain responses of single-crystal CuAlNi alloy demonstrating pseudoelastic behavior at 80°C . The three overlapping stress-strain curves with maximum stresses denoted by A, B, and C reveal the occurrence of fully reversed deformation and a small hysteresis due to phase transformation.
- Right:** Nanoindentation curves of single-crystal CuAlNi alloy at room temperature showing stable pseudoelastic behavior after three nanoindentation cycles (training period) of $150\ \mu\text{N}$ maximum load.

Selected Publications

- Ma, X.-G., and Komvopoulos, K., "Pseudoelasticity of Shape-Memory Titanium-Nickel Films Subjected to Dynamic Nanoindentation," *Applied Physics Letters* **84**(21) 4274 (2004).
- Wan, D., and Komvopoulos, K., "Thickness Effect on Thermally Induced Phase Transformations in Sputtered Titanium-Nickel Shape-Memory Films," *Journal of Materials Research* **20**(6) 1606 (2005).
- Ma, X.-G., and Komvopoulos, K., "In Situ Transmission Electron Microscopy and Nanoindentation Studies of Phase Transformation and Pseudoelasticity of Shape-Memory Titanium-Nickel Films," *Journal of Materials Research* **20**(7) 1808 (2005).

Komvopoulos, K., and Ma, X.-G., "Pseudoelasticity of Martensitic Titanium-Nickel Shape-Memory Films Studied by *In Situ* Heating Nanoindentation and Transmission Electron Microscopy," *Applied Physics Letters* **87**(26) 263108 (2005).

Zhang, H.-S., and Komvopoulos, K., "Nanoscale Pseudoelasticity of Single-Crystal Cu-Al-Ni Shape-Memory Alloy Induced by Cyclic Nanoindentation," *Journal of Materials Science* **41**(15) 5021 (2006).

Zhang, H.-S., and Komvopoulos, K., "Thermomechanical Effects on Phase Transformations in Single-Crystal Cu-Al-Ni Shape-Memory Alloy," *Journal of Materials Research* **22**(4) 994 (2007).

Zhang, H.-S., and Komvopoulos, K., "*In Situ* Synchrotron X-ray Microdiffraction Analysis of Thermomechanically Induced Phase Transformations in Cu-Al-Ni Shape-Memory Alloy," *Philosophical Magazine* **90**(16) 2235 (2010).

Zhang, H.-S., and Komvopoulos, K., "Nanoscale Pseudoelastic Behavior of Cu-Al-Ni Shape-Memory Alloy Induced by Partial Indentation Unloading," *Nanoscience and Nanotechnology Letters* **2**(4) 332 (2010).

4.3. Viscoelastic Properties of Polymeric Thin Films

Nano-imprinting is one of the most promising fabrication techniques in nanotechnology. Its main feature is the compression of a thin film of a polymer resist by a high-precision stamp into a rigid mold to produce a desirable surface pattern. Since nano-imprinting is a nano-forming process that is greatly dependent on the viscoelastic behavior of the patterned polymer film, basic understanding of the nanoscale viscoelastic behavior and insight into associated nanomechanics are critical for producing extremely small features (on the order of 10 nm) and achieving high pattern quality, reproducibility, and automation. Polymer films are also finding extensive use as overcoats of metallic surfaces because of their high toughness, good transparency, and relatively low density. However, absorption of ultraviolet (UV) radiation due to the exposure to sunlight induces chemical reactions that cause discoloration, significant changes in the surface mechanical properties, and embrittlement leading to peeling off of the polymer film from the substrate. Therefore, our goal in this area was to investigate the nanomechanical response of thin polymer films subjected to quasi-static and dynamic compressive loads and the protection of the polymer films from UV light-induced damage.

Selected Publications

Zhou, J., and Komvopoulos, K., "Nanoconfinement Effect on the Mechanical Behavior of Polymer Thin Films," *Materials Research Society Symposium Proceedings* **880E** BB4.3.1 (2005).

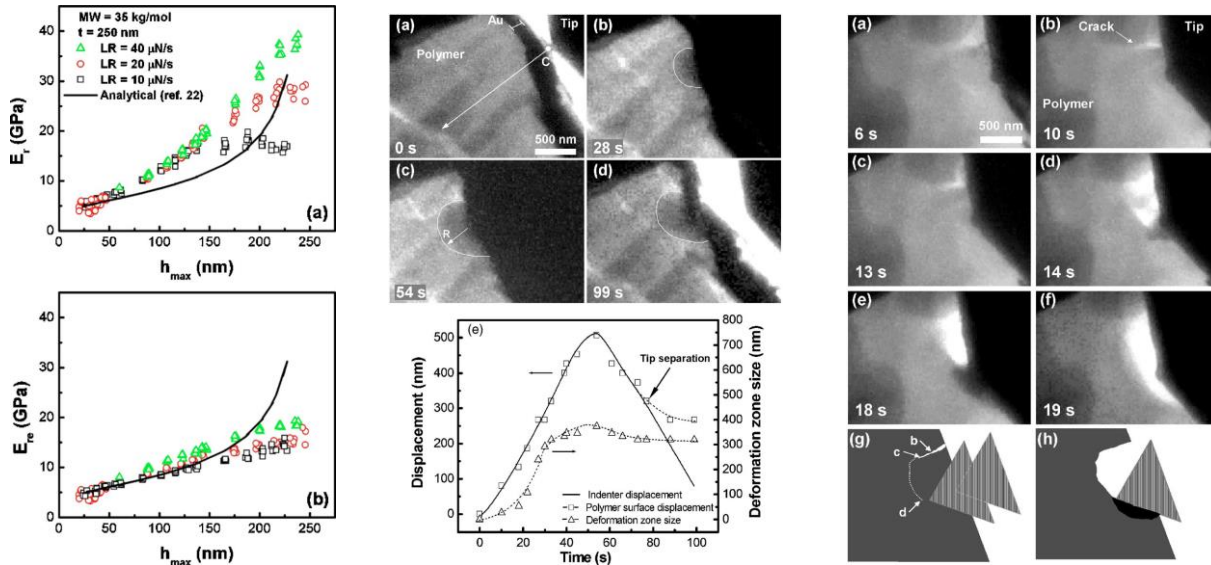
Mailhot, B., Rivaton, A., Gardette, J.-L., Moustaghfir, A., Tomasella, E., Jacquet, M., Ma, X.-G., and Komvopoulos, K., "Enhancement of Polycarbonate Lifetime and Surface Properties by Deposition of Ceramic Coatings," *40th International Symposium on Macromolecules, World Polymer Congress, Macro 2004*, Paris, France, 4-9 July, 2004.

Mailhot, B., Rivaton, A., Gardette, J.-L., Moustaghfir, A., Tomasella, E., Jacquet, M., Ma, X.-G., and Komvopoulos, K., "Enhancement of the Photoprotection and Nanomechanical Properties of Polycarbonate by Deposition of Thin Ceramic Coatings," *Journal of Applied Physics* **99**(10) 104310 (2006).

4.3.1. Quasi-Static Studies of Polymer Thin Films

The nanoscale deformation behavior of polymer films was investigated in nanoindentation experiments performed inside a transmission electron microscope (TEM). *In-situ* TEM observations provided information about the evolution of nanoscale viscoelastic-plastic deformation and fracture at the polymer surface during indentation loading and unloading. In another series of nanoindentation experiments, the effects of the thickness and molecular weight of thin polymer films on the surface and

interface viscoelastic behavior were examined in terms of the loading rate. The novelty of this work is the discovery of three regimes of different viscoelastic behaviors through the polymer film thickness, when it exceeds the unperturbed radius of gyration. The observed loading rate effect on the viscoelastic behavior of indented polymer films led to the development of a confinement molecular-based model that accounts for the restricted molecular chain mobility in the vicinity of the film/substrate interface. This model has important implications in polymer nanostructuring and nanopatterning.



Left: Comparison between analytical (curve) and experimental (symbols) results of reduced elastic modulus vs maximum indentation depth for PMMA films with 35 kg/mol molecular weight and 250 nm thickness subjected to a loading rate of 10, 20, and 40 $\mu\text{N/s}$: (a) as-measured and (b) modified (no viscous contribution) experimental results.

Middle: Characteristic TEM images showing (a) the engagement of the indentation tip with the UHMWPE polymer surface and the development of a deformation zone (high-contrast dark region) underneath the indenter tip during (b) the initial stage of indentation, (c) at maximum indentation depth, and (d) after full unloading. The time elapsed from the onset of indentation is shown at the lower left corner of each image. Results for the tip movement (solid line), the displacement of the polymer surface (square points), and the boundary of the deformation zone (triangular points) along the radial direction shown in (a) are plotted together in (e) for comparison.

Right: TEM images showing the evolution of nanoscale fracture from a surface defect (shallow indentation) in UHMWPE during nanoindentation: (a) initial stage of nanoindentation, (b) crack initiation from the nose of the surface defect, (c) downward crack growth, (d) lateral crack propagation toward the tip and delamination, (e) excessive deformation (high-contrast dark region) adjacent to the tip due to stress concentration induced by the previous delamination, and (f) second delamination event due to stress intensification in the tip vicinity. The previous delamination and deformation processes are shown schematically in (g) and (h), respectively.

Selected Publications

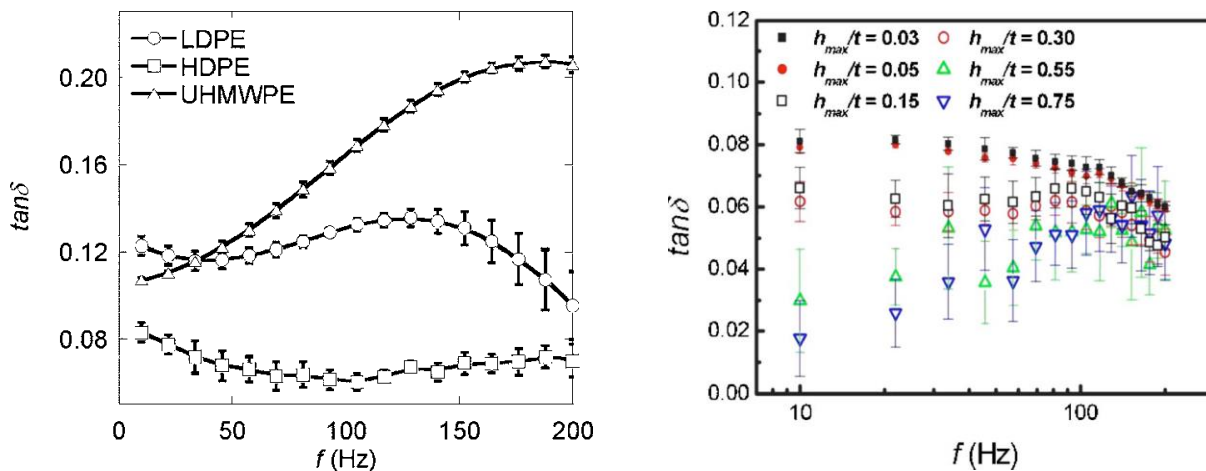
Zhou, J., Komvopoulos, K., and Minor, A. M., "Nanoscale Plastic Deformation and Fracture of Polymers Studied by *In Situ* Nanoindentation in a Transmission Electron Microscope," *Applied Physics Letters* **88**(18) 181908 (2006).

Zhou, J., and Komvopoulos, K., "Surface and Interface Viscoelastic Behaviors of Thin Polymer Films Investigated by Nanoindentation," *Journal of Applied Physics* **100**(11) 114329 (2006).

4.3.2. Dynamic Studies of Polymers

Nanoscale dynamic mechanical analysis (nano-DMA) was used to investigate the viscoelastic properties of polymer surfaces. By varying the driving frequency of an oscillating microprobe tip in contact with the polymer surface, the storage and loss modulus of the polymer were obtained as functions of depth and driving frequency. This work demonstrates that nano-DMA is an effective technique for performing nanoscale studies of the viscoelastic behavior of polymers.

Significant differences were observed between interfacial and bulk viscoelastic properties. In the low-frequency loading range, the interfacial viscous behavior is greatly suppressed because of changes in the molecular chain conformation at the film/substrate interface and the dynamic confinement of the molecular chains between the indenter and the substrate surfaces. Both effects significantly restrict small-scale mobility of the main chains. Alternatively, in the high-frequency loading range, main chain rearrangement is inhibited and short-range side group relaxation is the dominant mode. These results provide new information about the viscoelastic behavior of confined polymer films subjected to dynamic compressive loads, and form an experimental basis for developing constitutive relationships of the viscoelastic deformation of polymers.



Left: Loss tangent of low-density polyethylene (LDPE), high-density polyethylene (HDPE), and ultra-high molecular weight polyethylene (UHMWPE) vs force frequency for relatively shallow nano-indentations (depth <45 nm).

Right: Loss tangent of a thin (200 nm) PMMA film (open symbols) and bulk PMMA (filled symbols) vs frequency for maximum depth-to-film thickness ratio $h_{max}/t = 0.03$ – 0.75 .

Selected Publications

Chakravartula, A., and Komvopoulos, K., "Viscoelastic Properties of Polymer Surfaces Investigated by Nanoscale Dynamic Mechanical Analysis," *Applied Physics Letters* **88**(13) 131901 (2006).

Zhou, J., and Komvopoulos, K., "Interfacial Viscoelasticity of Thin Polymer Films Studied by Nanoscale Dynamic Mechanical Analysis," *Applied Physics Letters* **90**(2) 021910 (2007).

5. Engine Lubrication

5.1. Control of Automotive Emissions

There have been increasing concerns about oil shortages and health threatening particulates from automotive exhausts. Currently, synthetic lubricants for gear and engine components contain additives enriched with chlorine, phosphorous, and sulfur compounds, which provide effective lubrication and protection against wear through chemical reactions with the metal surfaces leading to the formation of antiwear films. Our work in this area aims to discover alternative blends, which can lead to similar or even better energy efficiency and engine performance compared with current blends while, at the same time, minimize the production of hazardous byproducts. Our research in this area began in the mid-90s and has led to the identification of new synthetic blends containing additives which can preserve the engine's efficiency and produce significantly less poisoning of catalytic converters, which not only increases CO_x and NO_x emissions but also negatively affects the combustion process, ultimately reducing the engine efficiency.

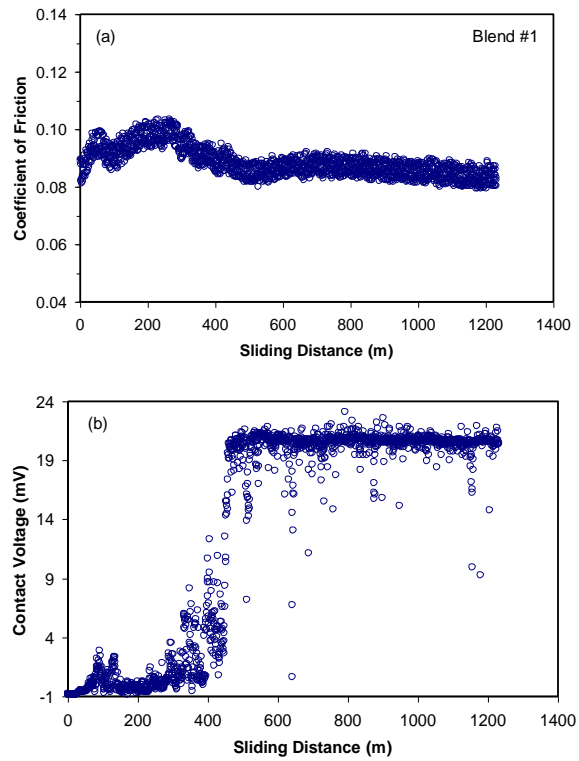
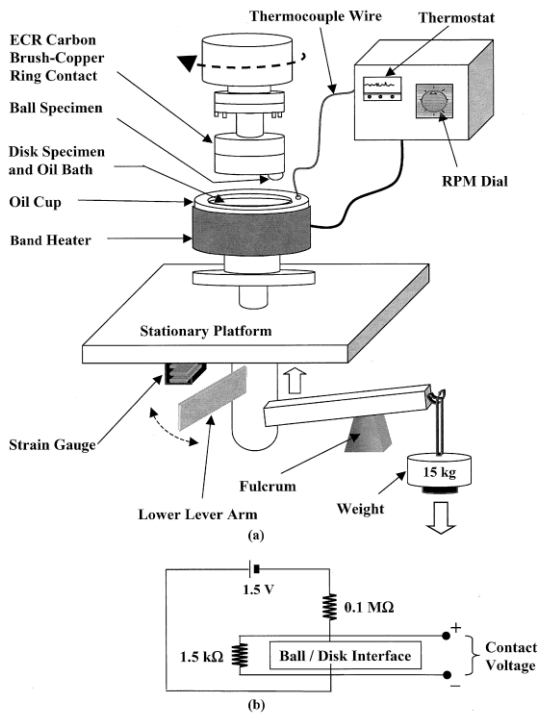
Our earlier studies were directed toward the discovery of new gear blends, whereas recent work has been on new formulations for high-performance car engines. We employ *in-situ* measurements of the coefficient of friction and electrical contact voltage to characterize the tribological performance of alternative blends and study the reaction kinetics and mechanical wear of tribofilms produced from new additives incorporated in each blend. Surface profilometry and scanning electron microscopy are used to further examine the prevailing steady-state wear mechanisms in the presence of new additives, detergents, and dispersants, whereas X-ray photoelectron spectroscopy is used to investigate the chemical composition of forming antiwear tribofilms.

Our lubrication studies elucidate the competing roles of various additive/dispersant compounds on the tribological properties of the produced antiwear films. A most important finding is that phosphorous-containing additives, currently used in all of the automotive oil blends, can be replaced by phosphorus-free additives that do not cause poisoning of the catalytic converter, while, at the same time, produce wear resistant films.

5.2. Anti-wear Additives with Reduced Phosphorus and Sulfur Contents

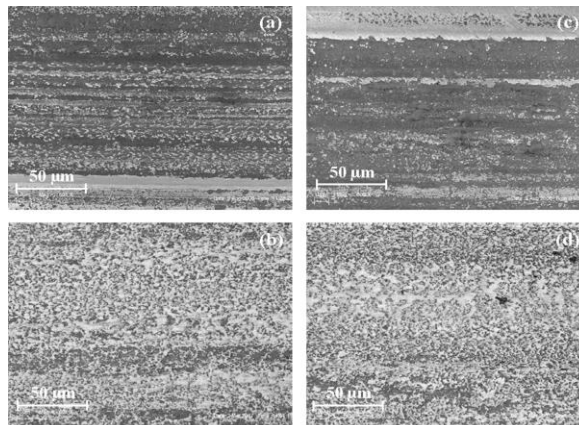
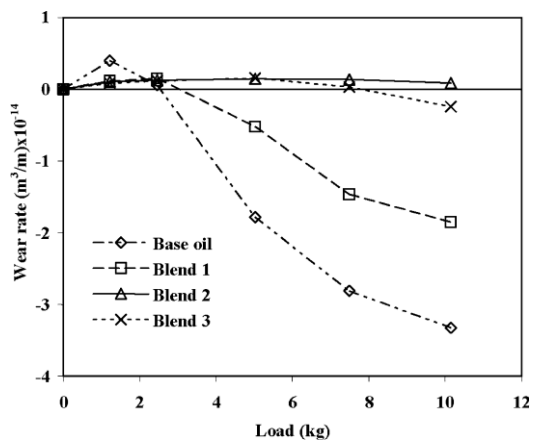
The contribution to air pollution by the automotive industry has been severely criticized in recent years due to the rapidly increasing number of highway drivers. This has led to more stringent regulations for exhaust emissions aimed at offsetting automotive-induced air pollution. The new regulations directly impact oil industries because they necessitate the development of new additives with significantly reduced phosphorus and sulfur contents. Zinc dialkyl dithiophosphate (ZDDP) has been the prime additive of engine oils for many years due to its effectiveness to form self-replenishing anti-wear films that protect the metal surfaces from mechanical wear. Unfortunately, the phosphorous and sulfur in ZDDP produce detrimental effects on the catalytic converter and particle filter of gasoline engines. Phosphorous causes surface poisoning, while sulfur increases the amount of sulfate particles negatively affecting the oxidation catalyst, selective catalytic reaction, and particulate filter. Therefore, the great challenge faced by the engine oil industry is to reduce the amount of ZDDP, while preserving the lubrication efficacy and antiwear performance provided by current oil blends. A plausible solution to this problem is to partially replace ZDDP with a metal dispersant. This is the motivation of our work in this area, which builds on work and experimental protocols derived from our earlier studies in this field.

Our main goal is to provide insight into the competing and antagonistic roles of ZDDP and metal detergents in the formation of antiwear tribofilms that will enable the development of new blends, which are benign to catalytic converters and, therefore, prevent excessive CO_x and NO_x emissions. Experiments performed in the temperature range of 100–125°C with steel specimens fully immersed in a bath of base oil containing ZDDP and a specific detergent show that the best antiwear performance is obtained with a tribofilm formed from a blend containing sulphonate detergent, presumably due to the presence of a hard borate glassy phase in the tribofilm, followed by tribofilms produced from blends containing overbased phenate and salicylate detergents. Work in progress is expected to provide additional insight into the synergistic and antagonistic effects between ZDDP and metal dispersants affecting antiwear film performance.



Left: Schematic illustration of (a) ball-on-disk tribometer and (b) electrical circuit used to measure the voltage drop across the contact interface.

Right: Variation of (a) coefficient of friction and (b) contact voltage with sliding distance for B-, P-, and S-containing blend #1 at ~100°C oil temperature.



Left: Wear rate vs normal load for different oils.

Right: SEM micrographs of wear tracks on steel surfaces: (a) blend 2 (load = 1.22 kg), (b) blend 2 (load = 10.15 kg), (c) blend 3 (load = 1.22 kg), and (d) blend 3 (load = 10.15 kg).

Selected Publications

Komvopoulos, K., Chiaro, V., Pakter, B., Yamaguchi, E. S., and Ryason, P. R., "Antiwear Tribofilm Formation on Steel Surfaces Lubricated With Gear Oil Containing Borate, Phosphorus, and Sulfur Additives," *Tribology Transactions* **45**(4) 568 (2002).

Komvopoulos, K., Do, V., Yamaguchi, E. S., and Ryason, P. R., "Effect of Sulfur- and Phosphorus-Containing Additives and Metal Deactivator on the Tribological Properties of Boundary-Lubricated Steel Surfaces," *Tribology Transactions* **46**(3) 315 (2003).

Komvopoulos, K., Do, V., Yamaguchi, E. S., Yeh, S. W., and Ryason, P. R., "X-ray Photoelectron Spectroscopy Analysis of Antiwear Tribofilms Produced on Boundary-Lubricated Steel Surfaces from Sulfur- and Phosphorus-Containing Additives and Metal Deactivator Additive," *Tribology Transactions*, Vol. **47**(3) 321 (2004).

Komvopoulos, K., Do, V., Yamaguchi, E. S., and Ryason, P. R., "Nanomechanical and Nanotribological Properties of an Antiwear Tribofilm Produced from Phosphorus-Containing Additives on Boundary-Lubricated Steel Surfaces," *ASME Journal of Tribology* **126**(4) 775 (2004).

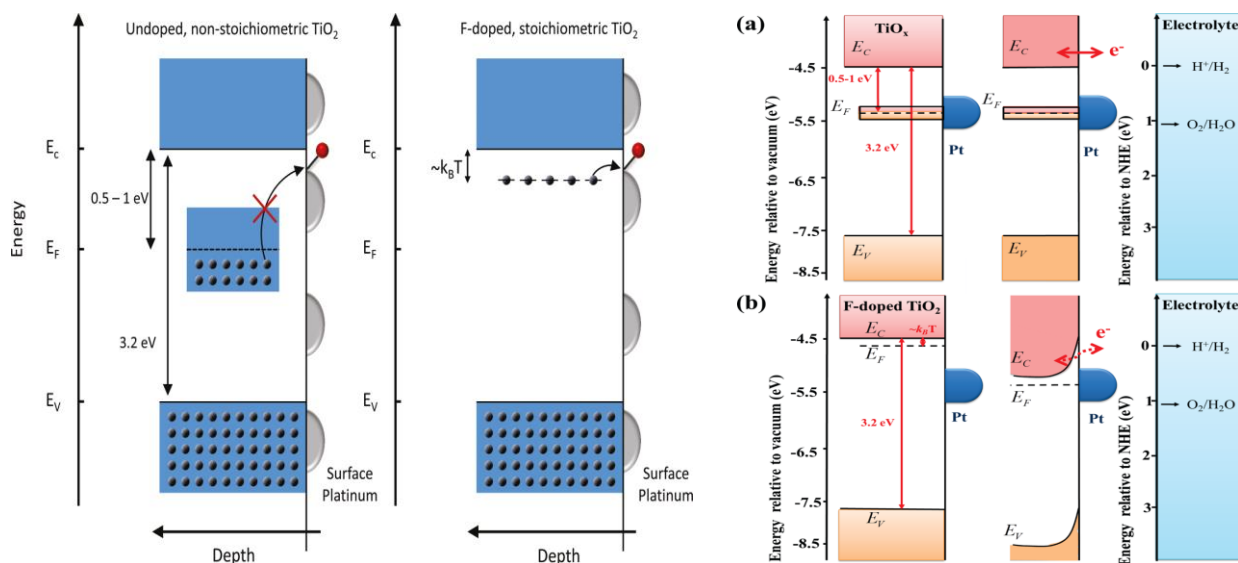
Komvopoulos, K., Pennecot, G., Yamaguchi, E. S., and Yeh, S. W., "Antiwear Properties of Blends Containing Mixtures of Zinc Dialkyl Dithiophosphate and Different Detergents," *Tribology Transactions* **52**(1) 73 (2009).

6. Energy

6.1. Electronic Tuning of Active Substrates to Enhance Catalyst Reactivity

Most industrial catalysts consist of metal particles supported by a porous oxide substrate. This not only provides a high surface area for the heterogeneous catalyst, but the oxide support also plays an important role in determining the activity and selectivity of the catalyst. The role of support material in electronic activation of surface chemistry was examined in a series of novel studies. A most important finding is the ability to tune the electronic structure of metal-oxide semiconductors used as catalyst supports to provide access to reaction pathways not thermally accessible with other catalysts. For example, we have found that electron flow from a titanium oxide (TiO_x) substrate to surface adsorbates can significantly increase the catalytic reaction rate by activating surface oxygen atoms to react with adsorbed carbon monoxide.

For the first time, studies of methanol oxidation over Pt/TiO_x catalysts showed that the electronic structure of the TiO_x oxide support can be tuned by fluorine doping to control the oxidation pathways on the Pt catalyst surface. More recently, we discovered that significantly enhanced electrocatalytic performance can also be achieved in important fuel cell reactions through oxide support modification by either adding oxygen vacancies or fluorine doping. The results of the latter studies provide guidance for selecting the support material of Pt/TiO_x catalyst systems and can also be applied to other metal-oxide support materials. Thus, our work has direct implications in the design and optimization of fuel cell catalyst supports.



Left: Schematic of the charge transfer mechanism in nonstoichiometric TiO_x and F-doped stoichiometric TiO₂. In the presence of mid-gap states, electron transfer from the oxide to an adsorbate species involves an electron with energy between 0.5 and 1.0 eV below the bottom of the conduction band. In the case of F-doped TiO₂, donor electrons occupy states at the bottom of the conduction band that were previously not thermally accessible. These higher energy electrons may transfer to an adsorbate species, resulting in higher turnover frequency and enhanced selectivity toward partial oxidation.

Right: Schematic of charge transfer mechanism in (a) nonstoichiometric TiO_x and (b) F-doped stoichiometric TiO₂. The mid-gap states in TiO_x produce a relatively low Fermi level, assisting in electron transfer from the oxide to adsorbed species. However, in the case of F-doped TiO₂, an energy barrier (band bending) is produced to maintain equilibrium, which inhibits electron transfer and, in turn, chemical reaction.

(E_C, E_F, and E_V denote conduction, Fermi, and valence energy levels, respectively.)

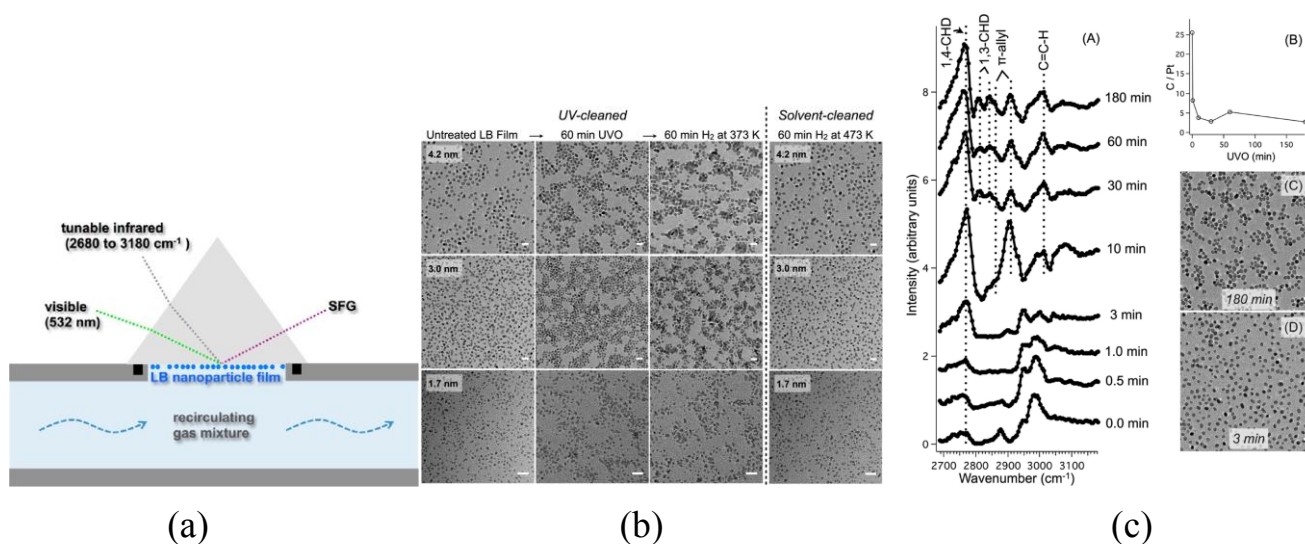
Selected Publications

Hervier, A., Baker, L. R., Komvopoulos, K., and Somorjai, G. A., "Titanium Oxide/Platinum Catalysis: Charge Transfer from a Titanium Oxide Support Controls Activity and Selectivity in Methanol Oxidation on Platinum," *Journal of Physical Chemistry C* **115**(46) 22960 (2011).

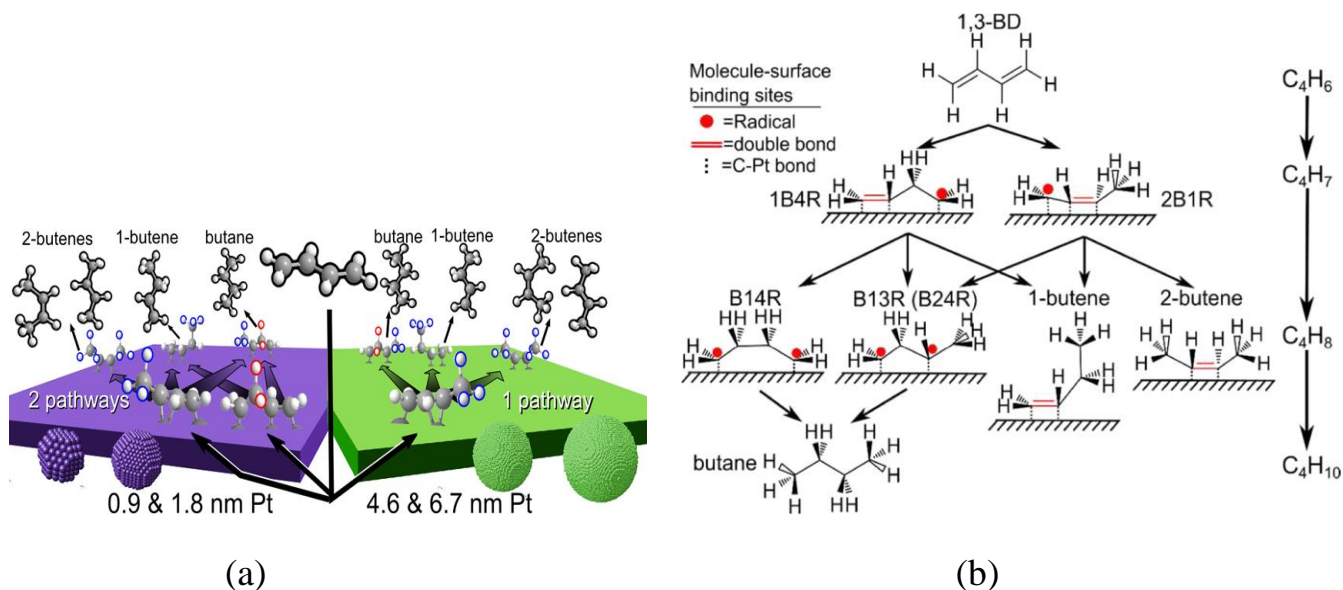
Shi, F., Baker, L. R., Hervier, A., Somorjai, G. A., and Komvopoulos, K., "Tuning the Electronic Structure of Titanium Oxide Support to Enhance the Electrochemical Activity of Platinum Nanoparticles," *Nano Letters* **13**(9) 4469 (2013).

6.2. Novel Catalysts of Nanoparticle Monolayers

Basic understanding of catalysis at the molecular level using nanoparticle monolayer catalysts has been the central objective of several sum frequency generation (SFG) vibrational spectroscopy studies. This work has been largely motivated by the fact that size and shape control of nanoparticle catalysts influences reaction rate and selectivity. Thus, to control the size and shape of catalytic nanoparticles, an organic ligand was used as a capping agent to stabilize the nanoparticles during synthesis. However, the presence of an organic capping agent presents two major challenges in SFG and catalytic reaction studies: (a) it blocks a significant fraction of active surface sites and (b) produces a strong signal, which prevents the detection of reaction intermediates with SFG. Thus, we examined cleaning the Pt nanoparticles capped with poly(vinylpyrrolidone) (PVP) by a solvent or UV cleaning. It was found that solvent cleaning leaves more PVP intact and relies on the disordering by hydrogen gas to reduce the SFG signal of PVP, whereas UV cleaning depends on nearly complete removal of PVP to reduce the SFG signal from PVP. While, both solvent and UV cleaning enable the detection of reaction intermediates by SFG, solvent cleaning also yields nanoparticles that are stable in reaction conditions, while UV cleaning leads to particle agglomeration during reaction. The results of our work indicate that solvent cleaning is more advantageous for studying the effects of nanoparticle size and shape on catalytic selectivity by SFG vibrational spectroscopy.



- (a) Schematic of SFG experiment with Langmuir-Blodgett nanoparticle films deposited on silica prism. Gas mixtures (Ar, H₂/Ar, and C₆H₁₀/H₂/Ar) were flown over the sample while SFG spectra were recorded.
- (b) TEM images (scale bar = 10 nm) showing UV-cleaned and solvent-cleaned Pt-PVP nanoparticles under reaction conditions. For 4.2 and 3.0 nm nanoparticles, 60 min of UV treatment results in clustering, with neighboring nanoparticles moving closer to each other while maintaining their size. Under hydrogenation reaction conditions (200 Torr H₂, 560 Torr Ar, 373 K), clustered nanoparticles often melt together producing much larger particles. Spherical nanoparticles of 1.7 nm size aggregate after 60 min of UV treatment. In contrast, under hydrogenation reaction conditions (200 Torr H₂, 560 Torr Ar) solvent-cleaned Pt-PVP nanoparticles do not show changes up to at least 473 K.
- (c) (A) SFG spectra of 4.2 nm Pt-PVP nanoparticles obtained at 298 K after UV cleaning (0 to 180 min) under cyclohexene hydrogenation reaction conditions of 10 Torr C₆H₁₀, 200 Torr H₂, and 550 Torr Ar. The spectra indicate that the observed intermediates change from exclusively 1,4-CHD (0-3 min) to 1,4-CHD, 1,3-CHD, and π-allyl (30-180 min). (B) XPS results showing the C/Pt ratio as a function of UV exposure time. (C, D) TEM images of UV-cleaned 4.2 nm Pt nanoparticles showing clustering after long treatment (180 min) but no aggregation (scale bar = 10 nm).



- (a) Illustration of product selectivity during 1,3-butadiene hydrogenation on monodisperse, colloiddally synthesized, Pt nanoparticles.
- (b) Schematic of reaction pathways for 1,3-butadiene (1,3-BD) hydrogenation, DFT-predicted stable intermediates during hydrogenation, and observed products. The addition of the first H atom leads to 1-buten-4-yl radical (1B4R) or 2-buten-1-yl radical (2B1R); the addition of a second H atom leads to butan-1,4-diyl radical (B14R), butan-1,3-diyl radical (B13R) or butan-2,4-diyl (B24R) intermediates, or 1-butene (1B) and 2-butene (2B) products. The nomenclature corresponds to IUPAC gas-phase radicals, in which “R” designates a radical. Carbon radicals and double bonds that are highlighted in red designate their locations in the gas phase, which correspond to the locations of C–Pt bonds that are shown by dotted lines.

The decomposition and removal of the PVP capping polymer from the monolayer by cyclic oxidation-reduction treatments and the interaction of CO with as-synthesized, clean Pt nanoparticles were examined in another series of studies. High-pressure adsorption of ethylene on clean Pt nanoparticles experiments revealed that the surface chemistry on clean Pt nanoparticles is similar to that encountered with a single-crystal Pt(100) surface. We also found that the kinetic mechanism of CO oxidation on PtSn catalysts is not limited by O₂ adsorption, as observed on pure Pt catalysts; instead, the PtSn catalyst is highly populated by O at the surface and in subsurface regions of Sn. Ambient-pressure X-ray photoelectron spectroscopy measurements of monodisperse PtSn nanoparticle catalysts showed that Pt and Sn atoms are mobile. The PtSn nanoparticles transform from intermixed Pt and Sn domains to metallic Pt and oxidic Sn domains during CO oxidation. The PtSn catalysts display a reaction mechanism with an activation barrier an order of magnitude less compared to pure Pt catalysts.

More recent studies were devoted to catalytic processes arising on noble metal (e.g., Pt, Pd, and Rh) nanoparticles encapsulated in SiO₂. The advantage with these core-shell catalysts is that the capping agent (e.g., PVP) can be removed by calcination, while still maintaining nanoparticle size monodispersity. This study has provided impetus for further work on core-shell systems aimed at developing fundamental *in situ* techniques for examining reactions on industrial catalysts.

Selected Publications

Krier, J. M., Michalak, W. D., Baker, L. R., An, K., Komvopoulos, K., and Somorjai, G. A., "Sum Frequency Generation Vibrational Spectroscopy of Colloidal Platinum Nanoparticle Catalysts: Disordering versus Removal of Organic Capping," *Journal of Physical Chemistry C* **116**(33) 17540 (2012).

Kweskin, S. J., Rioux, R. M., Song, H., Komvopoulos, K., Yang, P., and Somorjai, G. A., "High-Pressure Adsorption of Ethylene on Cubic Pt Nanoparticles and Pt(100) Single Crystals Probed by *In Situ* Sum Frequency Generation Vibrational Spectroscopy," *ACS Catalysis* **2**(11) 2377 (2012).

Michalak, W. D., Krier, J. M., Komvopoulos, K., and Somorjai, G. A., "Structure Sensitivity in Pt Nanoparticle Catalysts for Hydrogenation of 1,3-Butadiene: *In Situ* Study of Reaction Intermediates Using SFG Vibrational Spectroscopy," *Journal of Physical Chemistry C* **117**(4) 1809 (2013).

Michalak, W. D., Krier, J. M., Alayoglu, S., Shin, J.-Y., An, K., Komvopoulos, K., Liu, Z., and Somorjai, G. A., "CO Oxidation on PtSn Nanoparticle Catalysts Occurs at the Interface of Pt and Sn Oxide Domains Formed Under Reaction Conditions," *Journal of Catalysis* **312** 17 (2014).

Krier, J. M., Michalak, W. D., Cai, X., Carl, L., Komvopoulos, K., Somorjai, G. A., "Sum Frequency Generation Vibrational Spectroscopy of 1,3-Butadiene Hydrogenation on 4 nm Pt@SiO₂, Pd@SiO₂, and Rh@SiO₂ Core-Shell Catalysts," *Nano Letters* **15**(1) 39 (2015).

Krier, J. M., Komvopoulos, K., and Somorjai, G. A., "Cyclohexane and 1,4-Cyclohexadiene Hydrogenation Occur through Mutually Exclusive Intermediate Pathways on Platinum Nanoparticles," *Journal of Physical Chemistry C* **120**(15) 8246 (2016).

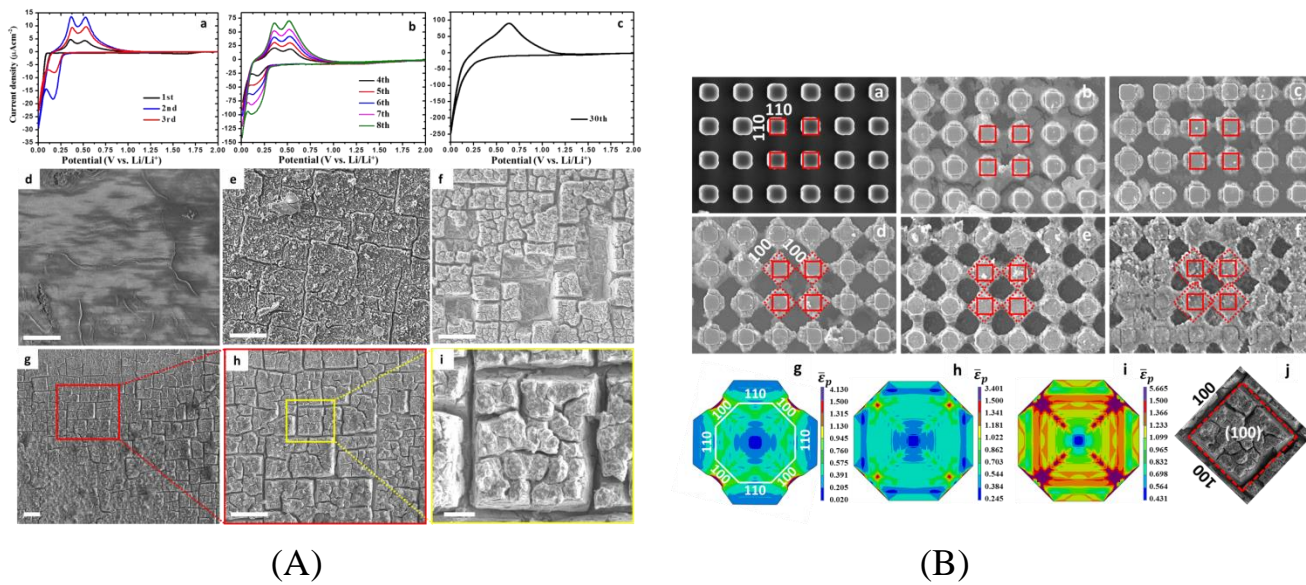
6.3. Li-Ion Battery Electrode Materials

Li-ion batteries (LIBs) have been widely used for long-term energy storage in various applications ranging from portable electronics to hybrid vehicles. However, the chemical instability of the electrolyte during operation has a negative effect on the reliability and durability of LIBs. Passive films, known as solid electrolyte interphase (SEI), forming on electrodes due to electrolyte decomposition produce a profound negative effect on the reversibility of LIBs. However, understanding of the electrolyte decomposition process is inadequate. Therefore, Fourier transform infrared (FTIR) spectroscopy studies were carried out to identify the unstable decomposition products of most common electrolytes of LIBs, such as ethylene carbonate-based electrolytes, which contribute to the formation of SEI. Our findings show that accounting for the solvation effect in FTIR analysis of decomposition electrolyte products contributing to the SEI formation in LIBs is critical. For the first time, our results conclusively identified the dominant role of catalysis in the electrolyte decomposition process. This discovery has important implications in electrode surface modification and electrolyte recipe selection, which are critical factors for enhancing the efficiency, durability, and reliability of LIBs.

For electric vehicles to be widely accepted, it is important to significantly increase the driving distance achieved by a single charge. Thus, in addition to obtaining a better understanding of SEI formation in current LIBs, future batteries must be reconfigured with new electrode materials of higher storage capacity than presently used materials (i.e., graphite). Silicon has been widely recognized as one of the most promising anode materials due to its high energy density; however, large irreversible capacity and poor reliability/durability have dramatically limited its immediate application. These deficiencies are partially due to electrolyte loss by reduction (formation of SEI) and instability of the SEI during charge/discharge. To provide a better understanding on the mechanism of Si electrode failure during battery cycling, we performed extensive electrochemical tests and *in situ* FTIR spectroscopy studies. The ultimate objective of these investigations is to provide fundamental understanding of the underlying

failure mechanisms of Si electrodes, which will enhance the rational design of new battery electrodes exhibiting minimal capacity decay during charge/discharge cycling. By tuning the probing depth in SFG vibrational spectra of molecules at the electrode surface, we specifically studied the dependence of SEI structural components on applied potential and observed that soluble species form on the native silicon oxide film, which might be related to the chemical instability of the SEI, and contribute to the unexpected premature failure of Si electrodes.

We also performed chemical and electrochemical experiments and finite element analysis (FEA) to study the chemical, electrochemical, and mechanical response of single-crystal Si electrodes during multiple charge/discharge cycles. Our study has led to the development of a hybrid experimental-analytical methodology, which can be applied to other ion-host energy storage materials. Our more recent investigations are focused on the concentration dependence of different electrolyte additives on the long-term electrochemical performance of LIBs and dependence of SEI formation mechanism on the concentration of these additives. The understanding of surface reactions occurring on electrode surfaces, knowledge of the role of the SEI film derived from these studies, and ongoing research are expected to provide valuable guidelines for the design of safe, high-capacity batteries exhibiting prolonged lifetime.



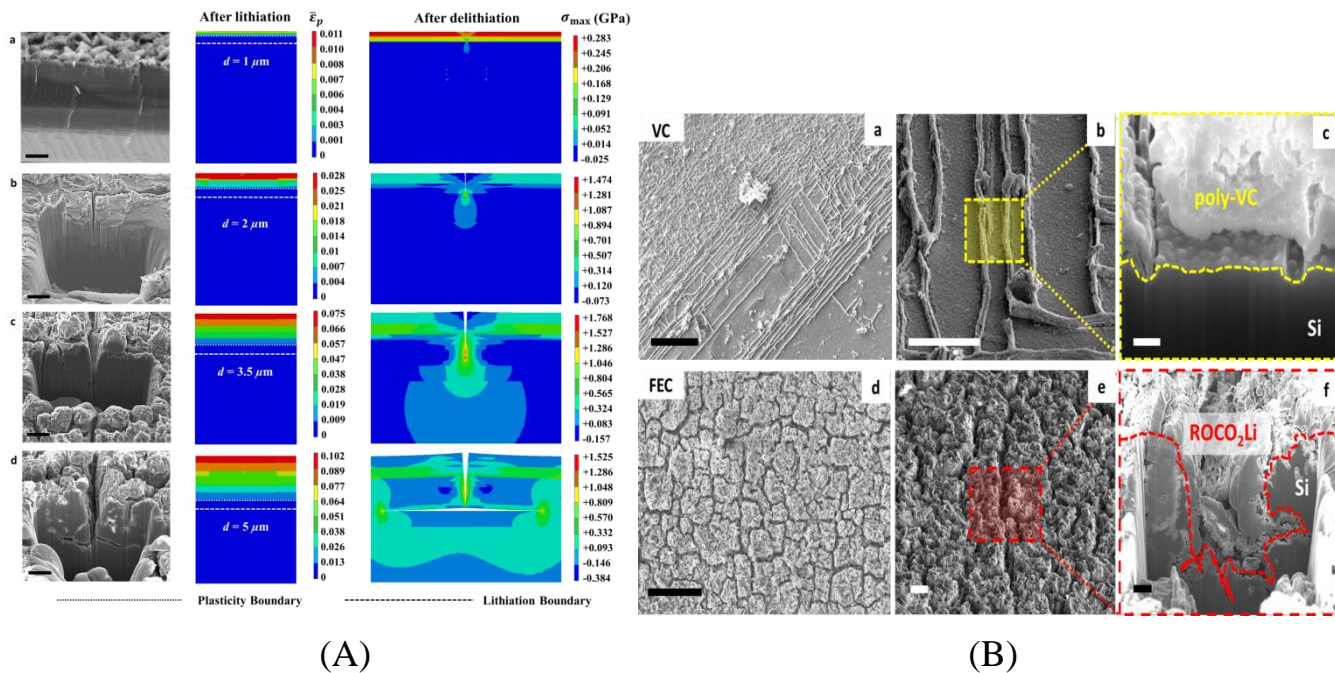
(A) **Electrode cyclic voltammetry response and surface morphology.** Current-voltage curves of a Si(100) electrode cycled between 2.0 and 0.01 V at a scan rate of 0.1 mV/s for (a) 1–3, (b) 4–8 and (c) 30 successive lithiation/delithiation cycles. Top-view SEM images of electrode surface morphology obtained after (d) 3, (e) 8, (f) 50 and (g–i) 30 cycles. (Scale bar: (d–h) 20 μm and (i) 3 μm .)

(B) **Anisotropic in-plane deformation and fracture of lithiated Si(100) micropillars and electrodes.** (a–f) SEM images of square micropillars fabricated on a p-type Si(100) wafer obtained at various lithiation stages (the size of the red solid squares is $3 \times 3 \mu\text{m}^2$). FEA results of in-plane equivalent plastic strain $\bar{\epsilon}_p$ distribution in (g) lithiated (unconstrained) micropillar and (h) lithiated and (i) delithiated (constrained) octahedral “unit cell” of the silicon electrode. (j) SEM image showing a crack pattern on the surface of a lithiated silicon electrode revealing crack formation in the <100> directions.

We have also carried out studies providing a mechanistic explanation of the root cause of premature silicon electrode failure in LIBs after prolonged lithiation/delithiation cycling and identified the fundamental fracture mechanisms of single-crystal silicon electrodes over extended cycling, using

electrochemical testing, microstructure characterization, fracture mechanics and FEA. We discovered that anisotropic lithium invasion results in crack initiation perpendicular to the electrode surface, followed by growth through the electrode thickness. The low fracture energy of the lithiated/unlithiated silicon interface provides a weak microstructural path for crack deflection, accounting for the crack patterns and delamination observed after repeated cycling. On the basis of this insight, we demonstrated how electrolyte additives can change the SEI, tune the mechanical properties of the cohesive layer, and improve the electrode fracture resistance.

The knowledge of the failure mechanisms of silicon electrodes gained from these studies forms a foundation for future design improvements and paves the way toward the development of more robust and durable electrodes for next-generation LIBs.



(A) Experimental and numerical results of electrode fracture. Cross-sectional focused ion beam (FIB)-SEM images (left column) and corresponding FEA results (middle and right columns) of a Si(100) electrode obtained after (a) 3, (b) 8, (c) 30 and (d) 50 lithiation/delithiation cycles. The FIB-SEM images show crack growth through the electrode thickness followed by crack deflection and propagation along the lithiation boundary (lithiated/unlithiated interface). The FEM results show the equivalent plastic strain $\bar{\epsilon}_p$ after lithiation and maximum principal stress σ_{max} after delithiation, illustrating crack initiation, propagation through the electrode thickness and lateral deflection along the lithiation boundary for different lithiation/delithiation cycles. (scale bar: (a) 0.5 μm and (b)-(d) 3 μm)

(B) Electrode crack arrest by reduction products of electrolyte additives. Top-view and cross-sectional SEM images of a Si(100) electrode cycled between 2.0 and 0.01 V for 30 cycles at a scan rate of 0.01 mV/s in EC/DEC/LiPF₆ electrolyte with (a)-(c) 5% VC additive and (d)-(f) 5% FEC additive. The dashed rectangles shown in (b) and (e) indicate the FIB milling area. The reduction products of the VC and FEC additives (poly-VC and ROCO₂Li, respectively) modify the mechanical properties of the solid electrolyte interphase (SEI) film and inhibit crack growth. (scale bar: (a, d) 100 μm , (b, e) 20 μm , (c) 300 nm, and (f) 3 μm)

Selected Publications

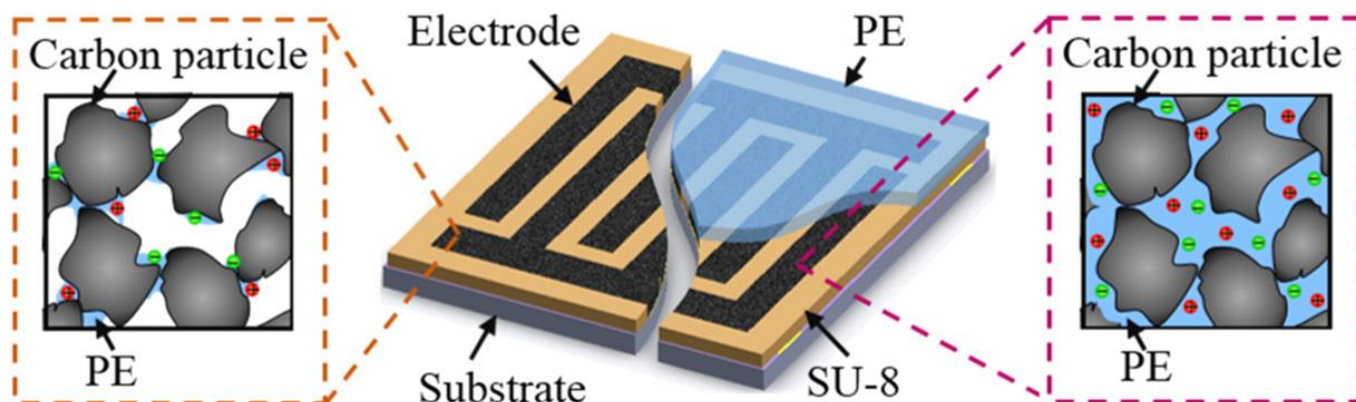
Shi, F., Zhao, H., Liu, G., Ross, Jr., P. N., Somorjai, G. A., and Komvopoulos, K., "Identification of Diethyl 2,5-Dioxahexane Dicarboxylate and Polyethylene Carbonate as Decomposition Products of Ethylene Carbonate Based Electrolytes by Fourier Transform Infrared Spectroscopy," *Journal of Physical Chemistry C* **118**(27) 14732 (2014).

Shi, F., Ross, P. N., Zhao, H., Liu, G., Somorjai, G. A., and Komvopoulos, K., "A Catalytic Path for Electrolyte Reduction in Lithium-Ion Cells Revealed by *in Situ* Attenuated Total Reflection-Fourier Transform Infrared Spectroscopy," *Journal of the American Chemical Society* **137**(9) 3181 (2015).

Shi, F., Song, Z., Ross, P. N., Somorjai, G. A., Ritchie, R. O., and Komvopoulos, K., "Failure Mechanisms of Single-Crystal Silicon Electrodes Subjected to Electrochemical Lithiation/Delithiation in Lithium-Ion Batteries," *Nature Communications* **7** 11886 (2016).

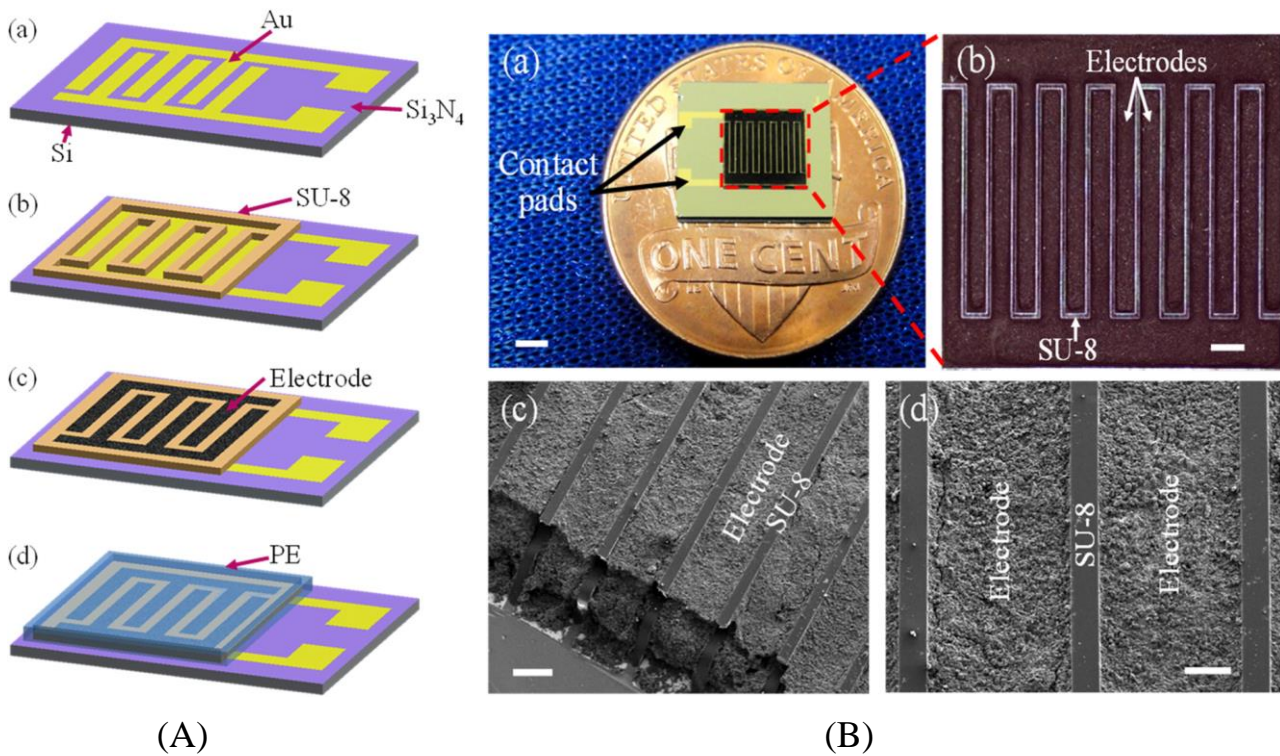
6.4. High-Capacity Energy Storage Systems

Energy storage units are of significant importance to energy conversion devices, such as piezoelectric nanogenerators, solar and thermoelectric cells, and other electronic circuits used to construct self-powered micro/nano-device systems. Microsupercapacitors (MSCs) have attracted significant attention for on-chip energy storage applications because they demonstrate high charge/discharge rate, long operation life, and relatively high energy density. Despite the high capacitance of most MSCs, using a liquid electrolyte in an electrochemical device has several potential risks, such as electrolyte leakage and electrical shortage of electrodes. The interest in MSCs is the development of materials and fabrication approaches that may lead to high-capacity, all-solid-state MSCs exhibiting better safety, environmental friendliness, excellent portability, and higher stability. However, replacing the liquid electrolyte by a solid electrolyte presents several challenges, such as difficulty of the solid electrolyte to diffuse into the bulk of electrodes and restriction in electrode thickness; hence, reduced capacity.

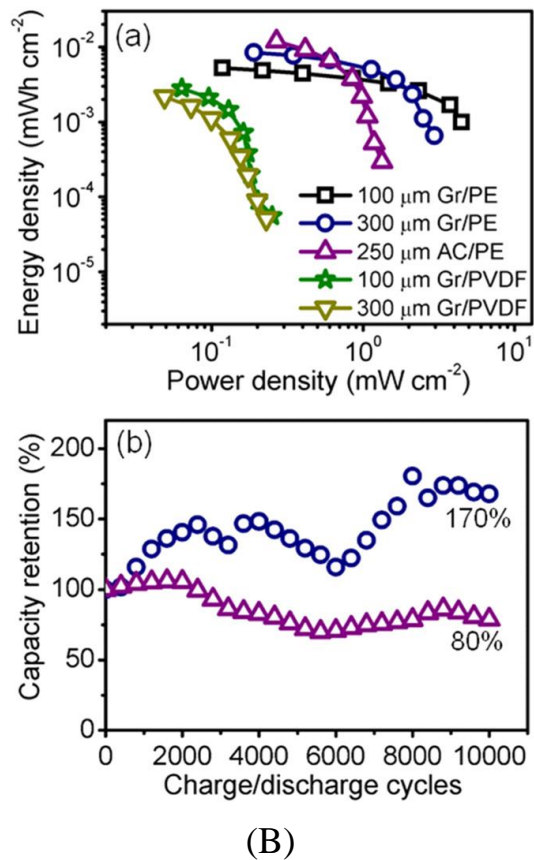
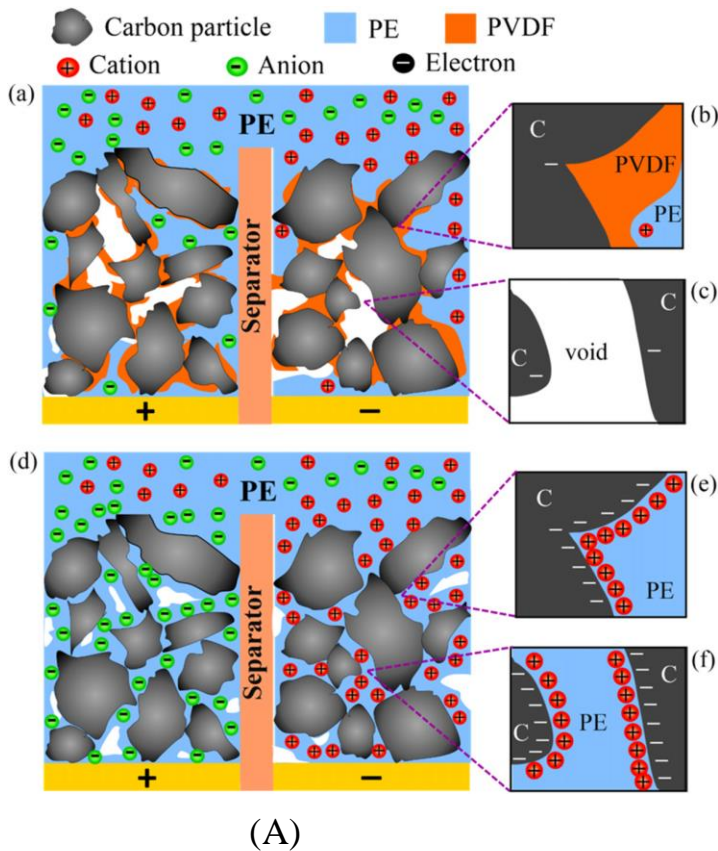


Schematic of a 3D all-solid-state MSC with interdigital electrodes consisting of carbon particle/PE composite. Schematics illustrating the MSC structure before and after coating the electrodes with PE to form electrolyte reservoirs are shown on the left and right, respectively. The incorporation of ion-containing PE in the electrode material before the formation of the electrode (left schematic) promotes the diffusion of PE in the electrode bulk after PE gel coating (right schematic), resulting in the formation of a 3D PE network.

Recent work (in collaboration with Tsinghua University) has brought much excitement because it shows that it is possible to develop high-energy-density, all-solid-state MSCs by using active material-electrolyte composite electrodes. Specifically, we have designed and fabricated 3D MSCs with electrodes consisting of active materials, like graphene or activated carbon particles and polymer electrolyte, which have a capacitance comparable with that of 3D MSCs with liquid electrolyte. While this is ongoing research, these initial findings indicate the high potential of our 3D all-solid-state MSCs for a wide range of power microsystem applications, in particular wearable microelectronics.



(A) Fabrication process of 3D all-solid-state MSCs: (a) deposition of a Si_3N_4 insulation layer on the Si substrate and micropatterning of the Au layer used as a current collector, (b) micropatterning of the SU-8 separators, (c) filling of the SU-8 trenches with electrode material, and (d) electrode coating with polymer electrolyte (PE).
 (B) Digital image of a 3D all-solid-state MSC on a US coin, (b) high-magnification digital image showing the effective area consisting of interdigital Gr/PE electrodes and SU-8 separator, and (c) tilted-view and (d) top-view SEM images of Gr/PE electrodes and SU-8 separator. (The scale bar in (a)-(d) is equal to 2 mm, 500 μm , 200 μm , and 100 μm , respectively.)



(A) Illustrative comparison of 3D all-solid-state MSCs with (a)-(c) carbon/PVDF electrodes and (d)-(f) carbon/PE (PE = PVA-H₃PO₄) electrodes showing that the incorporation of PE in the electrode material is conducive to electric double-layer (EDL) formation around the AC particles.

(B) (a) Ragone plots of 100- and 300- μm -thick Gr/PE, 250- μm -thick AC/PE, and 100- and 300- μm -thick Gr/PVDF MSCs for a scan rate in the range of 5-1000 mV/s and (b) capacity retention cycling of 300- μm -thick Gr/PE and 250- μm -thick AC/PE MSCs vs charge/discharge cycles for a scan rate of 50 mV/s.

Selected Publications

Pu, J., Wang, X., Liu, J., Li, S., and Komvopoulos, K., "A 3D All-Solid-State Microsupercapacitor with Electrodes Consisting of Activated Carbon/Polymer Electrolyte Composite," *Transducers 2015, 18th International Conference on Solid-State Sensors, Actuators and Microsystems*, Anchorage, AK, 2015, pp. 502-505.

Pu, J., Wang, X., Zhang, T., Li, S., Liu, J., and Komvopoulos, K., "High-Energy-Density, All-Solid-State Microsupercapacitors with Three-Dimensional Interdigital Electrodes of Carbon/Polymer Electrolyte Composite," *Nanotechnology* **27**(4) 045701 (2016).

Computational Surface Mechanics Laboratory (CSML)

Research in CSML encompasses analytical and numerical studies of surface interactions occurring over a wide range of length scales and dynamic analysis of mechanical components. Most of the studies in CSML are complementary to those conducted in SSEL, aiming to provide additional insight into experimentally observed deformation behaviors and physicochemical surface phenomena.

Recent studies in CSML have been mainly focused onto microscale plasticity and fracture of layered media due to contact interaction with rough surfaces. These comprehensive investigations on contact mechanics of fractal surfaces are the first to demonstrate scale dependencies in contact deformation phenomena and provide impetus for further studies in this emerging subfield of contact mechanics. In particular, dynamic contact of rough (fractal) elastic-plastic surfaces is new to the field of contact mechanics and of great importance to various microdevices having dynamic contact interfaces.

The novelty of the above studies is the implementation of real surfaces, realistic elastic-plastic constitutive models, and dynamic (impact) contact conditions in analytical and numerical (finite element method) models to predict the dynamic response of deformed homogeneous and layered media.

Recent research in CSML encompasses the following main topics:

- **DISCRETE DISLOCATION PLASTICITY ANALYSIS OF CONTACTING SURFACES**
- **SLIP-LINE PLASTICITY ANALYSIS OF INTERACTING ROUGH SURFACES**
- **ELASTIC-PLASTIC SPHERICAL INDENTATION**
- **MECHANICS OF ADHESIVE CONTACTS**
- **ADHESION-INDUCED CONTACT INSTABILITIES BETWEEN ROUGH ELASTIC-PLASTIC SURFACES**
- **MECHANICS OF THIN FILM DELAMINATION IN ADHESIVE CONTACTS**
- **MECHANICS OF NANOSCALE POLISHING, ADHESIVE WEAR, AND ASPERITY MICROFRACTURE**
- **MECHANICS OF OSCILLATORY ELASTIC-PLASTIC CONTACTS**
- **MECHANICS OF FLEXIBLE AND STRETCHABLE ELECTRONICS**

Main Software and Computer Facilities

To respond to the demands for in-depth stress/strain analysis, accurate life prediction, and challenging problems in contact mechanics, SCML is equipped with the following commercial computational FEA, solid modeling codes, custom-made software, and several state-of-art computers.

- Standard solid work software packages Auto-CAD and ProE enable the analysis of very complex geometries, such as those of rough (fractal) surfaces and modal shapes of dynamic components.
- The preferred FEM code for complex modeling at macro-, meso-, and micro-scale is the multi-physics code ABAQUS. This code not only provides both implicit and explicit algorithms, but also the capability to tackle problems involving large deformations, large strain gradients, and geometric/material nonlinearities.
- PATRAN (MSC Software product) is extensively used for pre-/post-processing work.
- For contact mechanics analysis below the threshold of continuum description, custom-made molecular dynamics (MD) codes are used to model inter-/intra-atomic interactions and deformation at the atomic scale as well as phase transitions due to thermal and mechanical effects.

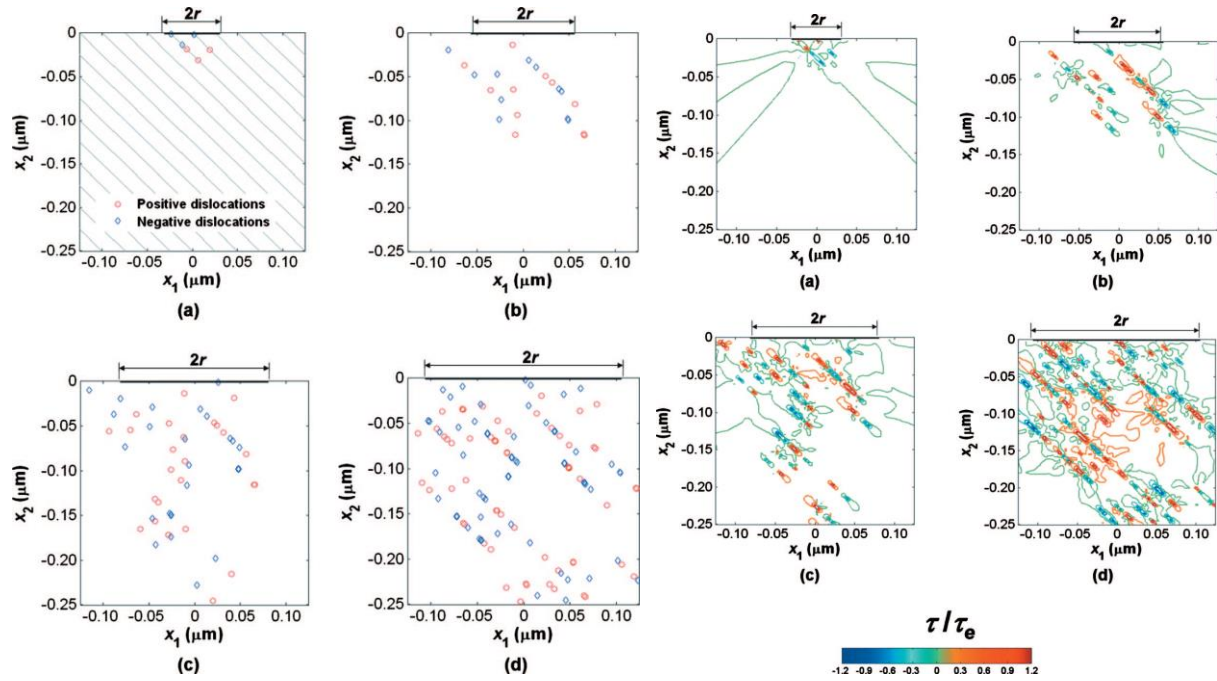
Computational work in CSML is carried out with the following computer workstations:

- Eight Dell Precision PWS-690 workstations (Intel® Xeon® CPU E5345 @ 2.33 GHz; 4 GB RAM; ACPI multiprocessor x64-based PC; File system: NTFS 250GB; DVD/CD-ROM drives: HL-DT-ST DVD+-RW GSA-H21N; Video card: NVIDIA Quadro FX 3450/4000 SDI; 3.5 inch floppy disk-drive; 19" LCD monitor: Dell 1908FPb). The quad-core 4 CPU processor and 4 GB RAM of each workstation allows parallel processing of the ABAQUS solver in cases of large computational FEA models
- Two 1 TB Maxtor shared storage connected to a 24-port 10/100/1000 GB Switch (Model No. SRW2024P with Webview and ProE). This switch enables fast file sharing and system backing up operations among the network of the workstations and allows for much higher speed of data transfer with an outside network. To further utilize this switch, a number computational server will be added to the existing network.

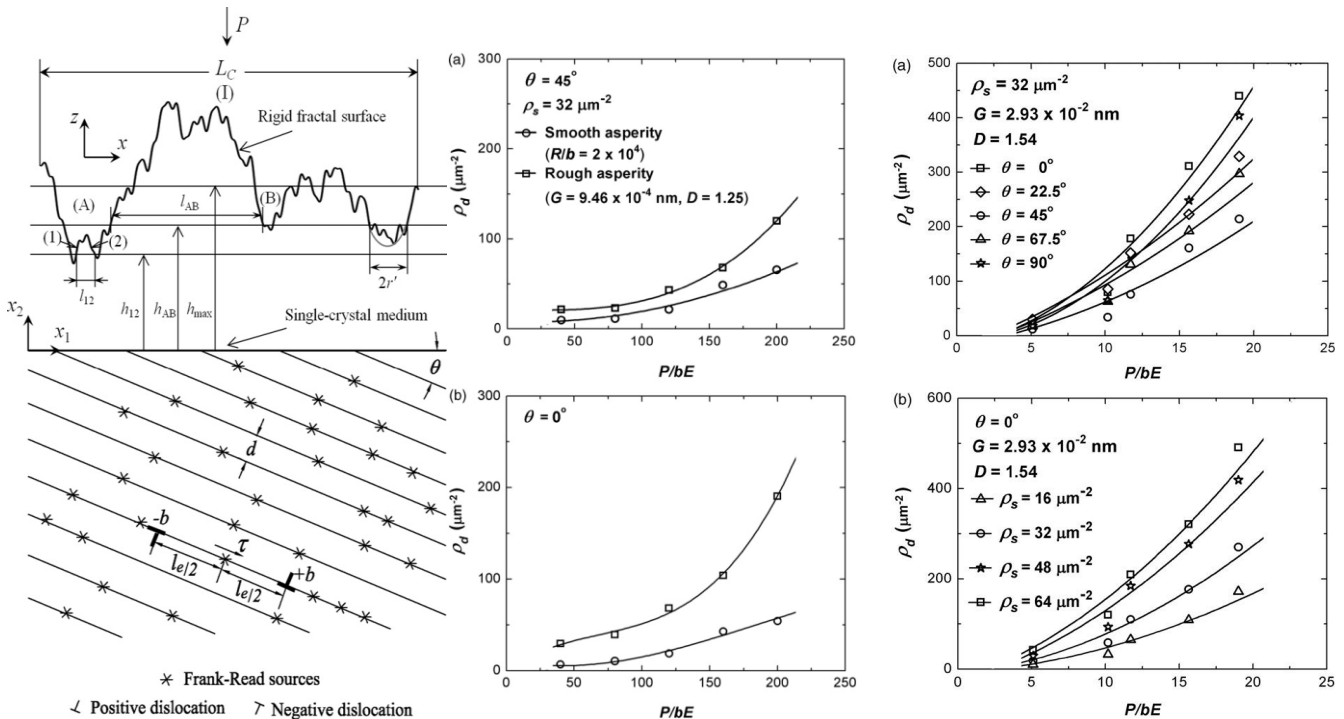
Summaries of Research Projects

The following investigations represent recent progress in pioneering work on surface mechanics of rough surfaces demonstrating multi-scale random roughness and the development of powerful computational capabilities for solving complex contact problems. These are the first surface mechanics studies to conclusively reveal scale dependencies of various contact phenomena. In particular, dynamic contact (impact) of elastic-plastic surfaces exhibiting multi-scale roughness and multi-layered structures represent pioneering initiatives at CSML. The novelty of these studies is the implementation of real surfaces, the development of realistic elastic-plastic constitutive contact models, the incorporation of interfacial adhesion, and the simulation of dynamic contact conditions that elucidate the interdependence of surface topography, adhesion, deformation, damage, and material removal (wear) at various length scales.

Investigations of elastic-plastic deformation in homogeneous and layered media have been carried out using discrete dislocation plasticity, slip-line plasticity theory, and finite element modeling. Our most recent studies include indentation, adhesive contact loading and unloading, surface microfracture, and oscillatory sliding (fretting) contact. These mechanics studies have been motivated by increasing needs



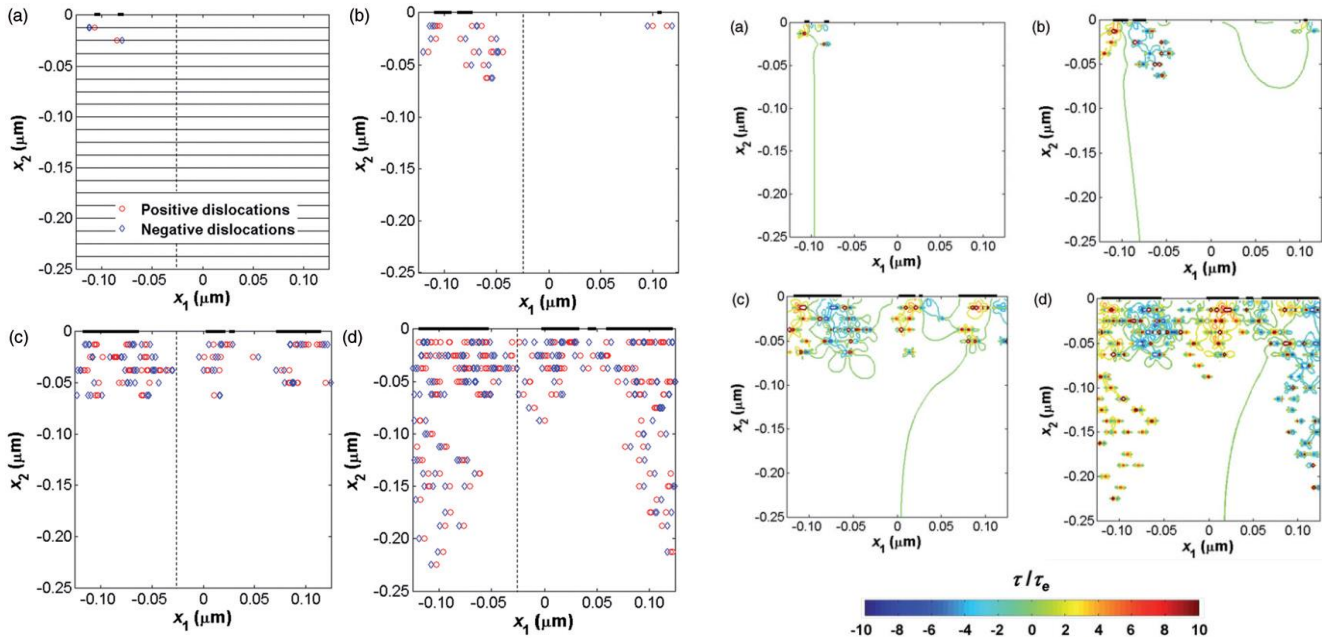
Left: (a)-(d) Dislocation maps vs contact width $2r$ (or normal load) for slip-plane orientation angle $\theta = 45^\circ$. Positive and negative dislocations are shown in red and blue, respectively.
Right: (a)-(d) Contours of dimensionless total resolved shear stress for different contact widths $2r$ corresponding to the dislocation maps shown on the left.



Left: Schematic of a single-crystal semi-infinite medium containing Frank-Read dislocation sources randomly distributed on parallel and equally spaced slip-planes indented by a rigid, rough (fractal) surface.

Middle: Dislocation density ρ_d vs dimensionless contact load P/bE for a single-crystal semi-infinite medium with dislocation source density $\rho_s = 32 \mu\text{m}^{-2}$ and slip-plane orientation angle θ equal to (a) 45° and (b) 0° indented by a rigid, smooth asperity of dimensionless radius of curvature $R/b = 2 \times 10^4$ and a rigid, rough (fractal) asperity with fractal parameters $G = 9.46 \times 10^{-4} \text{ nm}$ and $D = 1.25$.

Right: (a) Dislocation density ρ_d vs dimensionless contact load P/bE and slip-plane orientation angle θ for a single-crystal semi-infinite medium with dislocation source density $\rho_s = 32 \mu\text{m}^{-2}$ indented by a rigid, rough (fractal) surface with fractal parameters $G = 2.93 \times 10^{-2} \text{ nm}$ and $D = 1.54$. (b) Dislocation density ρ_d vs dimensionless contact load P/bE and dislocation source density ρ_s for a single-crystal semi-infinite medium with slip-plane orientation angle $\theta 0^\circ$ indented by the same surface as in (a).



Left: Evolution of dislocation structures in the subsurface of a single-crystal semi-infinite medium with slip-plane orientation angle $\theta 0^\circ$ for dimensionless global interference h/d equal to (a) 0.1, (b) 0.26, (c) 0.58, and (d) 0.9. Positive and negative dislocations are shown by red and blue symbols, respectively. Slip-planes are only shown in (a) for clarity.

Right: Contours of dimensionless total resolved shear stress for h/d equal to (a) 0.1, (b) 0.26, (c) 0.58, and (d) 0.9, corresponding to the dislocation structures shown on the left. Contact widths between the asperities of the rough surface and the semi-infinite medium are denoted by thick lines at the medium's surface.

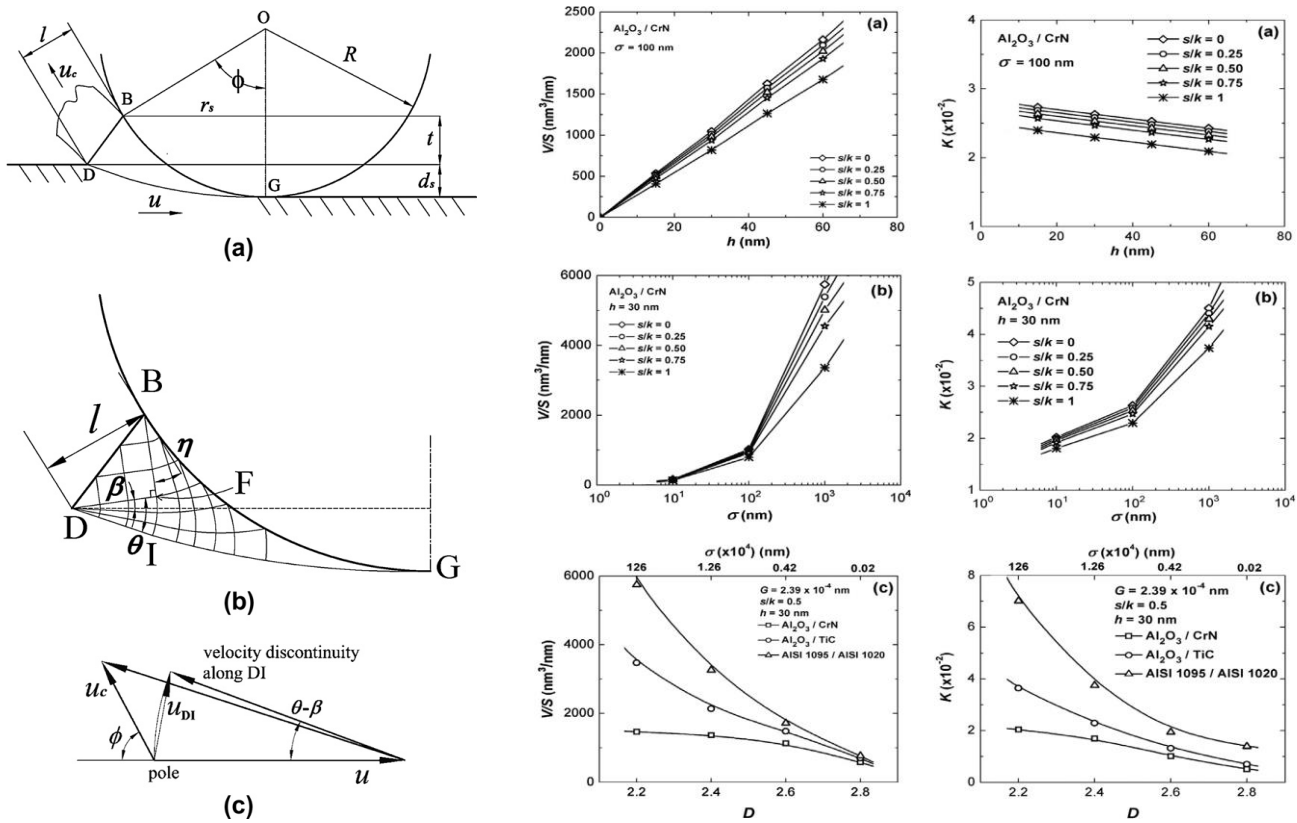
Selected Publications

Yin, X., and Komvopoulos, K., "A Discrete Dislocation Plasticity Analysis of a Single-Crystal Half-Space Indented by a Rigid Cylinder," *ASME Journal of Applied Mechanics* **78**(4) 041019 (2011).

Yin, X., and Komvopoulos, K., "A Discrete Dislocation Plasticity Analysis of a Single-Crystal Semi-infinite Medium Indented by a Rigid Surface Exhibiting Multi-Scale Roughness," *Philosophical Magazine* **92**(24) 2984 (2012).

2. SLIP-LINE PLASTICITY ANALYSIS OF INTERACTING ROUGH SURFACES

Surface interaction plays a critical role in mechanical components with contact interfaces (e.g., gears and bearings) and surfacing techniques (e.g., chemo-mechanical polishing and lapping). The main goal in this work is to develop comprehensive analytical models of sliding friction and mechanical wear for contact interfaces demonstrating multi-scale roughness. Instead of relying on empirical approaches based on experimental measurements, friction and wear models are developed for sliding contact of rough (fractal) surfaces. In particular, we have obtained numerical results of representative ceramic/ceramic, ceramic/metallic, and metal/metal sliding systems, which provide insight into the effects of the normal load, fractal parameters (surface roughness) of the harder surface, interfacial shear strength (adhesion), and material properties on the evolution of microscale plasticity (asperity scale), global coefficient of friction, and frictional energy dissipated during sliding.



Left: (a) Schematic of a hard spherical asperity (or wear particle) plowing through a soft surface and removing material by a microcutting process, (b) detailed view of plastic region consisting of a network of orthogonal α and β slip-lines, and (c) hodograph of the slip-line field.

Middle: (a) Wear rate V/S of $\text{Al}_2\text{O}_3/\text{CrN}$ sliding system vs global surface interference h and dimensionless interfacial shear strength s/k for fractal roughness parameters $D = 2.24$ and $G = 1.07 \times 10^{-4}$ nm, and rms roughness $\sigma = 100$ nm; (b) wear rate V/S of $\text{Al}_2\text{O}_3/\text{CrN}$ sliding system vs rms roughness σ of hard surface and dimensionless interfacial shear strength s/k for $D = 2.24$ and $h = 30$ nm; (c) wear rate V/S of different sliding systems vs fractal dimension D and rms roughness σ of hard surface for $G = 2.39 \times 10^{-4}$ nm, $h = 30$ nm, and $s/k = 0.5$.

Right: Wear coefficient K of sliding systems shown in the middle panel.

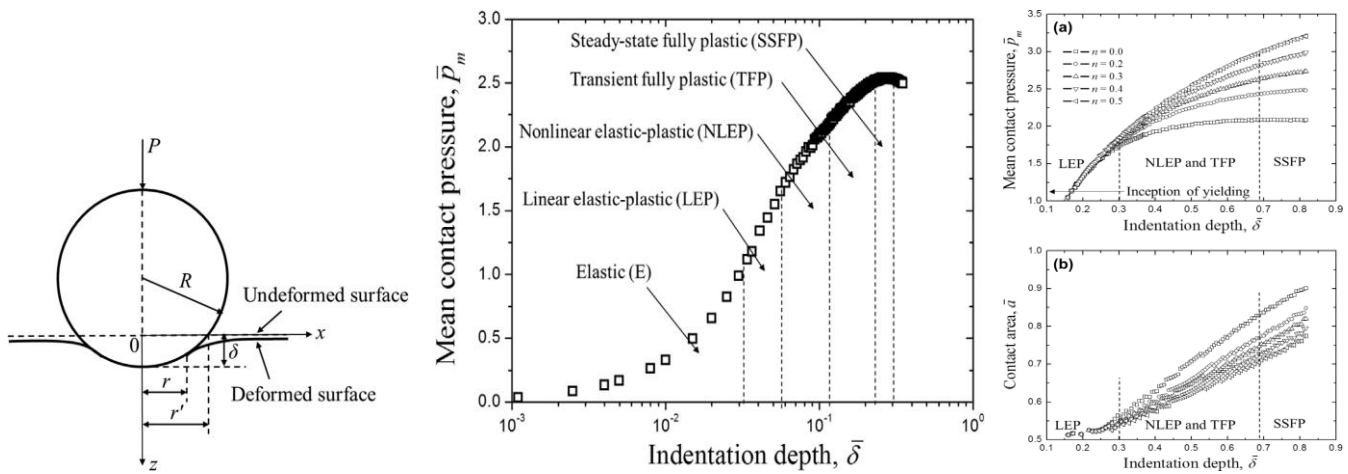
Selected Publications

Yin, X., and Komvopoulos, K., "A Slip-Line Plasticity Analysis of Abrasive Wear of a Smooth and Soft Surface Sliding Against a Rough (Fractal) and Hard Surface," *International Journal of Solids and Structures* **49**(1) 121 (2012).

Yin, X., and Komvopoulos, K., "A Slip-Line Plasticity Analysis of Sliding Friction of Rough Surfaces Exhibiting Self-Affine (Fractal) Behavior," *Journal of the Mechanics and Physics of Solids* **60**(3) 538 (2012).

3. ELASTIC-PLASTIC SPHERICAL INDENTATION

Indentation-induced plasticity is a fundamental problem in contact mechanics with direct implications in various engineering applications, including hardness measurement, load bearing longevity, and effective operation of contact-mode devices spanning a wide range of length scales (e.g., hard-disk drives and gas turbines). However, knowledge of the deformation modes affecting the post-yield behavior, the accurate measurement of the true material hardness, and the effect of strain hardening on the indentation response is mostly empirical. Understanding deformation due to indentation loading/unloading requires knowledge of the evolution of plasticity in terms of global deformation parameters. The objective of our studies is to examine the post-yield indentation behavior of elastic-plastic half-spaces for a wide range of material properties and identify the deformation regimes encountered from the inception of yielding to the establishment of steady-state fully plastic deformation. We have introduced a general description of elastic-plastic deformation of indented materials possessing different strain hardening characteristics in terms of the effective strain, which accounts for the variation of the yield strength with strain hardening, and have developed generalized constitutive equations of the mean contact pressure and contact area for perfectly plastic and strain hardening materials.



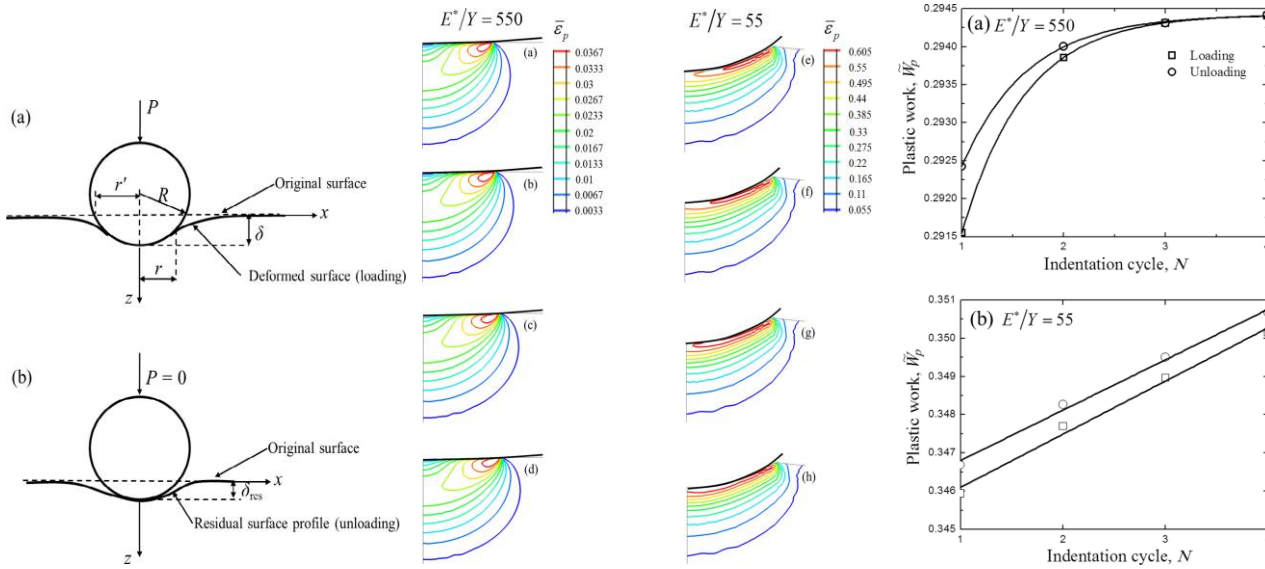
Left: Schematic of a deformable half-space indented by a rigid sphere.

Middle: Mean contact pressure vs indentation depth for an elastic-perfectly plastic half-space with elastic modulus-to-yield strength ratio $E/Y = 55$.

Right: (a) Mean contact pressure and (b) contact area vs indentation depth for an elastic-plastic half-space with $E/Y = 11$ and strain hardening exponent n between 0 and 0.5.

Another main objective of our work is to derive constitutive equations of the unloading response in spherical indentation accounting for material strain hardening, for which fundamental knowledge is

lacking, and to examine the accumulation of plasticity due to repeated spherical indentation. The novelty of this study is twofold. First, it is the first to provide constitutive equations of the unloading response in spherical indentation of strain hardening materials. Second, it elucidates the accumulation of plasticity in cyclic spherical indentation by tracking the development of the plastic zone and the dissipation of plastic work in each indentation cycle.



Left: Schematic illustration of spherical indentation of a half-space: (a) loading and (b) full unloading.
Middle: Contours of equivalent plastic strain in elastic–perfectly plastic materials with elastic modulus-to-yield strength ratio equal to 550 (left column) and 55 (right column) obtained after four consecutive indentation cycles of fixed maximum load: (a, e) first loading, (b, f) first unloading, (c, g) second loading, and (d, h) second unloading.
Right: Plastic work due to indentation loading under a fixed maximum load obtained after full unloading of elastic-perfectly plastic materials with (a) elastic modulus-to-yield strength ratio equal to (a) 550 and (b) 55 vs indentation cycle.

Selected Publications

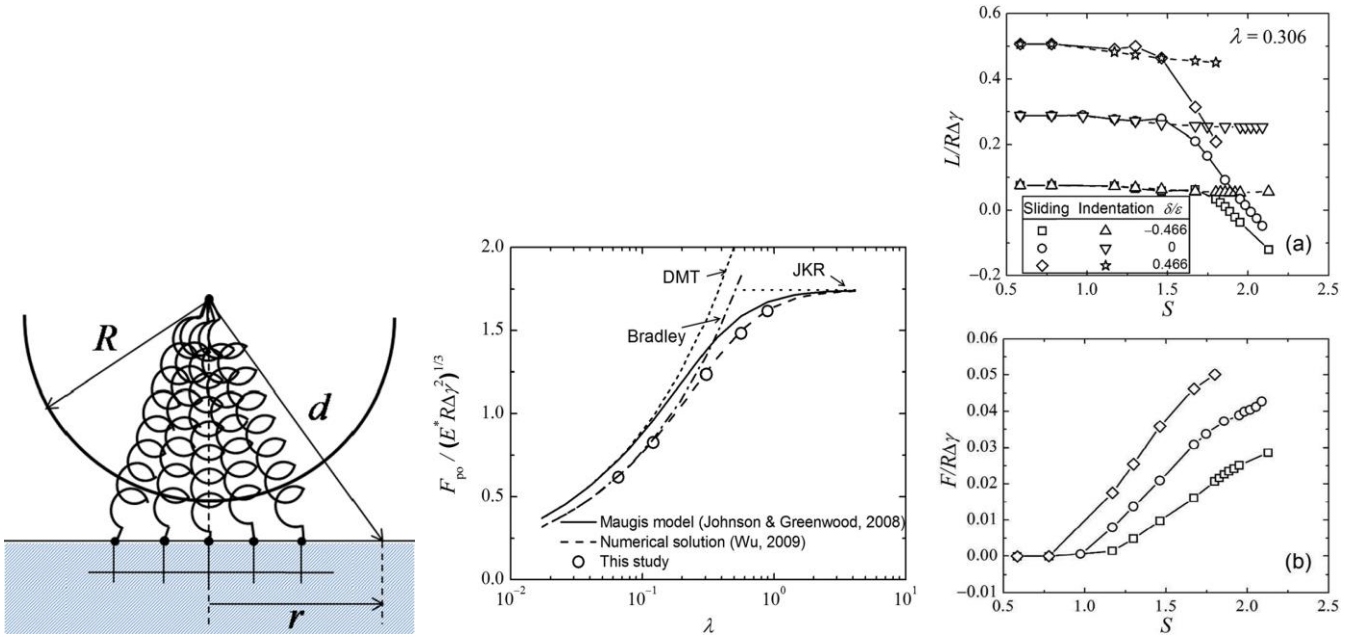
Song, Z., and Komvopoulos, K., “Elastic-Plastic Spherical Indentation: Deformation Regimes, Evolution of Plasticity, and Hardening Effect,” *Mechanics of Materials* **61** 91 (2013).

Song, Z., and Komvopoulos, K., “An Elastic–Plastic Analysis of Spherical Indentation: Constitutive Equations for Single-Indentation Unloading and Development of Plasticity Due to Repeated Indentation,” *Mechanics of Materials* **76** 93 (2014).

4. MECHANICS OF ADHESIVE CONTACTS

Adhesion is an important phenomenon affecting the performance and reliability of various mechanical components with contact interfaces, especially at submicron scales where surface forces dominate the bulk forces. Adhesion intensifies surface interaction, leading to energy loss, surface damage, material loss (wear) and, ultimately, the cessation of device operation. A series of analytical and numerical investigations were performed having as the main objective to elucidate adhesion effects in elastic-plastic contact behavior of homogeneous and layered media. The effect of adhesion on elastic-plastic

deformation of sliding contacts was modeled with nonlinear springs obeying a constitutive law derived from the Lennard-Jones potential. This is one of the primitive investigations to incorporate molecular dynamics description of adhesion in a continuous mechanics model. Displacement-control sliding simulations yielded solutions of the maximum adhesion force, normal and friction force, and subsurface stresses and strains, which provide insight into the effects of the work of adhesion, interaction distance, and elastic-plastic material properties on sliding contact behavior.

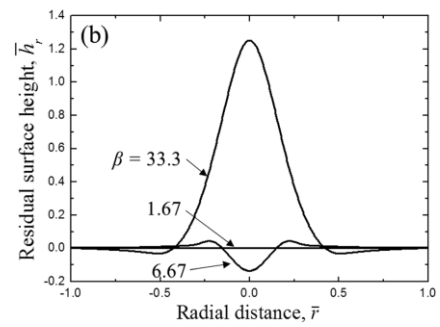
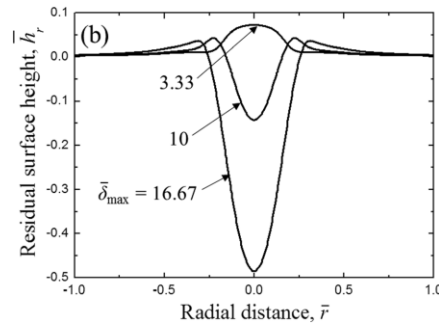
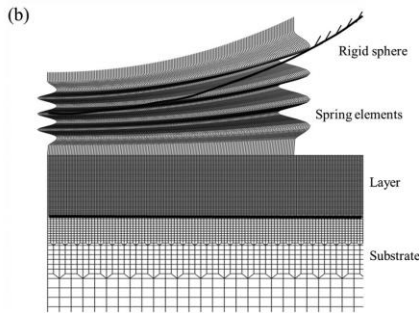
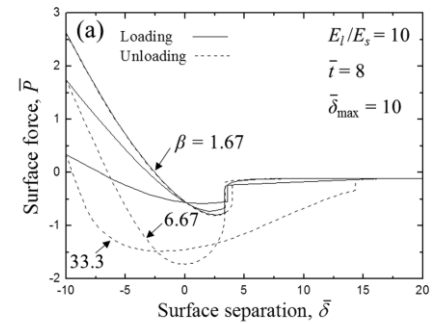
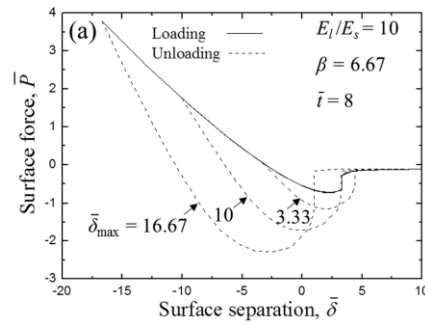
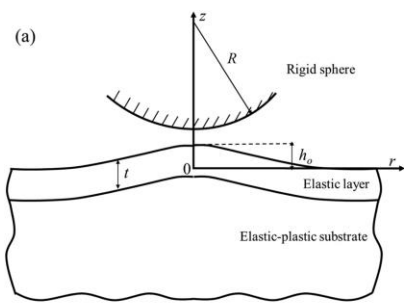


Left: Cross-sectional schematic of a cylindrical asperity in close proximity with a half-space. Adhesion forces are modeled by nonlinear springs attached to the asperity center and surface nodes of the half-space.

Middle: Solutions of the pull-off force vs Maugis parameter λ obtained from 2D adhesion models of elastic line contact: (- · - · - ·) Bradley model, (- - -) DMT model, (· · · · ·) JKR model, (—) Maugis model, (- - -) numerical solution of Wu, and (O) this study (Xu & Komvopoulos model).

Right: (a) Normal force for steady-state sliding and indentation and (b) friction force vs plasticity parameter $S = \Delta\gamma/\varepsilon Y$ for $\delta/\varepsilon = -0.466, 0,$ and 0.466 and $\lambda = 0.306$. (γ = work of adhesion, δ = interaction distance, ε = intermolecular equilibrium distance, and Y = yield strength)

The previous study was recently extended to investigate the interfacial strength of adhesion and contact instabilities due to adhesion between rough surfaces. One of our most important findings is that the classical adhesion parameter, used in the literature for many years, governs the strength of adhesion only of compliant rough surfaces. Thus, a new adhesion parameter was introduced for relatively stiff contact systems, and the applicable ranges of both the classical and new adhesion parameters were determined for different characteristic length scales at the single-asperity and rough-surface levels. The effects of surface adhesion and strain hardening on elastic-plastic contact deformation due to repetitive sliding (fatigue) were also examined and deformation maps providing information about the steady-state mode of deformation were obtained for materials exhibiting elastic-perfectly plastic (EPP) and elastic-linear kinematic hardening plastic (ELKP) behavior.

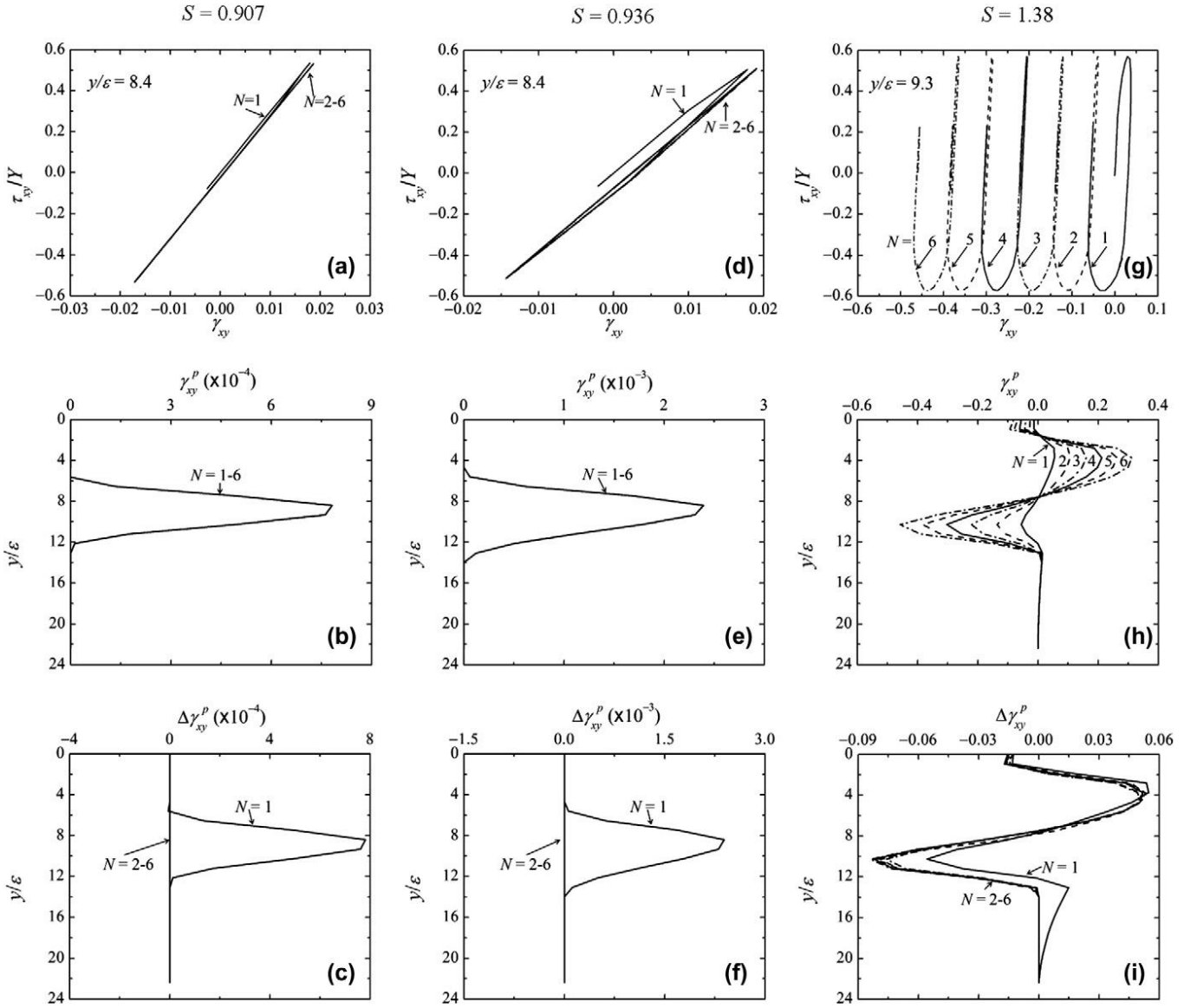


Left: (a) Schematic of a rigid sphere in close proximity with a layered medium consisting of an elastic layer and an elastic-plastic substrate (the upward deflection of the layered medium is due to the adhesion (attractive) surface force) and (b) finite element mesh of the layered medium, showing the nonlinear spring elements used to model interfacial adhesion.

Middle: (a) Surface force vs surface separation during loading (solid lines) and unloading (dashed lines) and (b) residual surface height vs radial distance for elastic-plastic layered medium, $E_l/E_s = 10$, $\beta = 6.67$, $t/\varepsilon = 8$, and $\delta_{\max}/\varepsilon = 53.33, 10$, and 16.7

Right: (a) Surface force vs surface separation during loading (solid lines) and unloading (dashed lines) and (b) residual surface height vs radial distance for elastic-plastic layered medium, $E_l/E_s = 10$, $\beta = 1.67, 6.67$, and 33.3 , $t/\varepsilon = 8$, and $\delta_{\max}/\varepsilon = 10$.

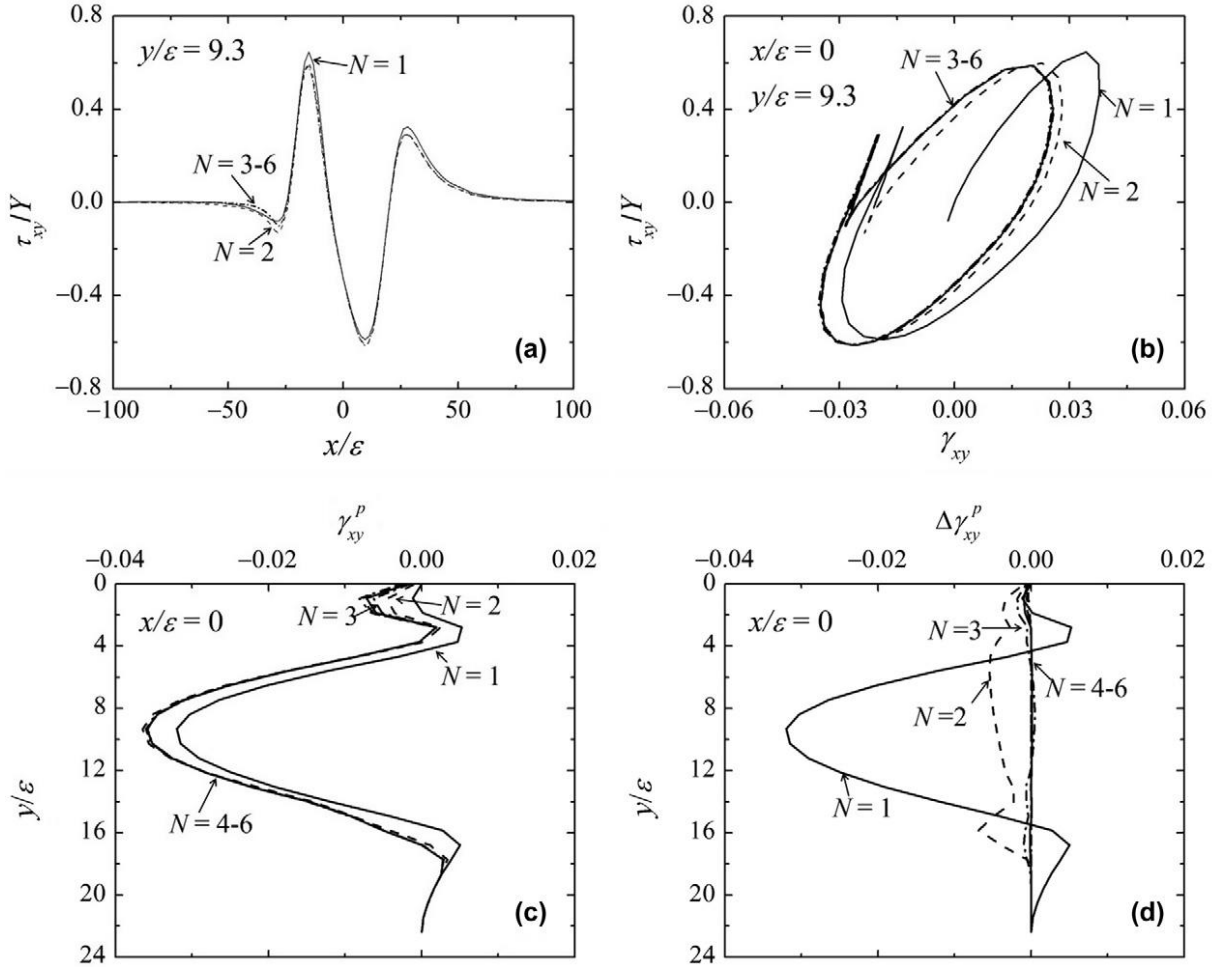
EPP
 $\lambda = 0.306, \delta/\varepsilon = 0, x/\varepsilon = 0$



Effect of plasticity parameter $S = \Delta\gamma/\varepsilon Y$ on deformation behavior for sliding cycle $N = 1-6$, $\lambda = 0.306$, $\delta/\varepsilon = 0$, $x/\varepsilon = 0$, and EPP material behavior: (a, d, g) shear stress τ_{xy}/Y vs shear strain γ_{xy} at the location of the maximum plastic strain; (b, e, h) depth distributions of residual plastic shear strain γ_{xy}^p ; (c, f, i) depth distributions of residual plastic shear strain increment $\Delta\gamma_{xy}^p$.

ELKP

$$\lambda = 0.306, S = 1.38, E_p/E = 0.1, \delta/\varepsilon = 0$$



(a) Shear stress τ_{xy}/Y vs sliding distance x/ε ; **(b)** shear stress τ_{xy}/Y vs shear strain γ_{xy} at $x/\varepsilon = 0$, both at the depth of maximum plastic strain $y/\varepsilon = 9.3$; **(c)** depth distributions of residual plastic shear strain γ_{xy}^p at $x/\varepsilon = 0$; **(d)** depth distributions of residual plastic shear strain increment $\Delta\gamma_{xy}^p$ at $x/\varepsilon = 0$ for sliding cycle $N = 1-6$, $\lambda = 0.306$, $S = \Delta\gamma/\varepsilon Y = 1.38$, $E_p/E = 0.1$, $\delta/\varepsilon = 0$, and ELKP material behavior.

Selected Publications

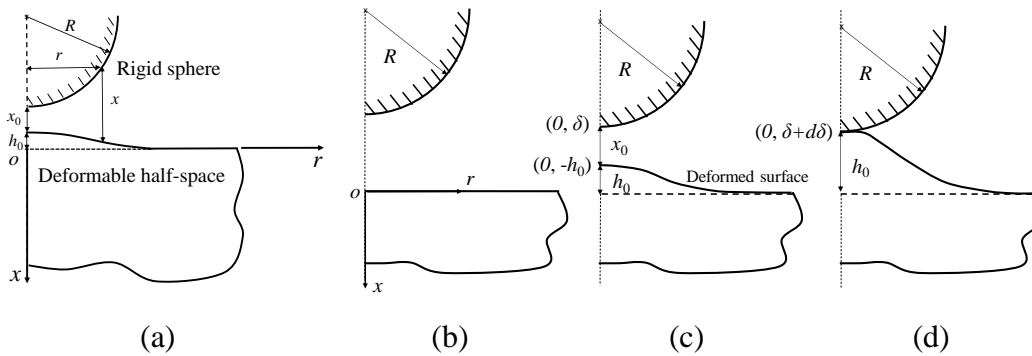
Xu, H., and Komvopoulos, K., "Elastic-Plastic Analysis of Adhesive Sliding Contacts," *ASME Journal of Applied Mechanics* **80**(4) 041010 (2013).

Song, Z., and Komvopoulos, K., "Adhesive Contact of Elastic-Plastic Layered Media: Effective Tabor Parameter and Mode of Surface Separation," *ASME Journal of Applied Mechanics* **80**(2) 021022 (2013).

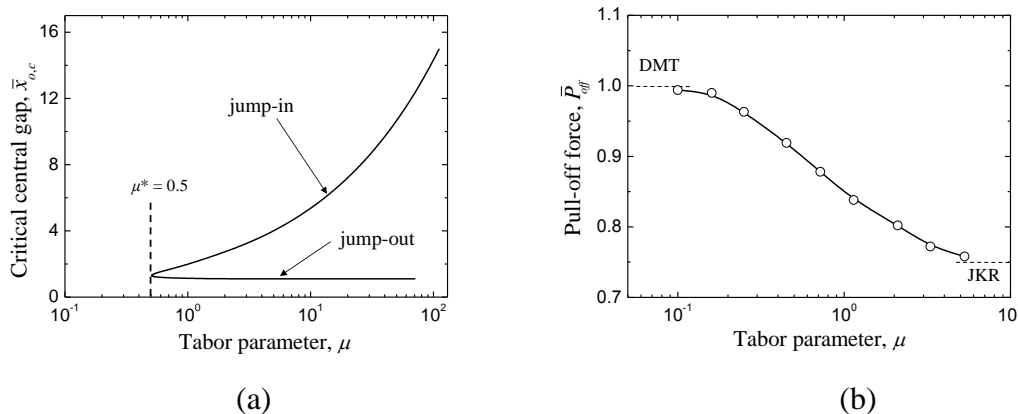
Xu, H., and Komvopoulos, K., "Surface Adhesion and Hardening Effects on Elastic-Plastic Deformation, Shakedown and Ratcheting Behavior of Half-Spaces Subjected to Repeated Sliding Contact," *International Journal of Solids and Structures* **50**(6) 876 (2013).

5. ADHESION-INDUCED CONTACT INSTABILITIES BETWEEN ROUGH ELASTIC-PLASTIC SURFACES

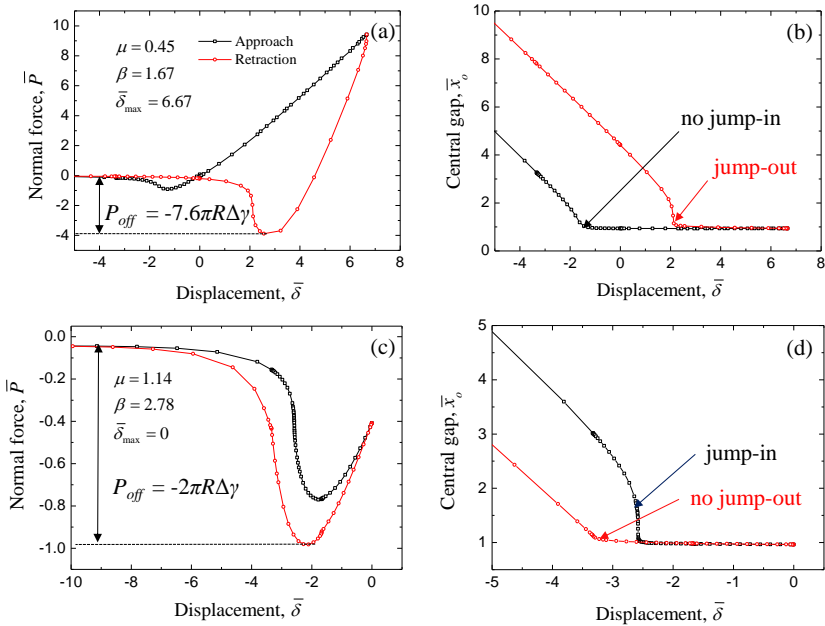
Surface adhesion is of great importance in many engineering systems where surface forces exceed bulk forces, such as microelectromechanical systems, hard-disk drives, and surface force microscopes. Our objective is to examine adhesion-induced contact instabilities in elastic and elastic-plastic contacts of systems exhibiting finite stiffness. To accomplish this objective, adhesive interaction in spherical contacts was modeled with the Lennard-Jones (L-J) potential and elastic adhesive contact was analyzed with the equivalent system of a rigid sphere with reduced radius of curvature and a half-space of effective elastic modulus. The critical gap at the instant of abrupt surface contact (jump-in) and separation (jump-out) was determined from the deformed surface profile of the elastic half-space and geometrical relationships. A finite element model of a rigid sphere and an elastic-plastic half-space was used to examine elastic-plastic adhesive contact. Surface adhesion was modeled by nonlinear springs with a force-displacement relationship governed by the L-J potential. The evolution of the interfacial force and the occurrence of jump-in and jump-out instabilities were investigated in terms of Tabor parameter, plasticity parameter, and dimensionless maximum normal displacement. The force-displacement response due to several approach-retraction cycles was interpreted in the context of elastic and plastic shakedown behaviors using dimensionless parameters.



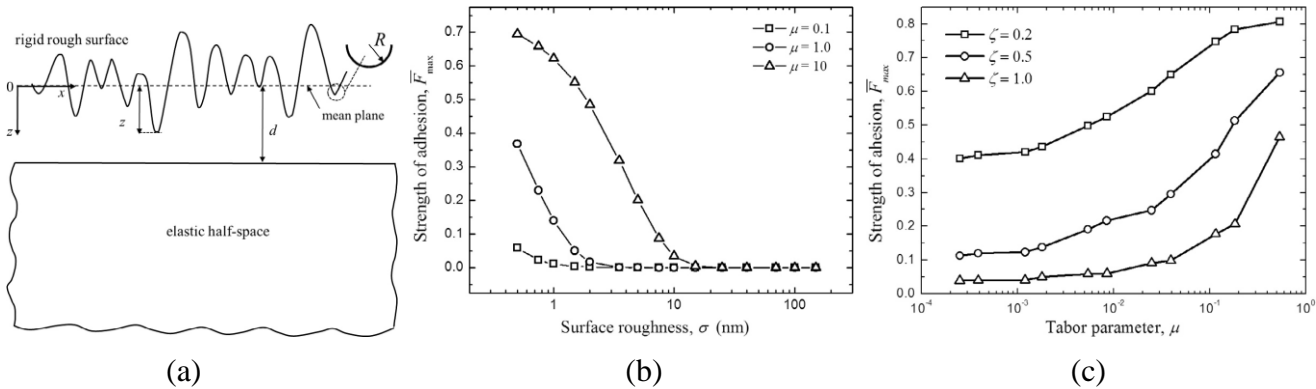
(a) Equivalent model of a rigid sphere in close proximity with an elastic half-space (the pile-up at the half-space surface is due to the effect of adhesion) and schematics of a rigid sphere in proximal distance with an elastic half-space for (b) relatively large gap (no surface deformation), (c) pile-up formation due to adhesive interaction, and (d) sudden surface contact (jump-in).



(a) Critical central gap at the instant of jump instability vs Tabor parameter and (b) pull-off force vs Tabor parameter.



(a, c) Normal load and (b, d) central gap vs displacement.



(a) Schematic of equivalent rough-surface contact model consisting of a rigid rough (fractal) surface and an elastic half-space, (b) strength of adhesion vs surface roughness, and (c) strength of adhesion vs Tabor parameter.

Selected Publications

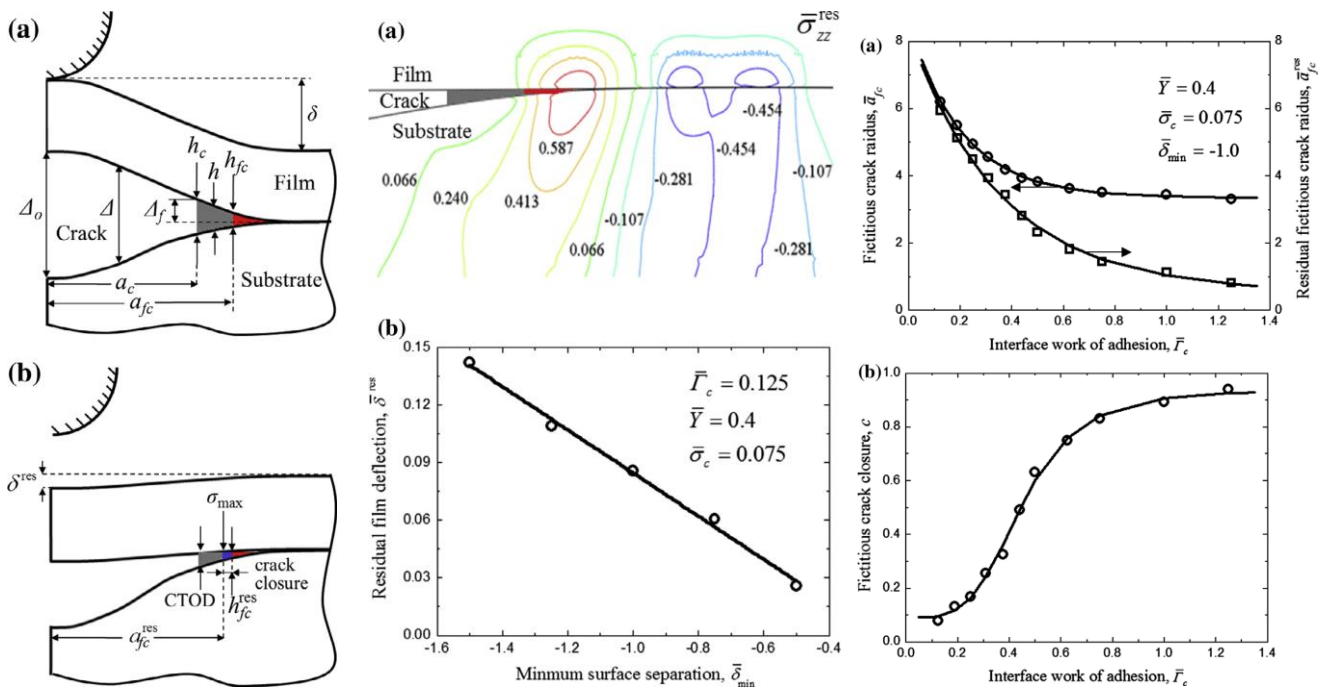
Song, Z., and Komvopoulos, K., "Adhesion-Induced Instabilities in Elastic and Elastic-Plastic Contacts during Single and Repetitive Normal Loading," *Journal of the Mechanics and Physics of Solids* **59**(4) 884 (2011).

Song, Z., and Komvopoulos, K., "Adhesive Contact of an Elastic Semi-infinite Solid with a Rigid Rough Surface: Strength of Adhesion and Contact Instabilities," *International Journal of Solids and Structures* **51**(6) 1197 (2014).

6. MECHANICS OF THIN FILM DELAMINATION IN ADHESIVE CONTACTS

Many engineering components are coated with protective films to protect the substrate from the high contact stresses and, in turn, premature failure. Therefore, the role of adhesion in contact behavior of layered solids was the objective of several recent studies. Specifically, we have investigated the adhesive

contact of a rigid spherical indenter with an elastic film supported by an elastic-plastic substrate using a bilinear cohesive zone law to model crack initiation and growth at the film/substrate interface. Our results elucidate the interdependence of contact instabilities and damage at the film/substrate interface of layered media subjected to adhesive contact loading and unloading. We observed ductile- and brittle-like modes of surface detachment upon unloading, characterized by the formation of a neck between the rigid spherical indenter and the layered medium and the formation of a residual impression on the unloaded layered medium, respectively. The obtained numerical results illustrate the effects of layer thickness, material properties, and maximum surface separation (interaction distance) on the maximum adhesion force, the commencement of jump-in and jump-out contact instabilities, and the evolution of substrate plasticity during loading and unloading, and indicate that incremental plasticity (ratcheting) in the substrate is the most likely steady-state deformation mechanism in cyclic contact loading.



Left: Schematics of a deformed layered medium (a) before and (b) after complete separation (jump-out) of the elastic film from the rigid sphere. Formation of a crack and a cohesive zone (gray region), partial closure of the cohesive zone (blue region), and high tensile stresses (red region) in front of the cohesive zone may occur at the film/substrate interface during a full load-unload cycle, depending on the material properties and minimum surface separation (maximum compressive force).

Middle: (a) Contours of residual stress and (b) variation of residual film deflection at the center of contact vs minimum surface separation.

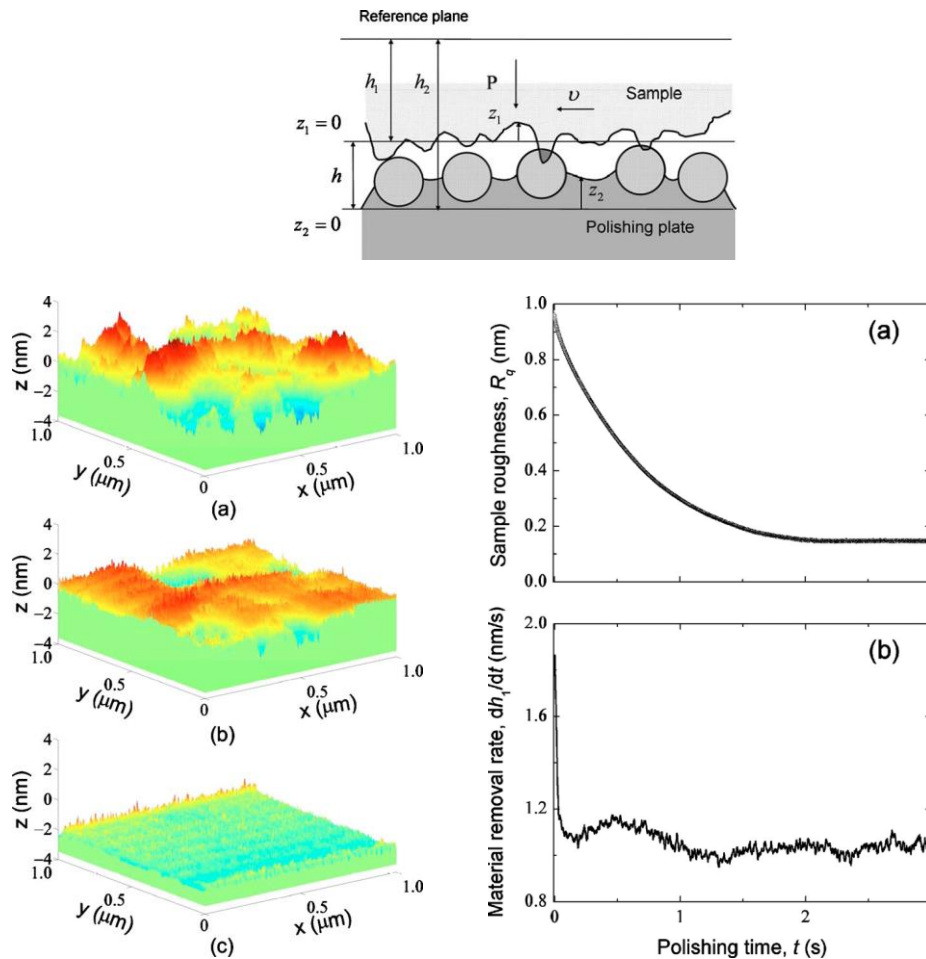
Right: (a) Radius of fictitious crack and residual fictitious crack and (b) closure of residual fictitious crack vs work of adhesion at film/substrate interface.

Selected Publications

Song, Z., and Komvopoulos, K., “Delamination of an Elastic Film from an Elastic-Plastic Substrate During Adhesive Contact Loading and Unloading,” *International Journal of Solids and Structures* **50**(16-17) 2549 (2013).

7. MECHANICS OF NANOSCALE POLISHING, ADHESIVE WEAR, AND ASPERITY MICROFRACTURE

Several physical processes may occur during surface contact. These processes originate between minute surface protrusions (asperities) and play the role of precursors of surface damage and wear. Among various wear processes resulting in the removal of material by repetitive surface interaction, the most often encountered process is adhesive wear. Surface damage due to adhesive wear is considered to be a principal factor leading to premature microdevice failure and limiting the efficiency of manufacturing processes of nanoscale material removal, such as chemo-mechanical polishing and lapping.

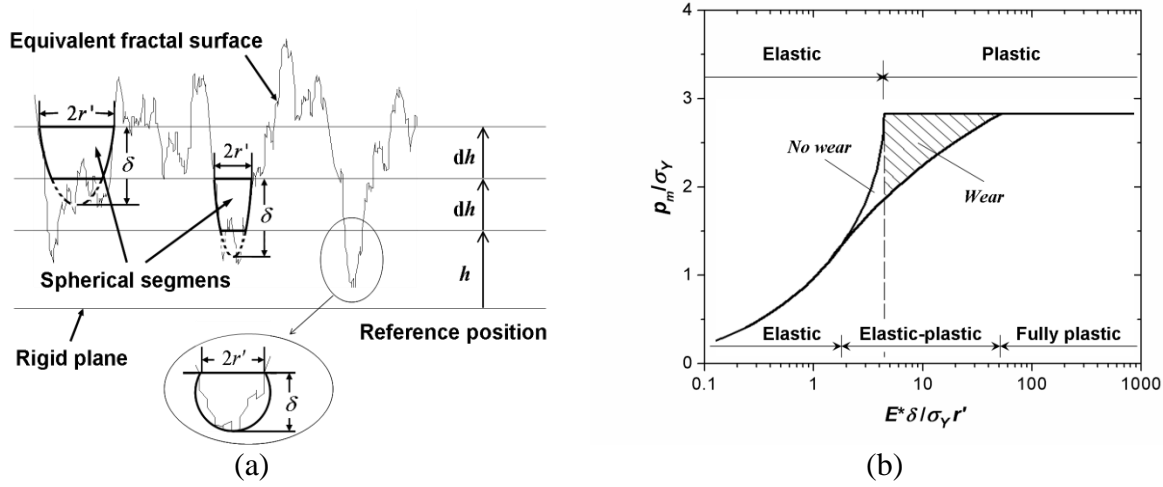


Top: Schematic illustration of the nanoscale polishing (lapping) process.

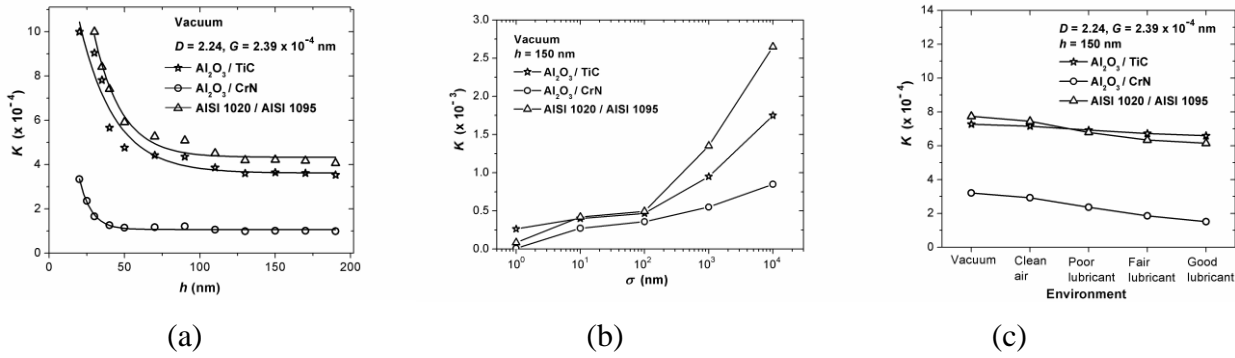
Bottom: Left: (a) initial, (b) transient, and (c) steady-state surface topographies of a polished surface.

Right: (a) surface roughness of a polished sample and (b) material removal rate vs polishing time.

Basic understanding of adhesion-induced material removal is of high importance to the endurance of mechanical systems and effectiveness of manufacturing processes of surface planarization and polishing. Wear particle formation due to asperity-asperity interaction is a consequence of cumulative surface damage including the sequential stages of plastic deformation, void/crack nucleation, and crack propagation.

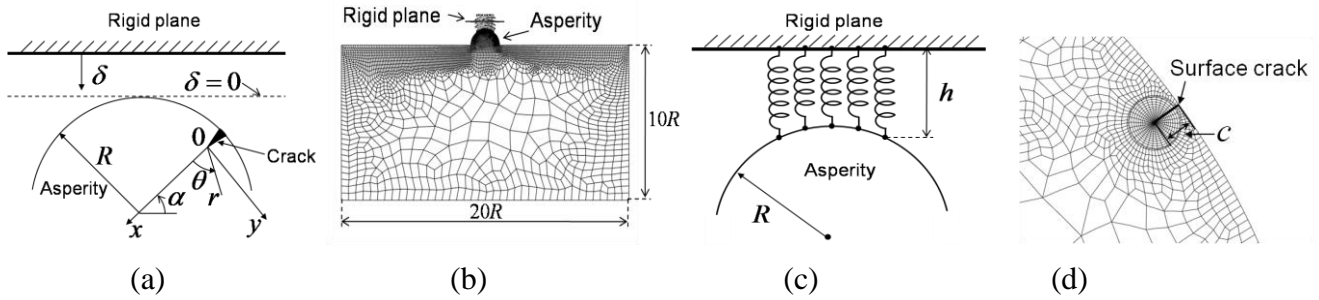


(a) 2D profile of a rough (fractal) surface truncated by a rigid plane and (b) normalized mean contact pressure p_m/σ_Y vs normalized representative strain $E^* \delta/\sigma_Y r'$.

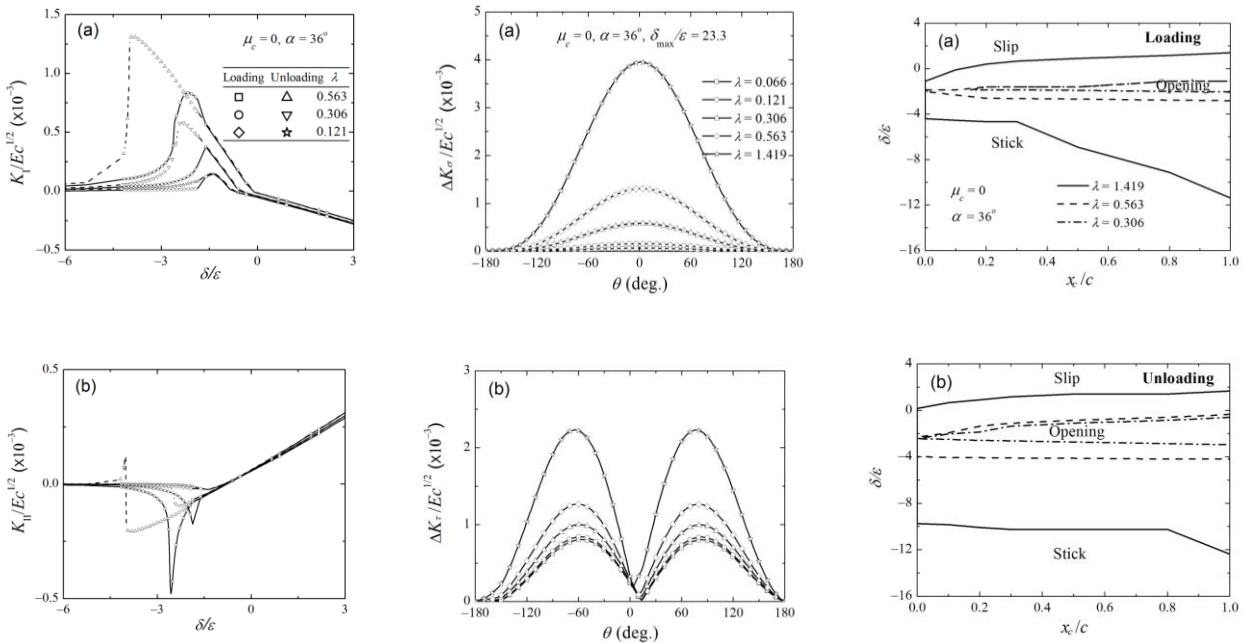


Wear coefficient K vs (a) global interference h , (b) rms roughness of equivalent surface σ , and (c) environment.

Adhesion-induced cracking in surface contact is a topic of particular interest that has not been thoroughly investigated. We have performed comprehensive fracture mechanics analyses of asperity cracking due to adhesive normal contact to determine the direction and rate of crack growth in cyclically loaded and unloaded asperities. FEM simulation results of this study were used to interpret the crack propagation direction and dominant crack mechanism in terms of asperity properties, work of adhesion, crack-face friction, maximum surface interference, and crack location at the asperity surface.



(a) Schematic of a rigid plane in the proximity of a cylindrical asperity with a small surface crack (the crack position is defined by the angle α and the surface interference δ is measured from the top of the undeformed asperity); (b) FEM mesh of a cracked asperity on a semi-infinite half-space in normal contact with a rigid plane; (c) schematic of nonlinear springs attached to the rigid plane and surface nodes of the elastic asperity, used to model surface adhesion; (d) refined mesh in the vicinity of the crack.



Left: Dimensionless stress intensity factors (a) $K_I/Ec^{1/2}$ and (b) $K_{II}/Ec^{1/2}$ vs surface interference δ/ϵ for loading (dashed lines) and (solid lines) unloading.
Middle: Dimensionless stress intensity factor ranges (a) $\Delta K_\sigma/Ec^{1/2}$ and (b) $\Delta K_\tau/Ec^{1/2}$ vs crack-growth direction θ .
Right: (a) Crack mechanism maps showing the evolution of opening, stick, and slip between the crack faces during (a) loading and (b) unloading.

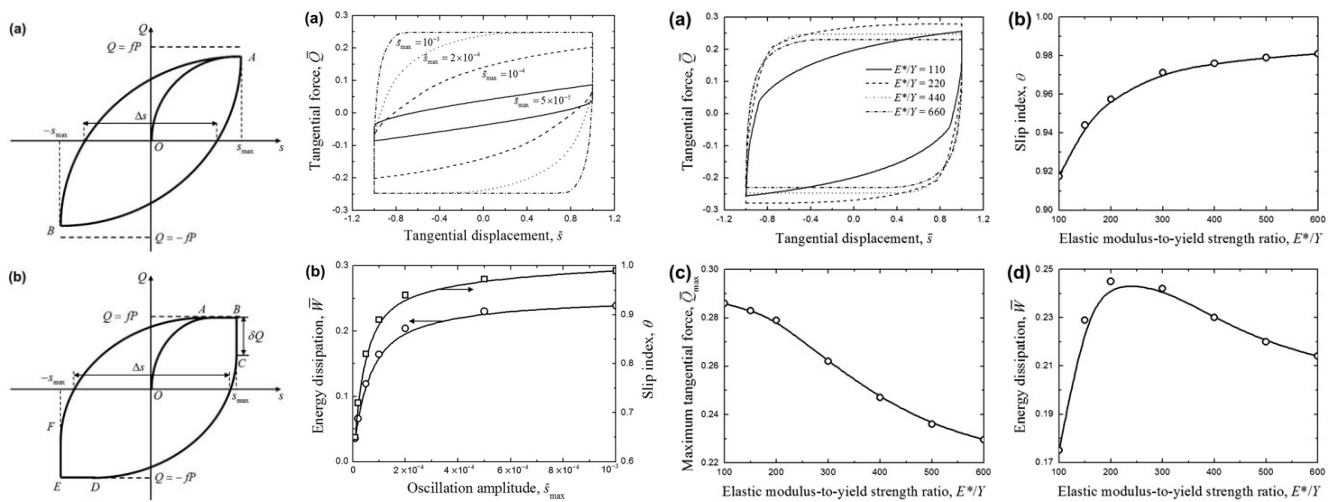
Selected Publications

Xu, H., and Komvopoulos, K., "A Quasi-Static Mechanics Analysis of Three-Dimensional Nanoscale Surface Polishing," *ASME Journal of Manufacturing Science and Engineering* **132**(3) 030912 (2010).
 Yin, X., and Komvopoulos, K., "An Adhesive Wear Model of Fractal Surfaces in Normal Contact," *International Journal of Solids and Structures* **47**(7-8) 912 (2010).

Xu, H., and Komvopoulos, K., "Fracture Mechanics Analysis of Asperity Cracking Due to Adhesive Normal Contact," *International Journal of Fracture* **181**(2) 273 (2013).

8. MECHANICS OF OSCILLATORY ELASTIC-PLASTIC CONTACTS

Structural vibrations during the operation of mechanical systems introduce oscillatory responses at joint interfaces, affecting the dynamic performance and operation of machines. The amplitude of the relative movement in oscillatory contacts may be on the order of a few tens of nanometers to several micrometers, depending on the applied load, elastic-plastic materials properties of interacting surfaces, and contact interface morphology. When the oscillation amplitude is much larger than the contact area, significant frictional energy is dissipated at the contact interface, resulting in the formation of wear debris by various mechanisms. However, when the oscillation amplitude is comparable with or less than the contact area, relative surface movement occurs in the outer region of the contact area (slip zone) but not in the center contact region (stick zone). Under stick-slip contact conditions, wear may occur by different sliding wear mechanisms (e.g., adhesion and abrasion) in the slip zone, and surface and/or subsurface (delamination) contact fatigue mechanisms in the stick zone. Thus, to elucidate the effects of surface roughness, contact pressure, oscillation amplitude, elastic modulus-to-yield strength ratio, and interfacial adhesion on the maximum tangential force and energy dissipated in elastic-plastic oscillatory contacts, we performed contact mechanics analyses of oscillatory rough surfaces characterized by fractal geometry. Our results have direct implications in a large range of oscillatory systems, from small microsystems, such as contact-mode MEMS devices, to large-scale dynamic systems, such as blades of high-power gas turbines.



Left: Schematic of tangential force Q vs. tangential displacement s for asperity contacts exhibiting (a) partial slip and (b) full slip.

Middle: (a) Tangential force vs. tangential displacement; (b) energy dissipation and slip index vs. maximum oscillation amplitude.

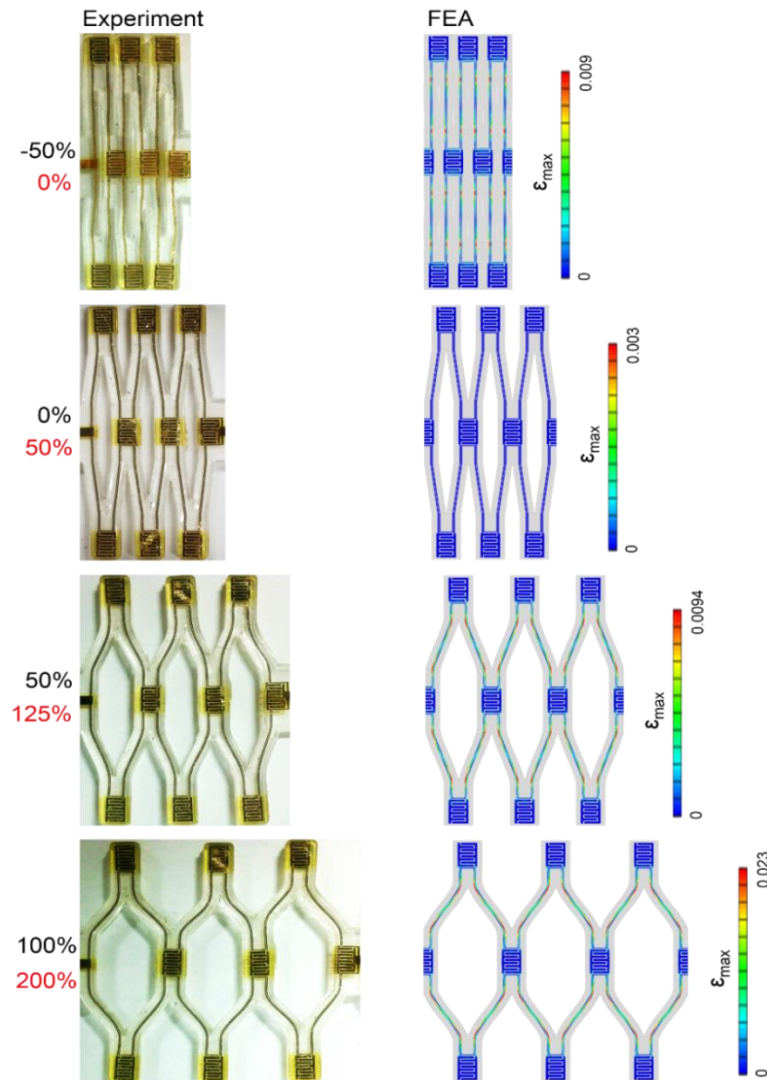
Right: Tangential force vs. (a) tangential displacement and (b) slip index; (c) maximum tangential force and (d) energy dissipation vs. elastic modulus-to-yield strength ratio.

Selected Publications

Song, Z., and Komvopoulos, K., "Contact Mechanics Analysis of Oscillatory Sliding of a Rigid Fractal Surface against an Elastic-Plastic Half-Space," *Philosophical Magazine* **94**(28) 3215 (2014).

9. MECHANICS OF FLEXIBLE AND STRETCHABLE ELECTRONICS

The rapid growth of wearable electronic devices has increased the demand for reliable flexible and stretchable electronics. To determine the stretchability of such electronics and, more importantly, to ensure that the locations where sensitive electronics, like microsupercapacitors (MSCs), are placed are essentially strain-free, 3D finite element analysis (FEA) was used to analyze the deformation of potential stretchable/flexible electronic structures subjected to various loadings, including uniaxial tension/compression, bending, and twisting.



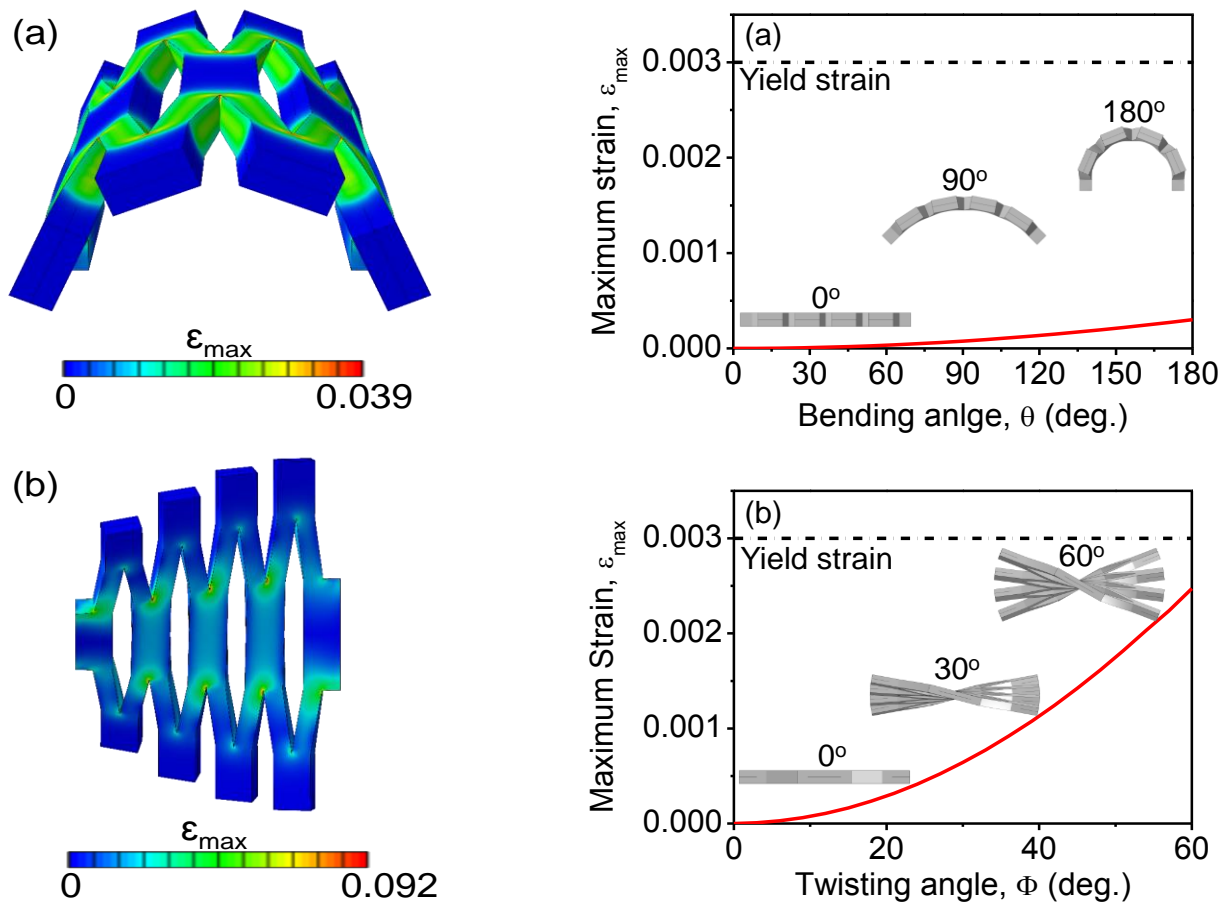
Left: Optical images of a 3×3 MSC array at different deformation stages.

Right: Corresponding FEA results of maximum (first principal) strain ϵ_{max} in the Au layer.

The FEA models capture the elastic-plastic deformation of the metallic components and the hyperelastic behavior of the honeycombed-like polydimethylsiloxane (PDMS) substrate. The above results provide insight into the capacity of such devices to accommodate large deformation and valuable guidance for mechanical testing.

We have obtained FEA results of MSC arrays showing that the devices can be stretched up to ~100% (zero prestrain) or 200% (-50% prestrain) without exceeding the yield strain in the gold layer of the devices. For example, for 100% stretching, the maximum strain in the bottom PDMS, top PI, Au, and bottom PI layers was found to be equal to 0.2, 0.024, 0.024, and 0.024, respectively. We also observed crack initiation at the sharp corners of the PDMS substrate when the device was stretched beyond 100%, and fracture when the elongation was increased to ~120%.

Our 3D FEA models show that for bending angles in the 0–180° range, the maximum strain in the gold layer of the MSCs is significantly below the yield strain. This is an intrinsic feature of the honeycomb structure of our microdevice. Also, because the gold layer is sandwiched by two identical polyimide (PI) layers and another two identical PDMS substrates, it is very close to the neutral plane of bending of the whole structure. Although twisting introduces larger strains in the device compared with bending, the gold layer exhibits purely elastic deformation in the 0°–60° twisting angle range.



Left: Distribution of maximum (first principal) strain ϵ_{max} in the PDMS layer of a 4×4 MSC array (a) bent by 180° and (b) twisted by 60°.

Right: Maximum (first principal) strain ϵ_{max} in the Au layer of a 4×4 MSC array as a function of (a) bending and (b) twisting angle. The inset figures in (a) show side-view schematics of the deformed device for a 0°, 90°, and 180° bending angle, whereas the inset figures in (b) show schematics of the deformed device for a 0°, 30°, and 60° twisting angle.

The findings of this work demonstrate the high potential of the present stretchable MSC arrays for a wide application range of wearable electronics, such as wrist and head band systems and wearable computing systems.

Selected Publications

Pu, J., Wang, X., Xu, R., and Komvopoulos, K., “Highly Stretchable Microsupercapacitor Arrays with Honeycomb Structures for Integrated Wearable Electronic Systems,” *ACS Nano* **10**(10) 9306 (2016).

Pu, J., Wang, X., Xu, R., and Komvopoulos, K., “Ultrahigh-Power, Flexible and Foldable Microsupercapacitors with Planar Interdigital Electrodes Consisting of Single-Walled Carbon Nanotube Networks,” submitted.